NOVEL APPLICATIONS OF PHOTONIC SIGNAL PROCESSING: TEMPORAL CLOAKING AND BIPHOTON PULSE SHAPING

A Dissertation

Submitted to the Faculty

of

Purdue University

by

Joseph M. Lukens

In Partial Fulfillment of the

Requirements for the Degree

of

Doctor of Philosophy

August 2015

Purdue University

West Lafayette, Indiana

For Angela, My Wife

Who can find a virtuous woman?
For her price is far above rubies.
Proverbs 31:10

ACKNOWLEDGMENTS

The last four years at Purdue have proven to be the most rewarding of my life—both professionally and personally—and accordingly I am indebted to many individuals whose guidance and friendship made this possible. First and foremost, I thank my advisor, Prof. Andrew M. Weiner, who first encouraged me to attend Purdue and initiated countless opportunities for high-impact research during my time here. Back in Fall 2011, I never would have guessed my Ph.D. dissertation would ultimately contain such colorful topics as time cloaking and quantum entanglement. The fact that it does speaks volumes to Prof. Weiner's remarkable ability to both identify and fund new avenues of exciting research—as well as see it through to completion with a mentoring approach that facilitates student growth and success. Coupled with his superior technical guidance was also valuable direction for my professional development; the chance to contribute to research proposals, write a book chapter, and attend the Siegman School on Lasers represent just a sampling of the unique opportunities I was given for growth.

The work accomplished in the laboratory would not have been possible without the expertise of our lab manager, Dr. Daniel E. Leaird. He was a constant source of help, feedback, and optics-guru wisdom; his accessibility and willingness to discuss most anytime removed countless roadblocks and sped up experiments. Postdoctoral scientist my first year at Purdue, Dr. Victor Torres-Company proved an erudite guide as I acquainted myself with the field of ultrafast photonics—both quantum and classical. His knowledge of deep theory and ability to teach important concepts made it like having another professor around—but without the added administrative responsibilities, so I could bug him more often!

I also thank Dr. Amir Dezfooliyan and Andrew J. Metcalf, fellow students with whom I was fortunate enough to work directly on experiments; their experience saved

me countless hours of work and combated the tedium of long days in the lab. I am grateful for Ogaga D. Odele, Poolad Imany, and Jose A. Jaramillo-Villegas, current members of the quantum optics subgroup in our lab, who provided lively discussions and excellent laboratory work. With them at the helm, nonclassical photonics should remain a forte of our lab for years to come. I thank Pei-Hsun Wang for valuable discussions throughout my thesis work, particularly in answering my numerous questions about on-chip frequency combs and their operation. It was helpful to have a fellow office mate like Pei-Hsun who worked similar predictable hours (uncommon for graduate students), giving me someone to quickly look to for questions ranging from "how did you solve that problem with the conducting sphere?" to "do you know when that form is due?" I am grateful to all the other members of Prof. Weiner's group since Fall 2011 as well, in particular Amir Rashidinejad, Yihan Li, Dr. Dennis Lee, Yang Liu, and Dr. Hyoung-Jun Kim for their help at various junctures. Dee Dee Dexter, our secretary, was always willing to go the extra mile when I asked her for help, far beyond her job responsibilities. Finally, I thank non-Purdue scientists Dr. Carsten Langrock (Stanford), Jiejun Zhang (Ottawa), and Prof. Daniel J. Gauthier (Duke), collaborators with whom I have enjoyed very valuable interactions and learning opportunities.

From a non-research side, I am especially appreciative of Unversity Lutheran Church. Its sound Biblical teaching has kept my family and me fed by Word and Sacrament throughout the past four years, and the friendships we have formed there will last a lifetime. I thank the pastors who served University Lutheran during my tenure: Rev. James Barton and Rev. Justin Herman. Both assumed their callings with humble dedication, and I am honored to have obtained their teaching and guidance. Most importantly, I am indebted to Angela, my wife and best friend. She supported me throughout all of graduate school, from the decision to pursue Ph.D. education rather than take a better-paying job, to long nights caring for a crying child; from my first published paper, to my final exam. I am blessed to have shared the last six years of my life with her, and I pray for even more rewarding years to-

gether in the future. I thank my two-year-old daughter, Nicaea, for giving me joy I never imagined possible. And I am grateful to her growing little sister for leaving mommy with enough energy to make it through another pregnancy; I can't wait to meet her soon!

Joseph M. Lukens

West Lafayette, Indiana
June 2015

TABLE OF CONTENTS

Page

LIST OF FIGURES

Figure Page

Figure Page

Figure Page

Figure Page

ABBREVIATIONS

BER	bit error ratio
CFBG	chirped fiber Bragg grating
CW	continuous-wave
DCF	dispersion-compensating fiber
DPSK	differential phase-shift keying
EPR	Einstein-Podolsky-Rosen
FWHM	full-width at half-maximum
HOM	Hong-Ou-Mandel
IM	intensity modulator
MZI	Mach-Zehnder interferometer
NRZ	non-return-to-zero
O-CDMA	optical code-division multiple-access
PM	phase modulator
PPLN	periodically poled lithium niobate
QKD	quantum key distribution
RF	radio-frequency
RMS	root-mean-square
RZ	return-to-zero
SFG	sum-frequency generation
SHG	second-harmonic generation
SLM	spatial light modulator
SMF	single-mode fiber
SPDC	spontaneous parametric downconversion
WDM	wavelength-division-multiplexed

ABSTRACT

Lukens, Joseph M. Ph.D., Purdue University, August 2015. Novel Applications of Photonic Signal Processing: Temporal Cloaking and Biphoton Pulse Shaping. Major Professor: Andrew M. Weiner.

We experimentally demonstrate two innovative applications of photonic technologies previously solidified in the field of classical optical communications. In the first application, we exploit electro-optic modulator technology to develop a novel "time cloak," a device which hides events in time by manipulating the flow of a probing light beam. Our temporal cloak is capable of masking high-speed optical data from a receiver, greatly improving the feasibility of time cloaking and bringing such exotic concepts to the verge of practical application. In the second specialization, high-resolution Fourier-transform pulse shaping—perfected for multi-wavelength telecom networks—is applied to shape the correlations of entangled photon pairs, states which have received considerable attention in nonlocal tests of quantum theory and in quantum key distribution. Using nonlinear waveguides fabricated out of periodically poled lithium niobate, we are able to demonstrate ultrafast coincidence detection with record-high efficiency, which coupled with our pulse shaper allows us to realize for the first time several capabilities in biphoton control, including high-order dispersion cancellation, orthogonal spectral coding, correlation train generation, and tunable delay control. Each of these experiments represents an important advance in quantum state manipulation, with the potential to impact developments in quantum information. And more generally, our work introducing telecommunication technology into both temporal cloaking and biphoton control highlights the potential of such tools in more nascent outgrowths of classical and quantum optics.

1. INTRODUCTION

The field of optical communication has revolutionized the manner in which information is transmitted across the globe, making the exchange of knowledge and ideas more efficient than ever. Facilitated by mature laser technology and the exceptionally low loss of silica fiber, modulation over the telecommunication band at 1550 nm is now the preeminent means for long-haul data transmission, unmatched in speed and range. And such high-speed communication has benefited greatly from the infusion of photonic technologies originally developed in ultrafast optics [1], the science and application of lasers capable of producing subpicosecond—or even few-femtosecond—bursts of light. For example, the basic arrangement for Fourier-transform pulse shaping [2,3], which was first demonstrated on broadband laser pulses in the visible portion of the spectrum [4], has been exploited in the development of wavelength-selective switches and gain equalizers for infrared optical communication [5]. Likewise, optical frequency combs—coherent light sources consisting of a discrete set of frequency components—have forged their way into optical communications. Whereas self-referenced mode-locked lasers have received considerable attention as comb sources, particularly for ultraprecise frequency metrology [6, 7], in other applications such as optical communication and arbitrary waveform generation [8], better-suited combs can be obtained through straightforward electro-optic modulation of a single-frequency laser beam, for in these functions simplicity and high repetition rates prove more valuable than absolute frequency stability. Such sources require only off-the-shelf telecommunication components and have found use in areas ranging from line-by-line pulse shaping [9] to radio-frequency (RF) photonic filters [10].

Notwithstanding the fervent research which continues to be directed toward advancing and improving both electro-optic combs and telecom-compatible pulse shaping, these technologies have reached a level of maturity at which they are ripe for

appropriation by other specializations of optical physics; no longer need they be classified solely as *investigational topics*, for they now can be viewed also as *tools* to drive advances in new fields. In this dissertation, we will describe experimental work in two distinct areas aimed to do precisely that: extend photonic technologies to regimes of physics where they have either been underutilized or absent altogether. In the first case, we will discuss the application and inversion of electro-optic frequency-comb generation to form a "time cloak" that is capable of hiding high-speed optical data from a receiver. And in the second portion, telecom pulse-shaping techniques will be used to shape the correlations of entangled photon pairs ("biphotons" for short), nonclassical light which is of great interest in both fundamental tests of quantum mechanics and quantum key distribution (QKD).

This dissertation is organized as follows. In Chapter 2 we describe in detail our high-speed temporal cloak, from theory to experimental implementation, followed by further improvements relevant to optical communications in Chapter 3. Chapter 4 then tackles the quantum optical formalism necessary describe our experiments in biphoton pulse shaping. Chapters 5 and 6 cover biphoton experiments with electronic coincidence detection and ultrafast biphoton sum-frequency generation (SFG), respectively. Finally, in Chapter 7 we introduce key areas we envision for future work in both time cloaking and biphoton pulse shaping.

2. TEMPORAL CLOAKING

2.1 Background

The origin of temporal cloaking can actually be traced to recent progress in *spatial* cloaks. Once relegated to the realm of science fiction, such invisibility cloaks have now risen to the forefront of scientific research, thanks to the development of so-called "metamaterials"—artificially engineered media with exotic properties unattainable in nature, including negative refractive index. Veselago predicted as early as 1968 that a medium with simultaneously negative permeability and permittivity would display strange behavior, such as negative refraction and backward phase velocity [12], but it was not until 1999 that it finally became possible to realize such a medium, when Pendry *et al.* proposed resonant structures capable of yielding an effective negative permeability at microwave frequencies [13]; the first demonstration of a negative-index medium followed in 2000 [14]. Yet the potential of metamaterials was soon shown to extend well beyond just negative refraction to even spatial invisibility cloaks [15–17], spawning an explosion of research which continues to progress at an ever-growing pace [18–24]. It was out of this backdrop that the first proposal for a space-time cloak emerged [25], based on the simple idea that, just as a spatially varying refractive index can bend light around a point in space, a time-varying index could be used to open up and close an intensity gap in time, thereby preventing the beam from interacting with—and therefore detecting—some temporal event. By combining the two, then, it is possible to at least envision a theoretical space-time cloak that hides *events* rather than just *objects* [26, 27].

Although a full space-time cloak has yet to be realized, Fridman *et al.* have demonstrated a temporal cloak which prevents a nonlinear interaction at a single

The key results of this chapter have been published in [11].

point in optical fiber [28]. The principle of the cloak's operation is based on the concept of space-time duality, the mathematical equivalence between paraxial diffraction and narrowband dispersion [29,30]. Since space-time duality provides the major theoretical underpinnings for the cloak we have constructed as well, it is profitable at this point to consider its origin and implications in detail. We therefore introduce the notation that will be employed throughout the rest of this dissertation. In all of the described experiments, polarization and transverse spatial degrees of freedom can be neglected, and so we consider an electric field that is a function only of the longitudinal distance z and time t, expressed as

$$E(z,t) = E^{(+)}(z,t) + E^{(-)}(z,t), \tag{2.1}$$

with $E^{(\pm)}(z,t)$ representing the positive and negative frequency components of the real field. That is,

$$E^{(+)}(z,t) = \int_0^\infty d\omega\, \tilde{E}(z,\omega) e^{-i\omega t}, \tag{2.2}$$

and

$$E^{(-)}(z,t) = \left[E^{(+)}(z,t)\right]^*, \tag{2.3}$$

where $\tilde{E}(z,\omega)$ is the Fourier transform of the real field $E(z,t)$. (The usefulness of the $\pm$ formalism will become evident in the extension later to quantum optics.) After Haus [31], we express $\tilde{E}(z,\omega)$ in terms of a baseband envelope $A(z,\Omega)$, slowly varying in both space and time:

$$\tilde{E}(z,\omega) = \begin{cases} A(z,\omega-\omega_0)e^{i\beta_0 z} & ; \quad \omega > 0 \\ A^*(z,-\omega+\omega_0)e^{-i\beta_0 z} & ; \quad \omega < 0, \end{cases} \tag{2.4}$$

where $\beta_0 = \beta(\omega_0)$ is the propagation constant evaluated at $\omega = \omega_0$, and we assume that $A(z,-\omega_0) = 0$ (i.e., that the optical bandwidth does not extend to zero frequency). As derived in [1], the spectrum $\tilde{E}(z,\omega)$ must satisfy the equation

$$\left[\frac{\partial^2}{\partial z^2} + \beta^2(\omega)\right] \tilde{E}(z,\omega) = 0 \tag{2.5}$$

in a linear medium, which is valid for both free-space and waveguide transmission. In the latter case, the propagation constant $\beta(\omega)$ is determined by the transverse field

distribution; since the primary guiding structure we use is standard optical fiber, we can take $\beta(\omega)$ as given and discount any transverse dependence. Considering the case $\omega = \omega_0 + \Omega$, we therefore obtain the following equation for $A(z, \Omega)$:

$$\frac{\partial^2 A}{\partial z^2} + 2i\beta_0 \frac{\partial A}{\partial z} + \left[\beta^2(\omega_0 + \Omega) - \beta_0^2\right] A = 0. \tag{2.6}$$

We now invoke the slowly varying envelope approximations in space, to neglect the term $\partial^2 A/\partial z^2$, and in time, to write $\beta_0 + \beta(\omega) \approx 2\beta_0$, leaving

$$2i\beta_0 \frac{\partial A}{\partial z} + 2\beta_0 \left[\beta(\omega_0 + \Omega) - \beta_0\right] A = 0. \tag{2.7}$$

Finally, continuing to exploit the narrowband assumption, we express β as the Taylor expansion $\beta(\omega_0 + \Omega) = \beta_0 + \beta_1\Omega + \beta_2\Omega^2/2$. Keeping up to second order in Ω thus simplifies finally to

$$\frac{\partial A}{\partial z} - i\beta_1\Omega = \frac{i\beta_2\Omega^2}{2} A, \tag{2.8}$$

which when inverse Fourier transformed becomes

$$\frac{\partial a}{\partial z} + \beta_1 \frac{\partial a}{\partial t} = -\frac{i\beta_2}{2} \frac{\partial^2 a}{\partial t^2}, \tag{2.9}$$

where $a(z, t) = \int d\Omega\, A(z, \Omega) e^{-i\omega t}$. The β_1 term simply produces an overall time delay at each position z, so we can remove it by defining a retarded time variable via the transformation $t - \beta_1 z \to t$, $z \to z$:

$$\frac{\partial a}{\partial z} = -\frac{i\beta_2}{2} \frac{\partial^2 a}{\partial t^2}. \tag{2.10}$$

This equation describes the linear field evolution for both our temporal cloak and that of [28]. And a remarkable result is found if we compare this propagation equation to paraxial spatial propagation of a monochromatic field. For example, if we now take the electric field to be

$$E^{(+)}(x, z, t) = u(x, z) e^{i(kz - \omega_0 t)}, \tag{2.11}$$

where $k = n(\omega_0)\omega_0/c$, and we impose the paraxial approximation, a similar calculation yields [31]

$$\frac{\partial u}{\partial z} = \frac{i}{2k} \frac{\partial^2 u}{\partial x^2}. \tag{2.12}$$

With the identifications $a \leftrightarrow u$, $t \leftrightarrow x$, and $\beta_2 \leftrightarrow -1/k$, the equations of motion for both narrowband dispersion [Eq. (2.10)] and paraxial diffraction [Eq. (2.12)] are identical, implying a one-to-one relationship between physically distinct phenomena associated with either approximation [30]. For example, the well-known result that parabolic phase applied by a thin lens can be used to focus a light beam in space is readily extended to temporal optics, for quadratic temporal phase followed by a properly chosen dispersive medium can compress optical waveforms in time [29]. Exploiting this analogy, Fridman *et al.* [28] constructed a "split-time" lens which applied quadratic temporal phase with a sharp slope discontinuity to a continuous-wave (CW) input probe, analogous to sending a planar wave between two spatial lenses connected at the tips. Then by propagating the modulated field through optical fiber with dispersion chosen to satisfy the temporal imaging condition, they generated a temporal intensity gap, during which an ultrafast pump beam could not interact with the probe. Thereafter the beam traversed fiber with the opposite sign of dispersion, closing up the intensity hole, and was modulated by a second, negative split-time lens to remove the residual temporal phase, leaving an output ideally identical to the original CW input. In this way, the pump beam (the event) was cloaked from the observer, for the probe designed to interact with it was unmodified at the output, thereby giving the deceptive impression it was absent completely.

These seminal results demonstrated that time cloaking could indeed be implemented in practice; however, this cloak operated at the pedestrian repetition rate of 41 kHz and generated a cloaking window equal to only about 10^{-4}% of the temporal period [28]. Both the low frequency and fractionally small cloaking window disqualify such a cloak from many applications in high-speed optical communications, in which data are transmitted at gigahertz rates and encompass a large fraction of the total period. For this reason, we have worked to develop a new temporal cloak thoroughly compatible with optical communications and capable of hiding high-speed data from a receiver, bringing the temporal cloak to the verge of practical application through the use of optical frequency-comb technology.

2.2 Building the Telecom Temporal Cloak

The time lenses in the first temporal cloak relied on nonlinear mixing of the CW probe with a strong pulsed laser to generate the desired phase [28]. Yet although time lenses based on such parametric interactions can produce large temporal chirps [32, 33], the requirements of high-power pulsed lasers and complicated optics make them ill-suited for high-speed telecom applications. Instead, electro-optic phase modulators prove more convenient; already common in optical communications—and therefore commercially available—phase modulators offer high RF bandwidth and linear optical operation, requiring only a single electrical input which can be readily synchronized to a global system clock [34]. Nevertheless, the sinusoidal voltages which are typically, and most conveniently, employed to drive these components yield temporal phase modulation that is only approximately quadratic over a portion of the period, meaning that input waveforms which extend beyond this window suffer from severe temporal aberrations [35], analogous to the wavefront distortions induced by imperfect spatial lenses in Fourier optics. Moreover, the nature of the split-time lens requires that the parabolic approximation remain valid all the way to the edge of the temporal period, for it is precisely this sharp chirp discontinuity which permits the formation of a temporal hole. Figure 2.1(a) highlights this situation, comparing the phase profile of an ideal array of split-time lenses to that of a sinusoid with the same quadratic phase coefficient. The sinusoid is wholly unable to reproduce the slope discontinuity, and even if we were to employ an arbitrary waveform generator to drive the modulator with a signal more accurately reproducing a parabola, limited RF bandwidth still precludes realization of the discontinuity; as shown in Fig. 2.1(b), keeping even up to five harmonics of the ideal signal fails to replicate the discontinuity, yielding instead a smoothed, zero-slope region in its wake. For the goal of high-speed communication at the limits of available RF bandwidth, such a requirement is impossible to satisfy, and therefore a substitute for the split-time lens is necessary in order to attain a high-speed temporal cloak.

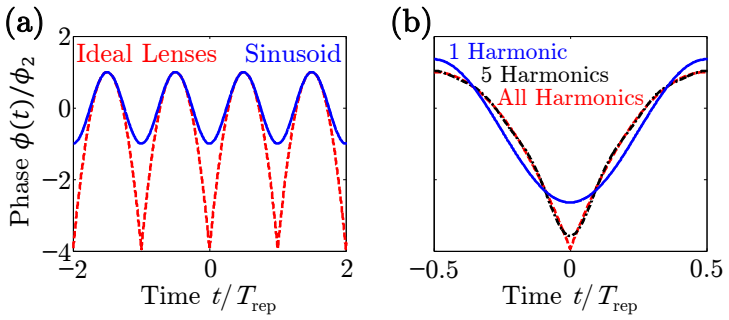

Fig. 2.1. RF bandwidth restrictions on the applied phase. (a) Comparison of the phase of an ideal time-lens array to a pure sinusoid with the same second-order Taylor coefficient $\phi_2 = d^2\phi/dt^2$ expanded about the peaks. The sinusoid is only able to mimic the ideal phase around the maxima; the quadratic approximation breaks down completely at the slope discontinuities. (b) Calculated filtering of the ideal phase. Subjecting the ideal parabolic phase profile to spectral filtering rounds off the discontinuity to a point of zero chirp. This is evident even in a filter passing five harmonics, an RF bandwidth difficult to obtain at fundamental frequencies of 10 GHz and beyond.

It is at this point that we exploit previous work in the generation of frequency combs through electro-optic modulation of CW light. In this application, a common objective is the conversion of CW light into a train of smooth, high-extinction pulses. This is precisely the goal of a temporal cloak, for in this case we wish to create regions of zero intensity within an initially uniform-intensity waveform. One successful method is based on the temporal version of the Talbot effect. Observed as early as 1836 [36], the spatial Talbot self-imaging phenomenon describes near-field diffraction of a plane wave off of a periodic grating, in which the image of the grating is repeated at discrete distances [37, 38]. A temporal analogue [39] follows from space-time duality. Consider an input optical spectrum $A_{\rm in}(\Omega)$ with a temporal period $2\pi/\omega_m$, described as a series of delta functions:

$$A_{\rm in}(\Omega) = \sum_p c_p \delta(\Omega - p\omega_m). \tag{2.13}$$

Propagating this field through a second-order dispersive medium of length L and dispersion constant β_2 gives the output $A_{\text{out}}(\Omega) = A_{\text{in}}(\Omega)e^{i\beta_2 L\Omega^2/2}$, which in this case becomes

$$A_{\text{out}}(\Omega) = \sum_p c_p \delta(\Omega - p\omega_m) e^{i\beta_2 L p^2 \omega_m^2/2}. \tag{2.14}$$

Therefore we see that, because of the field's periodicity, whenever the quantity $\beta_2 L\omega_m^2/2$ is equal to an integer multiple of 2π, $A_{\text{out}}(\Omega) = A_{\text{in}}(\Omega)$ and perfect reconstruction is obtained. Thus we define the fundamental Talbot length L_T as

$$L_T = \frac{4\pi}{|\beta_2|\omega_m^2}; \tag{2.15}$$

propagation through any integer multiple of this distance yields perfect replication of the input.

Although mathematically more complicated, fractional Talbot distances can also produce interesting waveforms, and in fact it is this fractional Talbot effect that is exploited in pulse generation. Specifically, we consider an input CW envelope that is sinusoidally phase modulated at an index of $\pi/4$:

$$a_{\text{in}}(t) = e^{-i\frac{\pi}{4}\cos\omega_m t}, \tag{2.16}$$

where the particular time origin is chosen for compactness of the final result. The field $a_{\text{out}}(t)$ after propagation through $L_T/4$ can be obtained analytically, although the derivation is too lengthy to reproduce here; see Appendix A for details. Assuming for definiteness that $\beta_2 > 0$ (this only impacts the overall phase), we arrive at the simple result

$$a_{\text{out}}(t) = \sqrt{2}\cos\left(\frac{\pi}{2}\sin^2\frac{\omega_m t}{2}\right), \tag{2.17}$$

which represents roughly 50%-duty-cycle flattop pulses separated by regions of zero intensity. Therefore, through temporal interference based on the Talbot effect, it is possible to convert a CW waveform into pulses with wide cloaking windows simply through sinusoidal phase modulation followed by dispersion—no split-time lens or exotic modulation is required. These cloaking windows represent a significant duration of the temporal period, orders of magnitude longer than in the first temporal cloak,

which we experimentally confirm in the next section. To widen the cloaking window even further, we can subsequently apply strong sinusoidal phase modulation to this pulse train; since the optical energy now lies primarily within the quadratic cusps of the sinusoid, minimal aberrations are incurred in the temporal imaging process, and so we can compress the pulses further through standard time-lensing procedures. This basic setup—phase modulation, quarter-Talbot dispersion, more phase modulation, and dispersion for pulse compression—has been explored for pulse generation [40–42], and we now extend it to high-speed temporal cloaking. Moreover, since phase modulation and dispersion introduce only linear insertion loss, they can be inverted through complementary dispersion and modulation. This crucial quality provides a means for subsequently closing up the temporal gap to produce a full cloak, in which the output shows no sign of additional data modulation and is ideally identical to the input.

The spatial analogue of our complete temporal cloak is presented in Fig. 2.2(a). The CW input followed by sinusoidal phase modulation is equivalent to a plane wave impinging on a sinusoidal phase grating, which through the Talbot effect is converted into a pattern of maxima and minima with unity visibility. The negative lens array represents the next round of sinusoidal phase modulation, which when followed by another dispersive medium focuses the optical energy to narrow spikes, between which any interactions (events) have no impact on the optical field. The remainder of the cloak then consists of the complementary elements (dispersion and phase modulation) required to fill in the temporal gaps and produce an output identical to the input, with no trace of the events' presence. We point out that through space-time duality, the spatial analogue to the temporal cloak requires exotic negative-index media to undo diffraction through positive-index media; on the other hand, optical fiber with both positive and negative dispersion is readily available, making the temporal version we implement realizable with standard commercial components. Figure 2.2(b) provides the numerically simulated intensity distribution corresponding to the cartoon in Fig. 2.2(a). Sharp concentration of the probe waveform is obtained, with cloaked regions of the same order in duration as the temporal period itself, made possible by interference

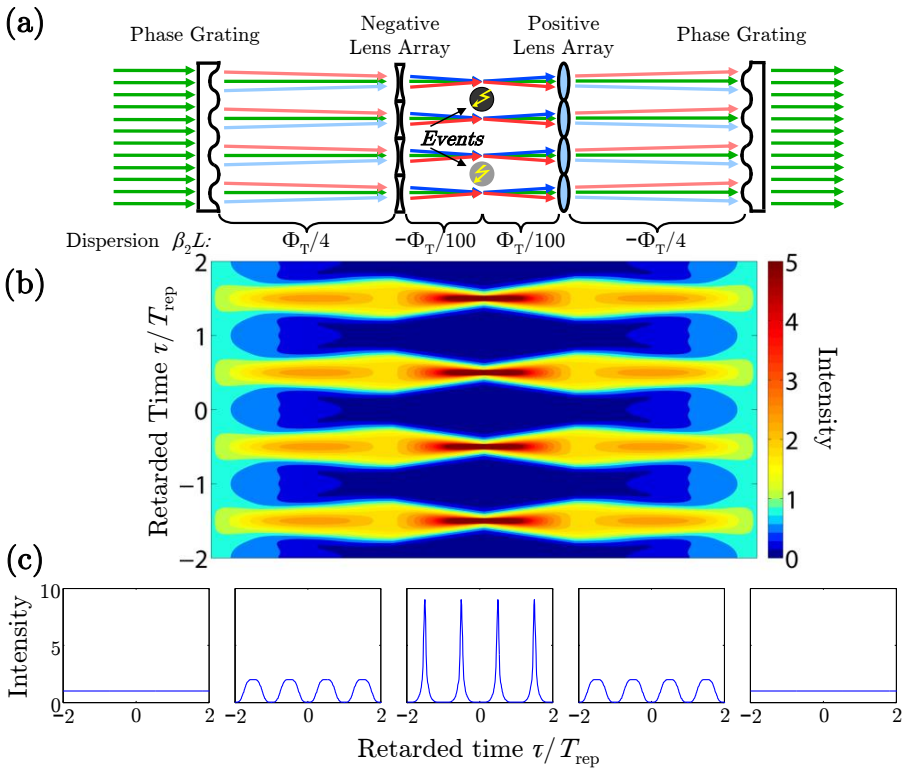

Fig. 2.2. Spatial analogue of temporal cloaking circuit. (a) Temporal ray diagram highlighting the spatial equivalent of the experimental setup. Φ_T represents the Talbot dispersion for DCF with dispersion constant β_2. Owing to the diffractive nature of the Talbot effect, temporal ray optics is not strictly applicable, but we nonetheless include this ray diagram for visualization. (b) Corresponding simulated intensity distribution. Wide cloaking windows of zero intensity appear at the temporal focus, nearing the duration of the repetition period, T_{rep}. (c) Temporal intensity slices at specific locations in the circuit (from left to right): first grating, negative lens array, event plane, positive lens array, and final grating.

through the Talbot effect. Finally, Fig. 2.2(c) shows intensity slices at various points throughout the cloaking circuit; high-extinction flattop pulses are evident after the quarter-Talbot dispersion, with intense and narrower pulses at the event plane. This basic arrangement is what we employ in our cloaking experiments, with different excitations examined as the event to cloak.

2.3 Experimental Realization

The full experimental setup is presented in Fig. 2.3. Operating at a global clock rate of 12.7 GHz, our input is a CW fiber laser (Koheras AdjustiK) at ∼1542 nm. The first phase modulator and chirped fiber Bragg grating (CFBG) generate flattop pulses, which are then modified by another phase modulator operated an index of about 2π, limited by the maximum allowable input RF power. The experimentally generated frequency comb is shown in Fig. 2.4(a), possessing 16 lines in the 10-dB bandwidth. Temporal compression of this frequency comb is then achieved with ∼1 km of Corning SMF-28e single-mode fiber (SMF); Fig. 2.4(b) displays the measured temporal autocorrelation of the probe field directly after this fiber link. The full-width at half-maximum (FWHM) of 11.7 ps represents only about 15% of the RF period, indicating the possibility for fractionally wide cloak durations. These pulses are next sent through an intensity modulator, whose function is to apply the event to be cloaked; we consider both sinusoidal intensity modulation and pseudorandom data. The succeeding −17-ps/nm dispersion-compensating fiber (DCF), phase modulators, and CFBG return the field to its original form, with erbium-doped fiber amplifiers employed to compensate for overall insertion loss. An additional DCF link is appended to the end of the setup, in order to permit undistorted data transmission when the cloak is turned off. In other words, with no voltage applied to the phase modulators, we want the event modulation to appear unscathed at the output, as if the cloak were absent completely—essentially "turning off" the temporal cloak. This requires that approximately zero net dispersion be present after the event plane, thereby necessitating the additional link. And since when the cloak is on, ideally a single-frequency field is input into the final DCF module, negligible distortion is induced when the phase modulators are operating. Finally, although omitted from Fig. 2.3, RF phase shifters are also utilized on four of the five modulators to ensure temporal synchronization.

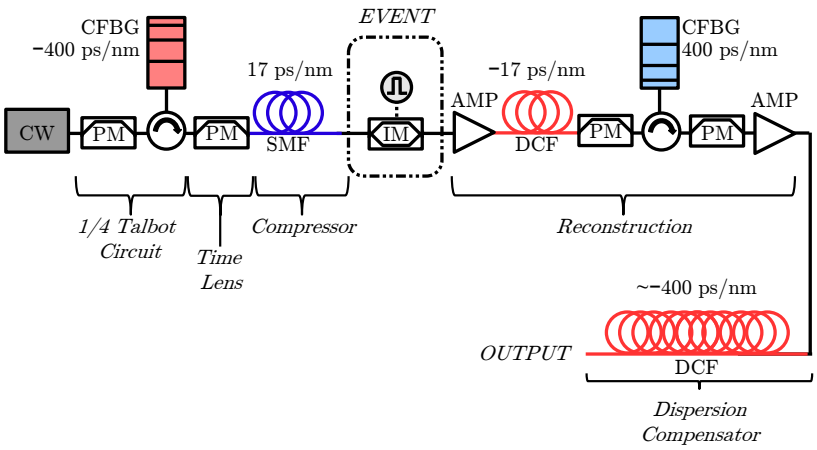

Fig. 2.3. Experimental setup of cloaking circuit. CW, continuous-wave input laser; PM, phase modulator; CFBG, chirped fiber Bragg grating; SMF, single-mode fibre; DCF, dispersion-compensating fiber; IM, intensity modulator; AMP, erbium-doped fiber amplifier.

We characterize cloak performance by splitting the output, sending one portion to an optical spectrum analyzer and the other to a 12.3-Gb/s photoreceiver (Agere 2560A-C02). We employ a photodetector with limited bandwidth for the purposes of cloak enhancement. Ostensibly one might regard such filtering as breaking the rules, for indeed a sufficiently narrowband filter can convert any field into a monochromatic waveform—this is not a cloak. However, in our case, the filtering is intentionally designed to leave the event intact, only impacting sidebands introduced by the cloak itself. As evident in Fig. 2.4(a), the cloak adds many spectral components to the input field, and so any mismatch between complementary phase modulators can leave residual energy extending out to several harmonics. On the other hand, the event to be cloaked (such as sinusoidal or pseudorandom modulation) could be relatively narrowband, producing minimal spectral spreading and lying primarily within the first-order sidebands. Figure 2.5 provides a schematic of this concept; since the unwanted harmonics—due to cloak imperfections—reside outside of the event passband itself, it is therefore possible to preferentially filter them out while leaving the event

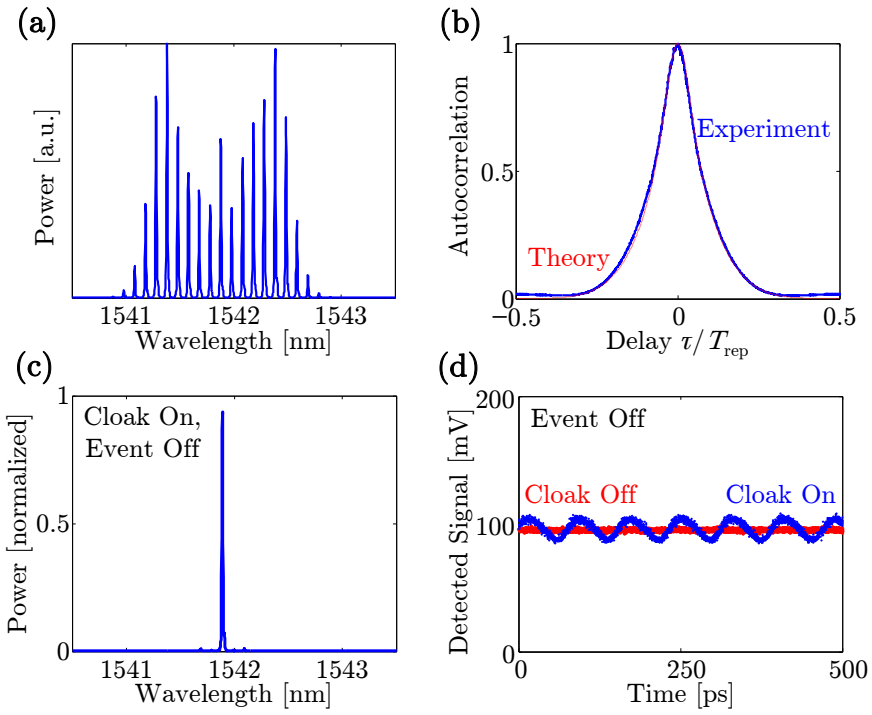

Fig. 2.4. Characterization of cloaking circuit. (a) Comb spectrum at the event plane, consisting of 16 spectral lines in the 10-dB bandwidth. (b) Corresponding intensity autocorrelation, shown over one full temporal period. The FWHM is 11.7 ps. (c) Spectrum at the output of the cloaking circuit, when no event is applied. (d) Corresponding temporal output measured on a photodetector, compared to the case when all phase modulators are off.

untouched. Thus, when the cloak is turned off, the filter allows the event to be registered undistorted at the output, whereas when the cloak is on, the filter merely cleans up cloak performance. Returning to experiment, with no event applied the measured output spectrum and received electrical signal are presented in Figs. 2.4(c) and (d). The sidebands present after the second phase modulator are suppressed by about 20 dB, leaving a single-frequency output, and the temporal output is nearly flat, albeit with small residual modulation resulting from imperfections in the cloak. These results demonstrate the ability to generate a broadband, smoothly compressed pulse train and then reverse the process to reobtain the monochromatic input field.

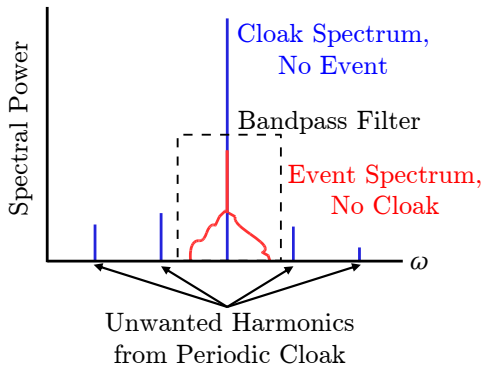

Fig. 2.5. Principle of spectral filtering for cloak enhancement. Even with no event present, cloak imperfections leave parasitic sidebands that are not fully compensated. But if the event has a spectrum lying primarily within these harmonics—as would be the case with pseudorandom data, for example—a bandpass filter can be used to preferentially remove the remaining sidebands without distorting the event itself.

The capacity to cloak an optical event is first examined with the clock signal applied directly to the intensity modulator, which yields high-contrast sinusoidal modulation when no cloak is present. With the phase modulators turned off, the output spectrum shows two strong sidebands [Fig. 2.6(a)], which are completely removed when the cloak is turned on [Fig. 2.6(b)]. Likewise, the temporal output consists of high-contrast sinusoidal modulation when the cloak is off, reducing to a nearly flat line when the cloak is operating, as shown in Fig. 2.6(c). The cloak is able to completely mask the presence of the intensity modulation, an event which comprises a significant fraction of the temporal period. For a more quantitative measure of this defining metric, the cloaking window, we temporally detune this sinusoidal event from the optimum point at which the peaks align with the compressed probe pulses, introducing modulation at the output. By measuring this modulation as a function of the time shift, we are able to arrive at an experimental assessment of the cloaking window's duration. The results for this test are presented in Fig. 2.6(d). The root-mean-square (RMS) output fluctuation, normalized to the mean, is plotted as

a function of the temporal detuning, alongside theoretical predictions and the value when the cloak is absent. Defining the cloaking window as the time shift at which this modulation equals one-half that in the uncloaked case, we find (accounting for negative detuning as well) a value of 36 ps, or 46% of the temporal period, which represents a conservative estimate since the sinusoidal perturbation has a large duration in itself. It is interesting that previous work in metamaterial cloaking arrays [43] using tapered gold-coated waveguides [44] achieved spatial cloaking over roughly 20% of the two-dimensional surface, comparable to the value we have obtained with our temporal cloak. And whereas the previous temporal cloak [28] operated on essentially isolated events, ours is truly periodic; indeed, the Talbot effect we exploit relies on precisely such periodicity to generate time holes which encompass such a large fraction of the temporal period. This wide cloaking window coupled with the multi-gigahertz repetition rate finally opens the door for temporal cloaking of high-speed optical data.

Therefore we next examine data applied to the intensity modulator, choosing an inverted (or dark) return-to-zero (RZ) modulation format. This ensures that the transmission function returns to unity during some fixed fraction of each bit period, providing temporal regions through which the compressed probe pulses can pass, with the binary data applied during the cloaked regions. We utilize a bit-error-ratio (BER) tester (Agilent N4901B) to create a non-return-to-zero (NRZ) binary sequence, which is then converted to inverted return-to-zero format by a high-speed logic circuit (Hittite HMC706LC3C) and used to drive the intensity modulator. The temporal outputs measured on a sampling oscilloscope for length $2^{31} - 1$ pseudorandom data [Fig. 2.7(a)] and for a specific sequence of ones and zeros [Fig. 2.7(b)] do indeed demonstrate successful data cloaking. When the cloak is turned off, both cases show clear voltage transitions indicative of error-free transmission, but when the cloak is on, the output is nearly flat, completely hiding the data signal. Our experiments thus extend temporal cloaking to the realm of practical application, for consideration

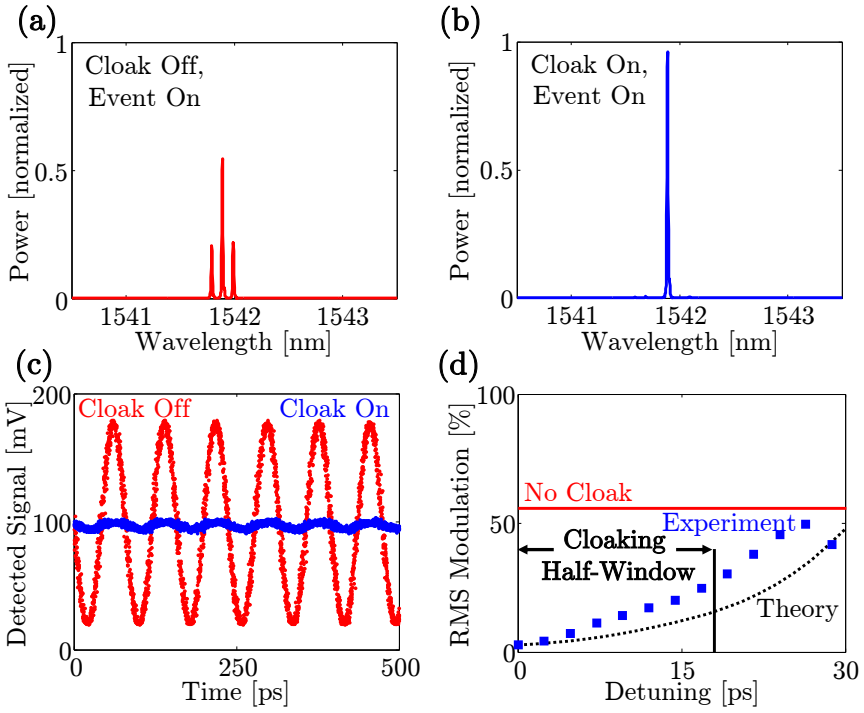

Fig. 2.6. Cloaking of sinusoidal modulation. (a) Output spectrum when the phase modulators are off and a sinusoid is applied to the intensity modulator. (b) Spectrum when the cloak is on, demonstrating removal of the sidebands in (a). Both spectra are normalized as in Fig. 2.4(c). (c) Corresponding temporal output. When the cloak is turned on, the previously high-contrast modulation is reduced to a flat line, hiding this event from an observer. (d) Measurement of the temporal cloaking window. The fractional modulation reaches one-half that in the uncloaked case at a detuning of 18 ps, for a total double-ended cloaking window of 36 ps, or 46% of the temporal period.

in high-speed telecommunications and with implications for secure communication in general.

2.4 Talbot Cloaking

Additionally, from a more general perspective, our results reveal a novel way to apply the Talbot effect: as a cloak in either space or time. Although the full

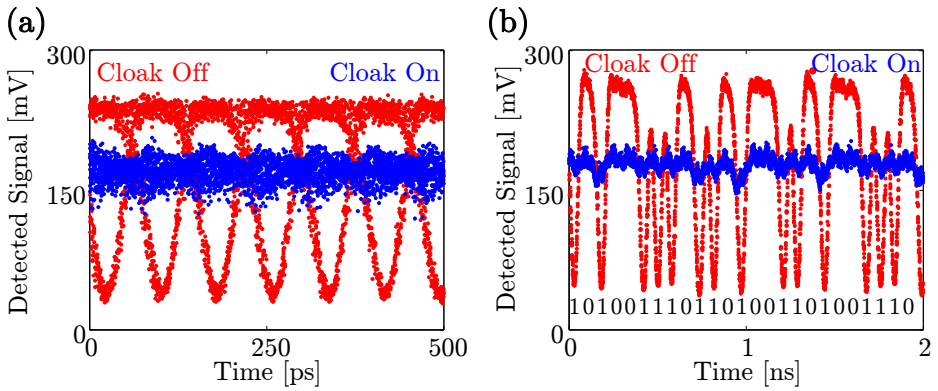

Fig. 2.7. Cloaking of data. (a) Temporal output when length $2^{31} - 1$ pseudorandom data are applied to the intensity modulator, measured on a sampling oscilloscope. The clear transitions between high and low data levels present when the cloak is off are completely removed when the phase modulators are on. (b) Output for a particular sequence of ones and zeros. Although the binary data specified on the bottom of the plot are clearly detected when the cloak is off, the voltage swings indicative of bit transmission are suppressed to a nearly flat line when the cloak is on.

cloak we have demonstrated utilizes time lensing and optical fiber to yield optimum performance, it would be possible to implement a simpler cloak based solely on Talbot self-imaging, for the holes that form after traversing the quarter-Talbot dispersion will naturally close themselves up on further propagation to the half-Talbot plane. What is especially interesting is that the spatial analogue of this simplified Talbot cloak—which consists of a single sign of dispersion—could then be realized in a simple uniform medium, requiring no negative-index materials.

In order to reinforce the connection between our temporal Talbot cloak and its analogue from space-time duality, we have constructed a spatial arrangement which highlights the key characteristics of this simplified Talbot cloak. The experimental setup is given in Fig. 2.8(a). A monochromatic C-band laser is emitted into free space and beam expanded so that it impinges on all 128 pixels of a spatial light modulator (SLM). On this device is programmed a sinusoidal phase mask with an amplitude of $\pi/4$ and 8 pixels per period, producing the spatial transmission grating of Fig. 2.2(a).

Based on device specifications, the spatial period is 800 μm, giving quarter- and half-Talbot distances in air of approximately 21 and 42 cm, respectively, for 1550-nm light. The measured intensity distribution at the quarter-Talbot plane [Fig. 2.8(b)] shows clearly the interference maxima and minima expected from theory, and a uniform-intensity field is indeed recovered at the half-Talbot mark [Fig. 2.8(c)]. For true phase and amplitude reconstruction, it would be necessary to place an additional SLM at the half-Talbot plane in order to remove the residual sinusoidal phase; however, in this simple experiment, we focus only on the intensity and do not tackle the complications associated with aligning two independent SLMs. As the object to cloak, we place an optical fiber (125-μm diameter) vertically in the quarter-Talbot plane within a null of the probing field and examine the intensity distribution at the half-Talbot plane. As shown in Fig. 2.8(d), when the SLM is programmed to flat phase, the fiber induces significant scattering, producing a sharp intensity gap in the measured field. But when the SLM is programmed with the sinusoidal phase specified previously, the output shows virtually no sign of the fiber whatsoever [Fig. 2.8(e)]; the obstruction is cloaked. Admittedly, the practical utility of this bulky cloak is doubtful, although other simplified spatial cloaks have recently received attention in the literature [45]. Yet notwithstanding questions of usefulness, our spatial Talbot cloak succeeds in bringing to light the unique insights of space-time duality, and we hope further exploration of the Talbot effect in both space and time will encourage advances in the field of optical cloaking.

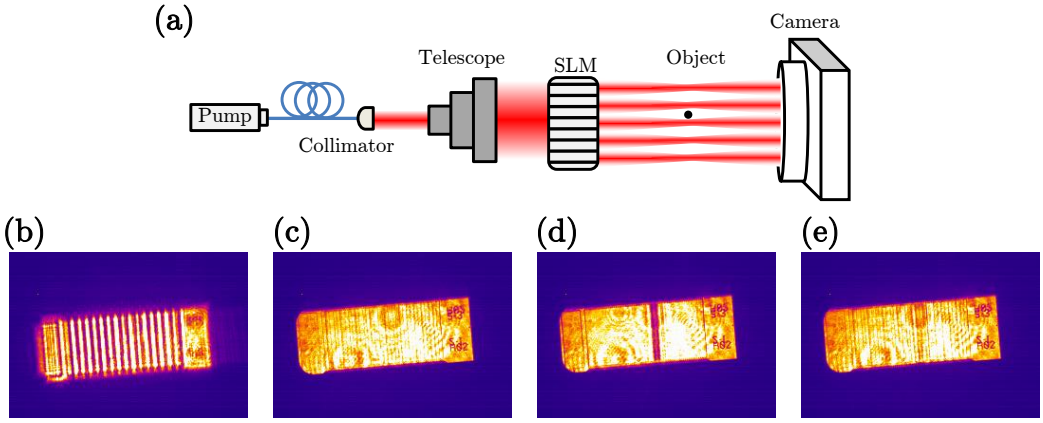

Fig. 2.8. Implementing a spatial Talbot cloak. (a) Experimental setup. A CW laser at 1550 nm is sent through a telescope for beam expansion and illuminates a 128-pixel SLM, programmed to impart sinusoidal transverse phase. Through Talbot self-imaging, the beam forms an array of intensity minima at $L_T/4$ and then recovers a uniform distribution at $L_T/2$, where a camera is used to measure the intensity. An object located in one of the field minima is ideally undectable by the camera. (b) Measured intensity at $L_T/4$ with no scattering object present but with the SLM programmed for sinusoidal modulation, showing clearly the development of interference fringes. (c) Intensity at $L_T/2$. The orginally uniform intensity is recovered as expected. (d) With the SLM programmed to flat phase and a wire placed at $L_T/4$, strong scattering is observed at $L_T/2$. (e) But when sinusoidal phase is applied, the presence of the wire is barely observable, demonstrating Talbot-based cloaking.

3. TEMPORAL CLOAKING IMPROVEMENTS FOR OPTICAL COMMUNICATION

3.1 Overview

The temporal cloak that we have demonstrated, while providing monumental performance gains, still offers room for improvement in several aspects. In this chapter, we summarize additional experiments which realize significant enhancements over the cloak described in Section 2.3. Specifically, we report modifications offering the new capability not only to hide optical data, but also to concurrently transmit it along another wavelength channel for subsequent readout, masking the information from one observer while directing it to another. Moreover, our new cloak succeeds in passing modulated data unscathed through a scrambling event, providing a new form of tampering resistance. Both examples launch a paradigm shift in temporal cloaking: instead of using time cloaks primarily to disrupt communication, we show how they can also improve data transmission, in turn greatly widening the range of possible applications in telecommunications.

3.2 The Improved Temporal Cloak

The previous experiments on time cloaking (described in Chapter 2 and work at Cornell [28]) exhibit the salient feature of a temporal cloak: the ability to hide the presence of some event from a probe that without the cloak would have been significantly modified. Accordingly, the event is effectively erased from the "history" recorded by the probe field [25, 26]. Yet one naturally could desire a more shrewd arrangement in which the event, while hidden from one optical beam, is perfectly

The results of this chapter have been published in [46].

visible to another probe, granting a desired recipient access to the history while cloaking it from an adversary. Such a feature is particularly suitable for optical communications, where the histories are streams of digital data which one may wish to secretly send to a distant party. Another restriction of the previous temporal cloaks is the limitation to continuous-wave input probe fields. Indeed, such fields do represent excellent test cases; possessing constant intensity over all time, they have no natural gaps in which events could take place and thus must be carefully manipulated to produce and close temporal holes. But of course it would be profitable to explore cloaking potential with non-continuous-wave inputs as well, both to examine the limits of current arrangements and explore possibilities for enhanced capabilities.

The new experiments address both of the previously mentioned shortcomings. First, we demonstrate a multi-wavelength (or WDM) cloak in which optical data are hidden from the probe at one of the input frequencies but accurately transmitted along another wavelength. Second, we consider non-continuous-wave input fields which consist of pseudorandom modulation, obtaining faithful transmission of this data even when subjected to high-speed interference from the event; in this fashion, the cloak furnishes anti-tampering capabilities, removing the impact of destructive modulation. These additions herald a fundamental change in how such cloaks can be viewed, for whereas previous time cloaks only *prevented* an observer from discovering the event, our new implementation reveals how time cloaks can be exploited to selectively *transmit* data as well. Considering the practical view that the most probable long-term applications of temporal cloaks will focus on improving current communication systems (e.g., as in [47]) rather than disrupting them, our results represent a key step forward.

In order to transition toward the first goal, a multi-wavelength cloak, we once again invoke space-time duality by drawing on a variation of Talbot interference, the so-called Lau effect [37, 48, 49]. Whereas the basic Talbot phenomenon requires a spatially coherent beam, the Lau effect considers instead a spatially incoherent source illuminating two gratings. Narrow slits on the first grating create a series of

individually coherent but mutually incoherent line sources, and each of these sources then generates a Talbot carpet after the second grating, all of which sum incoherently to give a total intensity that can correspond to a high-contrast image if the patterns are spatially aligned [37]. A temporal analogue of the Lau effect [50, 51] has previously been demonstrated for optical fields consisting of mutually incoherent narrowband lasers manipulated by an electro-optic modulator [52]. By tuning the laser frequency spacing, the delay between corresponding output time-domain waveforms can be adjusted to any amount within a period, from complete temporal coincidence to a half-period delay. And such delay control of temporal Talbot imaging is precisely what we require for a multi-wavelength time cloak. Individually, with no event present, each input wavelength should propagate through the cloak modulators and dispersion and emerge at the output as a continuous-wave signal; however, when an event is applied in the form of data modulation, one wavelength should escape without modulation, whereas the second should contain a faithful reproduction of the event data. To achieve this, we make use of the Lau effect and choose the wavelength separation so that both lasers yield compressed pulse trains which are delayed by one half-period relative to each other at the event modulator, ensuring that the data stream impacts only one of the two wavelength channels.

Temporal synchronization of both input wavelengths is achieved by precisely matching group delay through all dispersive elements. In general, a lossless second-order dispersive medium multiplies the incident frequency spectrum by the complex filter $H(\omega) = \exp[i\Phi_2(\omega - \omega_0)^2/2]$, where ω represents the angular frequency, Φ_2 the medium's dispersion coefficient, and ω_0 the center frequency of the expansion; in this form we have neglected an unimportant constant delay. The frequency-dependent group delay follows on evaluating the derivative of the filter phase: $\tau(\omega) = \frac{d}{d\omega}\arg H(\omega)$. Therefore, two carrier frequencies ω_1 and ω_2 will temporally separate on propagation through the medium by an amount $\Delta\tau = \tau(\omega_1) - \tau(\omega_2) = \Phi_2\Delta\omega$, where $\Delta\omega = \omega_1 - \omega_2$.

In order that both wavelengths precisely overlap in time at the second phase modulator in our cloak—location II in Fig. 3.1(b)—we require delay matching at a multiple of the temporal period, i.e.

$$|\Delta\tau_{\mathrm{CFBG}}| = \frac{2\pi p}{\omega_m}, \tag{3.1}$$

where p is a nonnegative integer and ω_m signifies the angular frequency of the electro-optic modulation (CFBG is short for "chirped fiber Bragg grating"). Even though we slightly detune the clock frequency from the Talbot condition in experiment, for conceptual simplicity here, we consider the CFBGs to apply quarter-Talbot dispersion, $|\Phi_2| = \pi/\omega_m^2$, which combined with the previous constraint fixes the possible frequency separations at

$$|\Delta\omega| = 2p\omega_m. \tag{3.2}$$

Thus any two lasers whose frequencies differ by an even multiple of the clock frequency will satisfy the first timing condition. Yet we also require that the waveforms at each wavelength be interleaved at the event—location III in Fig. 3.1(b)—so the relative delay through the optical fiber link must satisfy

$$|\Delta\tau_{\mathrm{fiber}}| = \frac{2\pi}{\omega_m}\left(q + \frac{1}{2}\right) \tag{3.3}$$

with q another nonnegative integer. Defining R as the ratio between CFBG and fiber dispersion coefficients $R = |\Phi_2^{(\mathrm{CFBG})}/\Phi_2^{(\mathrm{fiber})}|$, and recalling the first timing condition [Eq. (3.2)], one finds that both are met if p and q can be found such that

$$p = R\left(q + \frac{1}{2}\right). \tag{3.4}$$

Exact solutions exist only if the dispersion ratio R is an even integer; in our case, the fiber dispersion links were chosen previously for temporal compression, and so we are left with $R = 23.7$. We thus focus on the case $p = 12$, $q = 0.00633$, which exactly meets the CFBG timing condition but only approximately the interleaving requirement. Yet this deviation is minor; the interleaved pulse trains are now shifted by $\sim$51% of the temporal period instead of 50%, and since the second train need

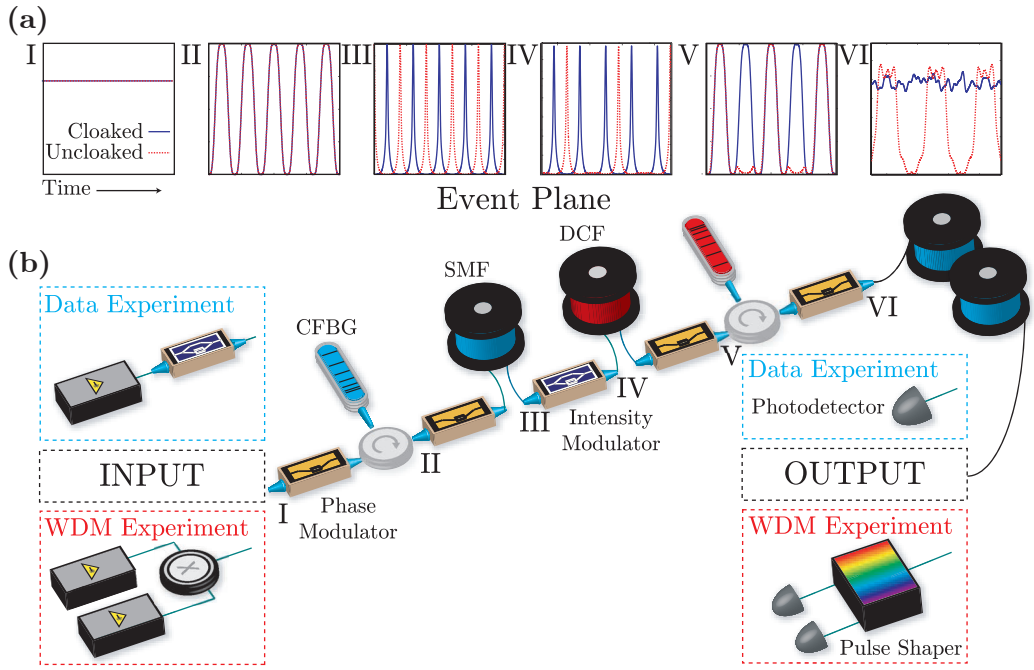

Fig. 3.1. Basic outline of improved temporal cloak. (a) Waveform progression for multi-wavelength cloak. Blue and red lines denote the intensity in the channels to be cloaked and to receive the data, respectively. Roman numerals represent various points in the circuit: (I) input to first phase modulator, (II) after quarter-Talbot dispersion, (III) at event plane just prior to event modulation, (IV) at event plane immediately after modulation, (V) before compensating quarter-Talbot dispersion, and (VI) at output. Only the red channel is impacted by the data modulation, which is an alternating zero-one sequence in this example. (b) Experimental setup. Boxes at the input and output show differences between the multi-wavelength cloak ("WDM Experiment") and data-as-input cloak ("Data Experiment"). Blue fibers and Bragg gratings signify anomalous dispersion, whereas red represents normal dispersion. CFBG: chirped fiber Bragg grating, SMF: single-mode fiber, DCF: dispersion-compensating fiber.

only *avoid* the event modulation—precise matching of phase is unnecessary—overall performance remains strong. Experimentally, our procedure is to first find a frequency spacing that gives approximately 50% interleaving and then fine-tune the separation to ensure temporal matching through the fiber Bragg gratings. For a more visual depiction, plots in Fig. 3.1(a) provide cartoons of the pulse trains derived from each

input frequency at various stages in the circuit, showing the overlap and interleaving necessary for our multi-wavelength cloak.

Figure 3.1(b) offers a schematic of the experimental setup, with the boxes labeled "WDM experiment" marking the input and output configurations for multi-wavelength cloaking. The central configuration of phase modulators and dispersion matches that in the previous cloak, although the order of normal and anomalous dispersion for the CFBGs has been arbitrarily reversed. We couple two independent monochromatic lasers into the cloaking circuit, one of whose wavelengths is tunable, and we propagate them through a combination of phase modulation and dispersion that converts them into interleaved pulse trains at the event plane. The event consists of intensity-modulated pseudorandom data which ideally impacts only one of the two trains, and after reconstruction the two wavelength channels are demultiplexed with a pulse shaper and then detected. As in Chapter 2, the extra dispersive fiber after the fourth phase modulator is added to achieve approximately zero net dispersion between the event and detector, so that turning the phase modulators off allows the event data to appear at the output without distortion. Moreover, when the cloak is operating, it is important to note that the amplitude of fluctuations in the output depends not only on the power in residual spectral sidebands (Fig. 2.5), but also the phase, for this determines whether contributions at the same radio frequency will add constructively or cancel each other out. Accordingly, we run all modulators at 12.11 GHz, rather than the 12.5 GHz estimated for ideal Talbot self-imaging, since we have found in simulation that this frequency gives slightly improved performance for our combination of dispersive elements. (The 12.71-GHz clock used in Chapter 2 was also chosen following such a numerical procedure, but subsequent simulations revealed 12.11 GHz as marginally more optimal.)

The measured spectrum when only the first two phase modulators are running is given in Fig. 3.2(a), with two distinct flattop combs generated about each carrier frequency. The broad bandwidth indicates that both combs will support short pulses at the event plane. To introduce the event, we apply inverted return-to-zero data

at the electrical input of the intensity modulator; when all phase modulators are off, both wavelength channels retain this data at the output, as evidenced by Fig. 3.2(b). However, turning on the cloak allows us to hide the data from one wavelength while continuing to broadcast it along the other; Fig. 3.2(c) gives the received signals when the phase modulators are on and optimized to cloak the short-wavelength channel. While the originally strong data modulation is removed on the output of the short-wavelength filter, the long-wavelength channel maintains high-contrast modulation. The received data has been converted to a non-return-to-zero format—which is as expected from theory due to the modulation and dispersion subsequent to the intensity modulator—but clear transitions between zero and one certify that the digital stream is fully maintained. Moreover, by shifting the event modulator's timing half a period, the roles of each channel can be reversed; as illustrated in Fig. 3.2(d), in this case the long-wavelength channel is now cloaked, with the short wavelength picking up the data.

Alternatively, instead of taking the event as the information-bearing quantity of interest—either to be hidden from or transmitted to another party—one may view the event as unwanted modulation which corrupts the input field; in this perspective, the cloak becomes a data *preserver* rather than a data *concealer*. Accordingly, it is profitable to consider data-modulated inputs rather than just continuous-wave fields which naturally lack any temporal information. At first glance, since the cloak is constructed assuming a single-frequency probe, it may appear that our design is inherently ill-suited for accepting a time-varying input. But the cloak itself operates at a high speed, so the requirement of constant intensity in effect means only that the input bandwidth be much smaller than the cloak repetition rate ω_m, or equivalently that the input field intensity must remain roughly constant over several clock periods. This intuitive picture implies that the cloak should still perform well with a data signal at the input, provided the data rate is sufficiently lower than ω_m.

We examine this idea experimentally with the setup of Fig. 3.1(b), but now using the transmitter and receiver in the "Data Experiment" insets. A single continuous-

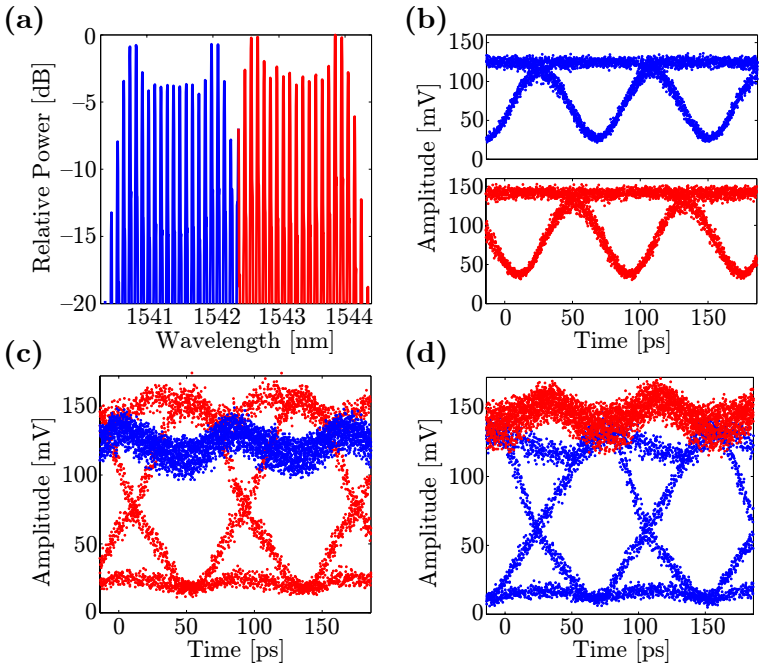

Fig. 3.2. Experimental results for multi-wavelength cloak. (a) Optical spectrum when the first two phase modulators are running. Colors indicate from which input laser a given spectral line was primarily generated, with blue representing the short-wavelength laser and red the long-wavelength one. (b) Received output for the short-wavelength (blue) and long-wavelength (red) demultiplexed channels when the event modulator is running and all phase modulators are off. (c) Received signals when the cloak is on and optimized to cloak the blue channel but transmit along the red. (d) Corresponding waveforms when the cloak is instead aligned to transmit data on the blue channel and cloak the red.

wave laser is modulated at some fraction of the clock frequency with non-return-to-zero data; explicitly, we consider clock-division factors of two, four, eight, and sixteen, corresponding to input data rates of 6.06 Gb/s, 3.03 Gb/s, 1.51 Gb/s, and 757 Mb/s, respectively. When the phase modulators are off, the high-speed event completely destroys the input data sequence; as illustrated in Fig. 3.3, the input data are nearly impossible to observe, corrupted by the fast modulation. Yet when the cloak is turned on, the input field is guided around this distorting modulation and recovered at the output, as indicated by the results in Fig. 3.4. For all input

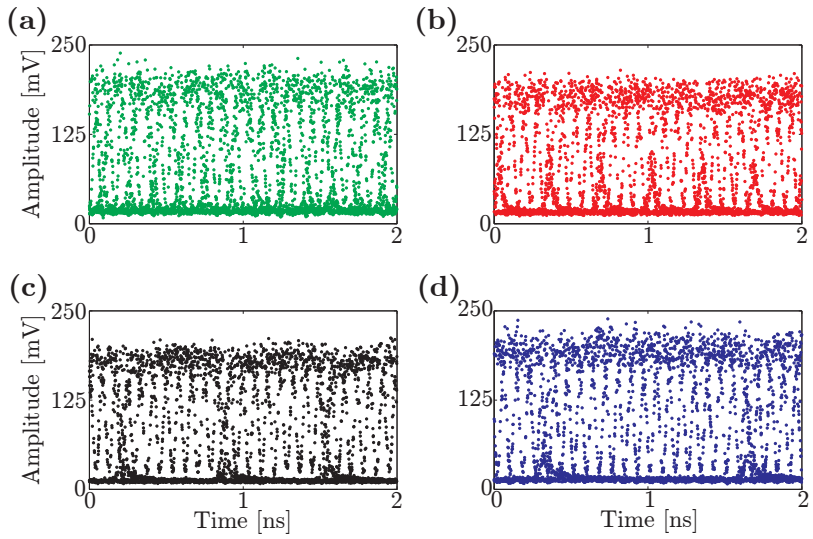

Fig. 3.3. Received signals for data-as-input experiment, when the cloak is off. (a) Input data rate is two times less than the clock. (b) Four times. (c) Eight times. (d) Sixteen times. In all cases, the high-speed event modulation at 12.11 GHz significantly corrupts the input data.

repetition rates, clear modulation at the correct period is now seen, with the event's impact reduced to residual noise at the high voltage level. This noise is strongest in the divide-by-two case, which makes sense, for the data rate is highest here and thus most removed from the continuous-wave ideal. Moreover, numerical simulations indicate only marginal performance improvement for data rates below the divide-by-eight case, which is qualitatively confirmed by the lack of significant noise reduction between Figs. 3.4(c) and (d).

For a more quantitative assessment of the cloak's utility as a data preserver, we also measure the received bit error ratio (BER) as a function of power, for all combinations of cloak and event operation. Unfortunately, because our high-speed BER tester (Agilent N4901B) is already required to generate the 12.11-GHz modulation serving as the event, we are forced to use a slower device for this analysis (HP 70004B), whose operation is limited to data rates below 3 Gb/s; for this reason, we can test only the divide-by-eight (1.51 Gb/s) and divide-by-sixteen (757 Mb/s) cases. Employing an

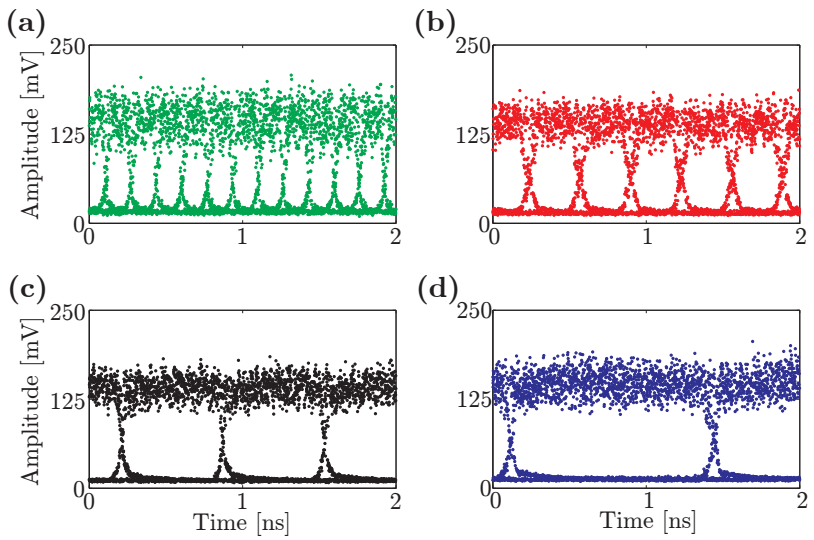

Fig. 3.4. Received signals for data-as-input experiment, when the cloak is on. (a) Input data rate is two times less than the clock. (b) Four times. (c) Eight times. (d) Sixteen times. Now the input sequences are fully recovered, with clear data signals observed at the appropriate repetition rates.

electrical amplifier to permit lower received optical powers, we measure the BER at the cloak output for the following four cases: (i) cloak off, event off; (ii) cloak off, event on; (iii) cloak on, event off; and (iv) cloak on, event on. The first case corresponds to the input passing through all elements with no additional phase or intensity modulation applied; therefore its BER should be lowest, providing a reference against which the other combinations can be compared. The second case should be worst, as it coincides with the corrupted data in Fig. 3.3—it is this situation for which the cloak is designed to offer significant error reduction when operating. Thus ideally, the cloak should: introduce negligible errors on its own, indicating that case (iii) should closely resemble case (i); and remove the errors in (ii), implying that (iv) should offer much lower BERs than (ii). Figure 3.5 displays the results of these tests, confirming the expected behavior. For both the divide-by-eight [Fig. 3.5(a)] and divide-by-sixteen [Fig. 3.5(b)] rates, negligible error increases are observed when the cloak is turned on and no interference is present, whereas the BER falls significantly when the cloak

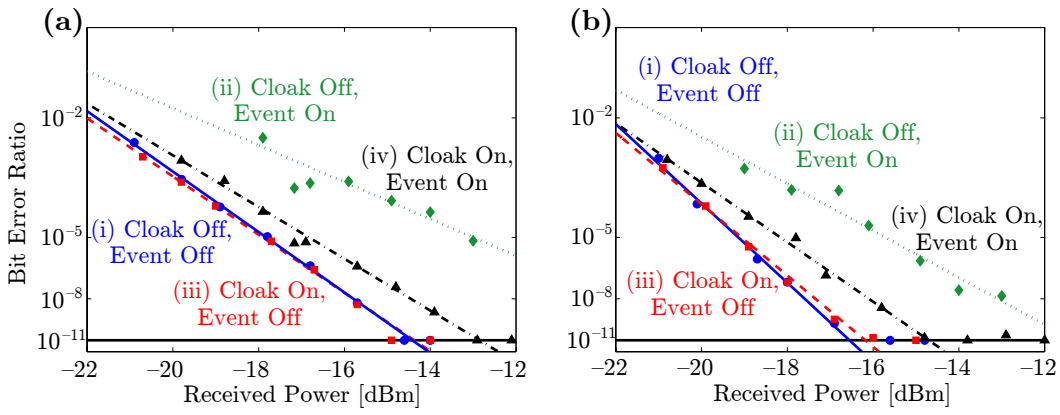

Fig. 3.5. BER test results. (a) Input data rate is one-eighth of the clock (1.51 Gb/s). (b) Data rate is one-sixteenth of the clock (757 Mb/s). Filled symbols indicate measurement results, and lines correspond to best fits. Error-free operation corresponds to a BER of 10^{-11}, marked by solid black lines; at our integration times, zero measured errors signify BERs $\leq 10^{-11}$ with 95% confidence [53].

is operating and the event is attacking the stream. As a consequence of the BER tester's low bandwidth, this improvement is perhaps less dramatic than expected; since the measurement electronics intrinsically filter out high-speed noise, the event corrupts the input to a lower extent than a higher-bandwidth detector would have indicated. Nevertheless, the general behavior is corroborated, with the cloak clearly improving signal quality in the face of the corrupting event.

3.3 Avenues for Future Improvement

The 46% cloaking window measured in the previous chapter is presently limited by the modulation index of the second and third phase modulators, which controls the total bandwidth of the combs in Figs. 2.4(a)and 3.2(a); a broader comb would permit compression to even narrower pulses and therefore facilitate wider cloaking windows. However, the modulation index is constrained by the maximum allowable RF input power, so at least with our current devices and layout, significant improvements in

the cloaking window appear unlikely. Yet cascading *multiple* phase modulators in series, instead of employing just one, could yield substantially wider cloaking. For example, in other work in our group [54], three phase modulators in series followed by compressing fiber were shown to produce pulses nearly eight times shorter than those demonstrated here; such short pulses imply cloaking windows around 90% should be possible by simply replacing the second and third phase modulators of Figs. 2.3 or 3.1 each with a set of modulators in series. Extending this technique to even more modulators to approach cloaking windows nearing 100% would prove costly, but should be possible; nothing intrinsically prevents it.

Another important characteristic of the cloak is the data rate at which it operates, which is fixed by the quarter-Talbot dispersion applied by the CFBG, and so for any given setup, our temporal cloak design functions only for a fixed event frequency. However, it is a simple matter to design a cloak at any desired frequency, by choosing the required dispersive links. In particular, this quality allows our cloaking arrangement to readily generalize to much higher data rates (e.g., 40 or 100 Gb/s), limited only by the capabilities of state-of-the-art modulators. In fact, since the Talbot length scales inversely with the square of the repetition frequency [Eq. (2.15)], higher data rates would in some ways be *easier* to implement, for they require shorter dispersive links. For these reasons we believe our temporal cloak is well-suited for the future of optical communication at ever-faster speeds.

As a consequence of timing drift from the thermo-optic effect in optical fiber, the RF phase shifters in our experiments require readjustment every few minutes under the conditions in the laboratory—an instability that would only be exacerbated in the myriad environments of long-haul telecommunications. Although active synchronization through software control could represent a viable solution, we propose a completely passive fix through replacing the two optical-fiber links of Fig. 2.3 by their equivalent CFBGs. This would remove the >1 km of silica fiber and in its place leave only a few meters, thereby making timing drift negligible compared to the RF period. Additionally, it would be valuable to pursue an arrangement composed

entirely of polarization-maintaining components. Currently, polarization controllers are required before every modulator, increasing both system loss and susceptibility to environmental fluctuations. Even better would be to implement the cloak with on-chip modulators, which would allow for precise engineering of the waveguides and dispersion. Indeed, we believe the stronger parasitic modulation in the two-wavelength case (Fig. 3.2) results from a slight dispersion mismatch, preventing the pulse trains at both wavelengths from maintaining timing synchronization at all modulators. Thus improved dispersion control would offer strong performance gains in the multi-wavelength case in particular.

More generally, we see two major avenues for progress on the multi-wavelength cloak's functionality. First, instead of considering only two wavelengths, it is feasible to directly extend our technique to several evenly spaced frequencies, in which cloaked and data-transmitting channels alternate along the grid. The total number of potential channels would be limited only by the acceptance bandwidth of the optical components. Second, programmable delay control would permit multi-wavelength cloaking with arbitrary laser channel frequencies, instead of the precisely chosen values in this experiment. This could in principle be implemented by placing pulse shapers before and after each of the inner phase modulators in Fig. 3.1(b) (e.g., at locations II, III, IV, and V). By applying spectral phase shifts corresponding to the desired group delays, it would then be possible to control which wavelength channels are cloaked and which pick up data, with complete programmability and no restriction to particular frequency spacings. Implementation of this scheme would demand relatively fine spectral resolution, roughly on the order of the cloak repetition frequency, in order to permit the half-period shifts necessary to move a channel's delay from cloaked to uncloaked positions. Nevertheless, systems like the current one designed only for particular wavelength separations could find use even without the added capabilities furnished by multiple pulse shapers, as certain optical communication techniques such as orthogonal frequency-division multiplexing already require precisely spaced channels at multiples of the symbol rate.

3.4 Conclusion

In summary, in this chapter we have demonstrated two new uses for temporal cloaking in high-speed telecommunications. The first, a multi-wavelength cloak, allows data which is hidden from one wavelength channel to be transmitted along an alternative one; in the second, a corrupting event is cloaked from an input digital message, thereby allowing faithful transmission of the incoming data past an aggressive modulation signal. Both realizations offer new perspectives on temporal cloaking for improving data communication systems rather than disturbing them. It will be interesting to explore how this two-sided nature of time cloaking may be exploited in future developments in this field, whether in the exotic quest for a full space-time cloak or in more mundane—but no less important—efforts to improve optical communications.

4. BIPHOTON PULSE SHAPING THEORY

4.1 Background

The extensive research interest in biphotons stems from the quantum mechanical entanglement they possess, which endows such photon pairs with their nonclassical—and often bizarre—properties. Mathematically speaking, entanglement results when the total quantum state cannot be expressed as the product of individual states for the constituent subsystems [55]; the total state can only be represented as a *linear combination* of such non-entangled, or separable, states. Measurements on two entangled particles can be strongly correlated, even when they are arbitrarily far apart, allowing, for example, simultaneously narrow momentum and position correlations. Such nonlocality was perhaps most pointedly critiqued by Einstein, Podolsky, and Rosen (EPR) in 1935, in which they concluded that quantum mechanics must be incomplete, for it violated the ostensibly sound axiom of local realism [56]. Yet it was not until the work of J. S. Bell in the 1960s that this philosophical debate could enter the realm of experiment. In his seminal 1964 paper [57], Bell derived an inequality for the correlations between two particles which all local hidden variable theories must satisfy, but which an entangled quantum state could violate. And although originally specialized to spin-1/2 atoms, the majority of current Bell tests utilize instead entangled photons generated through spontaneous parametric downconversion (SPDC) [58]. Not only are biphotons relatively simple to generate at room temperature, requiring only a laser and nonlinear crystal, but they can also travel long distances in free space or optical fiber with minimal decoherence—essential to achieve true nonlocality or distribute a secret key between distant users.

It is precisely this second application, quantum communication, which motivates the biphoton experiments we have conducted. Interestingly, neither the original pro-

posal [59] nor current schemes based on weak coherent states [60, 61] actually require entanglement for operation; however, QKD protocols utilizing entangled photons do remain a major subject of research. For not only do entanglement-based protocols mitigate the issues of empty pulses and information leakage which plague single-photon systems [60]; they also provide a direct connection to the EPR paradox and the fundamental weirdness of quantum mechanics. Indeed, the first proposal for entanglement-based QKD relied on violation of Bell's inequality to verify security [62], and photons entangled in polarization [63], time bins [64–67], or time and frequency [68–70]—just to name a few—have all been considered for secure key distribution. The nature of such QKD protocols is beyond the scope of this work; for further information, the reader is directed to the reviews in [60, 61]. Here we focus instead on novel ways to manipulate these entangled states at the fundamental level, drawing specifically on established technology in classical pulse shaping. We therefore believe our work provides a springboard for new applications in the development of quantum cryptography, by extending techniques previously relegated to classical optics.

Since its development in the 1980s [4], Fourier-transform pulse shaping of femtosecond laser pulses has revolutionized the field of ultrafast optics, with applications ranging from coherent control of chemical reactions to RF photonics, wavelength-selective switching to single-cycle pulse generation [2,3]. In the standard arrangement, a broadband pulse is spectrally dispersed by a diffraction grating, thereby separating each of the constituent frequencies. By placing a programmable liquid-crystal mask in the focal plane, it is possible to control the amplitude and phase of each frequency component independently; when the frequencies are recombined in a dispersion-free fashion (made possible by a $4f$ geometry [4]) an essentially arbitrary time-domain field can be constructed, limited only by spectral resolution. In this way complicated fields which vary on a femtosecond timescale can be readily synthesized, a feat impossible with even the fastest electronic modulators. This fine temporal control is well suited for any broadband optical field, including classical incoherent light [71]

and, most importantly for us, biphotons. As first demonstrated in 2005 [72], a pulse shaper can be used to modify the temporal correlations of entangled photons in a fashion analogous to classical arbitrary waveform generation. Over the past decade, only a handful of biphoton pulse shaping experiments with spatial light modulators have been realized in other groups (e.g., [73–75]), and none has considered biphotons in the telecommunications band around 1550 nm, the optimal regime for long-haul QKD along optical fiber. We accordingly have sought to exploit classical telecom pulse-shaping methods and technology to greatly enhance the capabilities for biphoton manipulation, carrying out several key experiments demonstrating its potential.

4.2 Time-Frequency Entangled Photons

The biphotons we examine in experiment are obtained through SPDC of a narrowband pump field. In this interaction, a single pump photon decays into two daughter photons, traditionally called "signal" and "idler," such that energy is conserved; Fig. 4.1(a) provides a sketch of this process. Since both photons are created at the same instant in time and derive from a photon with well-defined energy, they are highly correlated in *both* time and frequency, even though individually each photon may be found in a wide range of times or frequencies. For example, a frequency measurement of one photon might yield a value anywhere within a several terahertz range; but once this frequency is known, that of its partner is fixed to the value required to satisfy energy conservation, which is as narrowband as the CW pump photon (perhaps megahertz or less). The strong correlations in time and frequency are highlighted in Figs. 4.1(b) and (c), defying the typical inverse relationship between time and frequency spread. Such joint correlation amid individual randomness provides the basis for recently proposed time-frequency QKD protocols aimed at distilling multiple bits per photon [68–70].

This heuristic discussion can be made more rigorous with quantum optical theory. The positive and negative complex electric fields introduced previously must now be

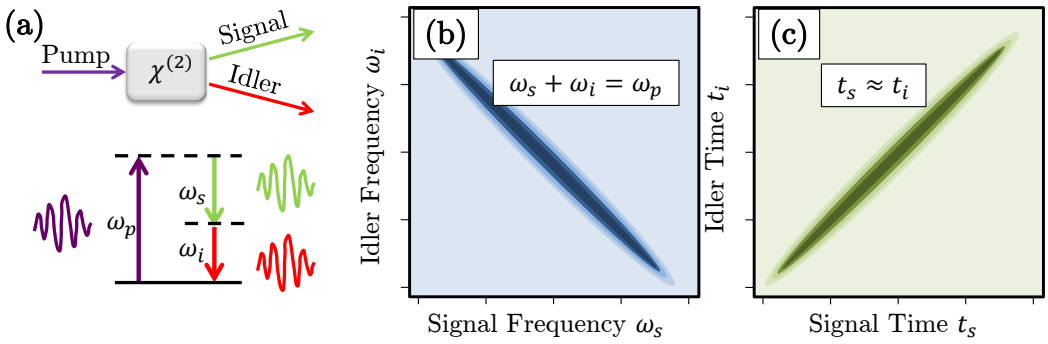

Fig. 4.1. Basics of time-frequency entangled photons. (a) Schematic of SPDC generation process. Signal and idler frequencies must sum to that of the pump to satisfy energy conservation. (b) Joint spectral correlations. (c) Joint temporal correlations. Even though individual photons have a wide spread of spectro-temporal content, they are highly correlated with their partner.

taken as quantum mechanical operators. In the typical free-space derivation [55], a quantization volume is introduced and all three spatial dimensions must be considered. But since light is confined to an optical waveguide in all of our experiments, we need to consider only one spatial dimension. Moreover, the formalism is made more transparent by considering a continuum of modes directly (that is, letting the quantization dimension approach infinity from the start). The positive, single-polarization electric field operator in the Heisenberg picture for a waveguide geometry is then given by [76]

$$\hat{E}^{(+)}(z,t) = i\int_0^\infty d\omega \left[\frac{\hbar\omega}{4\pi\epsilon_0 cnS}\right]^{1/2} \hat{a}(\omega)e^{i(kz-\omega t)}, \tag{4.1}$$

where the negative-frequency field follows by taking the Hermitian conjugate; i.e., $\hat{E}^{(-)}(z,t) = [\hat{E}^{(+)}(z,t)]^\dagger$. Here S is the effective transverse area, and $n = n(\omega)$ is the waveguide index of refraction, defined so that the propagation constant k satisfies $k = n(\omega)\omega/c$. These quantities account for all effects of the waveguide geometry, and so, just as in the discussion surrouding Eq. (2.5), we are justified in ignoring the transverse field distribution; its only impact is to modify the propagation constant from that of a plane wave to $k(\omega)$ calculated from an eigenvalue equation [1]. The

annihilation operator $\hat{a}(\omega)$ has the effect of destroying one photon at frequency ω, and its Hermitian conjugate $\hat{a}^\dagger(\omega)$ creates a photon at ω. For a particular spatial mode, they satisfy the relations [76]

$$[\hat{a}(\omega), \hat{a}^\dagger(\omega')] = \delta(\omega - \omega'), \tag{4.2}$$

$$[\hat{a}(\omega), \hat{a}(\omega')] = 0, \tag{4.3}$$

$$\hat{a}(\omega)|\omega'\rangle = \delta(\omega - \omega')|\text{vac}\rangle, \tag{4.4}$$

and

$$\hat{a}^\dagger(\omega)|\text{vac}\rangle = |\omega\rangle. \tag{4.5}$$

The vacuum state is represented by $|\text{vac}\rangle$, and $|\omega\rangle$ is the Dirac-normalized state consisting of one photon at frequency ω.

To describe evolution of the quantum state and our measurements conducted on it, we employ the interaction picture, in which the quantum state evolves in time through an interaction Hamiltonian and the operators according to the Hamiltonian of the isolated electromagnetic field [55]. In this way, we can separate generation of the entangled state from subsequent propagation through any optical elements, the convenience of which will become evident later when we treat the effect of optical filtering. Specifically, the interaction Hamiltonian describing SPDC in a nonlinear waveguide is given by [77]

$$\hat{H}_I = \epsilon_0 \int_{\mathcal{V}} d^3\vec{r}\,\gamma(z)\hat{E}_p^{(+)}(z,t)\hat{E}_s^{(-)}(z,t)\hat{E}_i^{(-)}(z,t) + \text{h.c.}, \tag{4.6}$$

where p, s, and i denote the pump, signal, and idler fields, respectively, and integration is taken over the volume of the interaction region. The shorthand h.c. denotes the Hermitian conjugate of the first term, and $\gamma(z)$ is the relevant nonlinear coefficient, assumed dispersionless over the optical bandwidth considered; it can, however, vary along the longitudinal direction, reflecting the fact that the waveguides used in experiments are periodically poled. Because the pump is an intense classical field, we can treat its operator as a complex number, oscillating at the pump frequency $2\omega_0$:

$$\hat{E}_p^{(+)}(z,t) = E_0 e^{i(k_p z - 2\omega_0 t)}, \tag{4.7}$$

where $k_p = k(2\omega_0)$. We define the signal field as containing frequency content greater than ω_0, and the idler less than ω_0, so specializing Eq. (4.1) and factoring out the slowly varying dependence on frequency, we take as our field operators

$$\hat{E}_s^{(-)}(z,t) = -i\left[\frac{\hbar\omega_0}{4\pi\epsilon_0 c n_0 S}\right]^{1/2}\int_0^\infty d\Omega\,\hat{a}_s^\dagger(\omega_0+\Omega)e^{-i(k_s z-\omega_0 t-\Omega t)} \tag{4.8}$$

and

$$\hat{E}_i^{(-)}(z,t) = -i\left[\frac{\hbar\omega_0}{4\pi\epsilon_0 c n_0 S}\right]^{1/2}\int_0^{\omega_0} d\Omega'\,\hat{a}_i^\dagger(\omega_0-\Omega')e^{-i(k_i z-\omega_0 t+\Omega' t)}, \tag{4.9}$$

where $k_s = k(\omega_0+\Omega)$, $k_i = k(\omega_0-\Omega')$, and $n_0 = n(\omega_0)$. We also express $\gamma(z)$ as a Fourier series to reflect the poling [78]:

$$\gamma(z) = \sum_m \gamma_m e^{iK_m z}. \tag{4.10}$$

In the interaction picture, keeping only the lowest-order correction to the input vacuum gives the perturbed quantum state [55]

$$|\Psi\rangle = M|\text{vac}\rangle_s|\text{vac}\rangle_i + \frac{1}{i\hbar}\int_0^t dt'\,\hat{H}_I(t')|\text{vac}\rangle_s|\text{vac}\rangle_i, \tag{4.11}$$

where $M\sim 1$ is added to allow for proper normalization of $|\Psi\rangle$. Taking the waveguide to extend from $z=-L$ to $z=0$, and assuming that only one poling wavenumber K_m from Eq. (4.10) is close to $k_s+k_i-k_p$, plugging in Eqs. (4.7)-(4.10) into Eq. (4.6) and then this into Eq. (4.11) gives

$$\begin{aligned}|\Psi\rangle =& M|\text{vac}\rangle_s|\text{vac}\rangle_i \\ &- \frac{E_0\gamma_m\omega_0}{4\pi i c n_0}\int_0^\infty d\Omega\int_0^{\omega_0} d\Omega'\int_{-L}^0 dz\,e^{-i\Delta k z}\int_0^t dt'\,e^{i(\Omega-\Omega')t'}|\omega_0+\Omega\rangle_s|\omega_0-\Omega'\rangle_i,\end{aligned} \tag{4.12}$$

with the phase mismatch defined as

$$\Delta k(\Omega,\Omega') = k_s + k_i - k_p - K_m. \tag{4.13}$$

In the limit of large t, the last integral approaches $2\pi\delta(\Omega-\Omega')$, which yields finally

$$|\Psi\rangle = M|\text{vac}\rangle_s|\text{vac}\rangle_i + \int_0^{\omega_0} d\Omega\,\phi(\Omega)|\omega_0+\Omega\rangle_s|\omega_0-\Omega\rangle_i, \tag{4.14}$$

with

$$\phi(\Omega) = \frac{iE_0\gamma_m L\omega_0}{2cn_0} e^{i\Delta kL/2} \mathrm{sinc}\frac{\Delta kL}{2}. \tag{4.15}$$

Δk is evaluated at $\Omega' = \Omega$ and $\mathrm{sinc}\, x = \sin x/x$. The above state expresses mathematically the intuitive argument presented earlier: the biphoton consists of a superposition of signal and idler spectral modes with the property that their frequencies sum to that of the pump. Now, however, we have an explicit expression for the weighting of the possible spectral pairs. Therefore, with knowledge of the waveguide poling and effective refractive index—information which is provided by our collaborators at Stanford University—we can predict the generated quantum state in our experiments through Eqs. (4.14) and (4.15).

And not only do these equations reveal the overall shape of the biphoton state; they also facilitate a quantitative estimate of the downconversion efficiency, the probability for a given pump photon to spontaneously decay into an entangled photon pair. To derive this relationship, we calculate the mean signal-photon generation rate and compare it to the pump photon flux. The relevant signal flux operator at the output face of the crystal ($z = 0$) can be written in terms of electric field operators as

$$\hat{\mathcal{F}}_s = \frac{2n_0\epsilon_0 cS}{\hbar\omega_0} \hat{E}_s^{(-)}(0,t)\hat{E}_s^{(+)}(0,t), \tag{4.16}$$

which corresponds to the field power divided by photon energy, giving the desired units of inverse time. For the coherent-state pump field, the photon flux is simply the c-number

$$\mathcal{F}_p = \frac{n_p\epsilon_0 cS}{\hbar\omega_0}|E_0|^2, \tag{4.17}$$

where $n_p = n(2\omega_0)$. Thus we define the SPDC efficiency η_{SPDC} via the relation

$$\begin{aligned} \eta_{\mathrm{SPDC}} &= \frac{\langle\Psi|\hat{\mathcal{F}}_s|\Psi\rangle}{\mathcal{F}_p} \\ &= \frac{2n_0}{n_p|E_0|^2}\langle\Psi|\hat{E}_s^{(-)}(0,t)\hat{E}_s^{(+)}(0,t)|\Psi\rangle. \end{aligned} \tag{4.18}$$

Utilizing the expression for the field operator in Eq. (4.8), along with the biphoton state in Eqs. (4.14) and (4.15), we arrive at the efficiency

$$\eta_{\mathrm{SPDC}} = \frac{\hbar\omega_0^3\gamma_m^2 L^2}{8\pi\epsilon_0 c^3 n_0^2 n_p S}\int_0^{\omega_0} d\Omega\,\mathrm{sinc}^2\frac{\Delta kL}{2}. \tag{4.19}$$

The place-holding constant γ_m can be written in terms of the effective second-order nonlinearity d_{eff} according to

$$\gamma_m = -4d_{\mathrm{eff}}, \tag{4.20}$$

a relationship derivable by translating the expressions of, e.g., [79, 80] to our formalism. This yields finally

$$\eta_{\mathrm{SPDC}} = \frac{2\hbar\omega_0^3 d_{\mathrm{eff}}^2 L^2}{\pi\epsilon_0 c^3 n_0^2 n_p S}\int_0^{\omega_0} d\Omega\,\mathrm{sinc}^2\frac{\Delta kL}{2}, \tag{4.21}$$

in agreement with the result in [80] obtained following an alternative method. For our periodically poled lithium niobate (PPLN) source, the effective nonlinearity satisfies $d_{\mathrm{eff}} = 2d_{33}/\pi$, where $d_{33} = 31.5$ pm/V and the factor of $2/\pi$ accounts for the poling [78]; plugging in these and the remaining parameters for a 52-mm-long guide, Eq. (4.21) predicts a downconversion efficiency of about 4×10^{-5}, close to the $\sim 10^{-5}$ actually observed in experiment. Such quantitative agreement provides additional validation of the interaction-picture-based approach which we have adopted here.

4.3 Theory of Biphoton Pulse Shaping

Measurement of the above biphoton state is achieved through photodetection of the signal and idler photons, typically with single-photon avalanche photodiodes. To relate this process to the quantum optical formalism introduced in the last section, we follow the heuristic argument first presented by Glauber [81]. (For a more rigorous development, refer to Ch. 14 of [55].) First we note that the detection of the signal photon at time t_1 and the idler at t_2 modifies the initial field state $|\Psi\rangle$ so that its inner product with the final state $|f\rangle$ is given by

$$\langle f|\hat{E}_s^{(+)}(t_1)\hat{E}_i^{(+)}(t_2)|\Psi\rangle. \tag{4.22}$$

The probability of signal and idler detection is thus obtained (up to a proportionality constant) by taking the modulus squared of the above matrix element and summing over all final states of the field. We therefore define the fourth-order correlation function as this quantity:

$$\begin{aligned}\Gamma^{(2,2)}(t_1,t_2) &= \sum_f |\langle f|\hat{E}_s^{(+)}(t_1)\hat{E}_i^{(+)}(t_2)|\Psi\rangle|^2 \\ &= \sum_f \langle\Psi|\hat{E}_i^{(-)}(t_2)\hat{E}_s^{(-)}(t_1)|f\rangle\langle f|\hat{E}_s^{(+)}(t_1)\hat{E}_i^{(+)}(t_2)|\Psi\rangle \\ &= \langle\Psi|\hat{E}_i^{(-)}(t_2)\hat{E}_s^{(-)}(t_1)\hat{E}_s^{(+)}(t_1)\hat{E}_i^{(+)}(t_2)|\Psi\rangle, \end{aligned} \tag{4.23}$$

where the last line follows from the completeness of the final states. This correlation function is the primary quantity with which we characterize the quantum field in experiment, measured either by comparing the detections on separate photodiodes or counting sum-frequency photons in ultrafast coincidence detection.

A convenient simplification occurs when the state $|\Psi\rangle$ contains no more than two photons, for then the operator $\hat{E}_s^{(+)}(t_1)\hat{E}_i^{(+)}(t_2)$ acting on $|\Psi\rangle$ produces at most a result proportional to the vacuum state (it could also give zero), meaning that we can with impunity insert the operator $|\text{vac}\rangle\langle\text{vac}|$ into the expression for the correlation function:

$$\begin{aligned}\Gamma^{(2,2)}(t_1,t_2) &= \langle\Psi|\hat{E}_i^{(-)}(t_2)\hat{E}_s^{(-)}(t_1)|\text{vac}\rangle\langle\text{vac}|\hat{E}_s^{(+)}(t_1)\hat{E}_i^{(+)}(t_2)|\Psi\rangle \\ &= |\langle\text{vac}|\hat{E}_s^{(+)}(t_1)\hat{E}_i^{(+)}(t_2)|\Psi\rangle|^2 \\ &= |\psi(t_1,t_2)|^2, \end{aligned} \tag{4.24}$$

where we have defined the biphoton wavepacket [82]

$$\psi(t_1,t_2) = \langle\text{vac}|\hat{E}_s^{(+)}(t_1)\hat{E}_i^{(+)}(t_2)|\Psi\rangle. \tag{4.25}$$

This quantity is linear in signal and idler fields and can be viewed as a "wave function" whose modulus squared gives the probability density for joint photon detection. Yet this function is by no means a solution of the Schrödinger equation; it is simply a useful matrix element. And so to complete the theoretical description of biphoton

pulse shaping, we need only compute the biphoton wavepacket for the state in Eq. (4.14), when the signal and idler photons are spectrally filtered. Specifically, we apply the complex filters $H_s(\omega)$ to the signal photon and $H_i(\omega)$ to the idler photon after the nonlinear waveguide (which include any phase accrued through propagation through optical fiber). Since these operators transform just like their classical counterparts, the effect of filtering is included simply by multiplication in the spectral domain, leaving the fields at the detectors

$$\hat{E}_s^{(+)}(t_1) = i\int_{\omega_0}^{\infty} d\omega_s \left[\frac{\hbar\omega_s}{4\pi\epsilon_0 cnS}\right]^{1/2} H_s(\omega_s)\hat{a}_s(\omega_s)e^{-i\omega_s t_1} \tag{4.26}$$

$$\hat{E}_i^{(+)}(t_1) = i\int_{0}^{\omega_0} d\omega_i \left[\frac{\hbar\omega_i}{4\pi\epsilon_0 cnS}\right]^{1/2} H_i(\omega_i)\hat{a}_i(\omega_i)e^{-i\omega_i t_2}. \tag{4.27}$$

Taking $t_1 = t+\tau$ and $t_2 = t$ and using the state in Eq. (4.14), we have the wavepacket

$$\begin{aligned}\psi(t+\tau,t) =& \langle \text{vac}| i\int_{\omega_0}^{\infty} d\omega_s \left[\frac{\hbar\omega_s}{4\pi\epsilon_0 cnS}\right]^{1/2} H_s(\omega_s)\hat{a}_s(\omega_s)e^{-i\omega_s(t+\tau)} \\ &\times i\int_{0}^{\omega_0} d\omega_i \left[\frac{\hbar\omega_i}{4\pi\epsilon_0 cnS}\right]^{1/2} H_i(\omega_i)\hat{a}_i(\omega_i)e^{-i\omega_i t} \\ &\times \left(M|\text{vac}\rangle_s|\text{vac}\rangle_i + \int_0^{\omega_0} d\Omega\, \phi(\Omega)|\omega_0+\Omega\rangle_s|\omega_0-\Omega\rangle_i\right),\end{aligned} \tag{4.28}$$

which represents the probability amplitude for detecting the signal photon a time τ after detecting the idler. Extracting slowly varying factors and rearranging the order of integration, we get

$$\begin{aligned}\psi(t+\tau,t) =& -\frac{\hbar\omega_0}{4\pi\epsilon_0 cn_0 S}\int_0^{\omega_0} d\Omega \int_{\omega_0}^{\infty} d\omega_s \int_0^{\omega_0} d\omega_i\, \phi(\Omega)H_s(\omega_s)H_i(\omega_i)e^{-i[\omega_s(t+\tau)+\omega_i t]} \\ &\times \langle \text{vac}|\hat{a}_s(\omega_s)\hat{a}_i(\omega_i)|\omega_0+\Omega\rangle_s|\omega_0-\Omega\rangle_i.\end{aligned} \tag{4.29}$$

Using the property of the annihilation operator in Eq. (4.4), the matrix element is found to be $\delta(\omega_s-\omega_0-\Omega)\delta(\omega_i-\omega_0+\Omega)$, allowing trivial integration over ω_s and ω_i:

$$\psi(t+\tau,t) = -\frac{\hbar\omega_0}{4\pi\epsilon_0 cn_0 S}e^{-i\omega_0(2t+\tau)}\int_0^{\omega_0} d\Omega\, \phi(\Omega)H_s(\omega_0+\Omega)H_i(\omega_0-\Omega)e^{-i\Omega\tau}. \tag{4.30}$$

The unimodular dependence on t can be neglected, since it vanishes upon calculating the correlation function $\Gamma^{(2,2)}$, and the unimportant overall constant can be absorbed into $\phi(\Omega)$, leaving a wavepacket which depends only on the time difference τ:

$$\psi(\tau) = \int_0^\infty d\Omega\, \phi(\Omega) H_s(\omega_0 + \Omega) H_i(\omega_0 - \Omega) e^{-i\Omega\tau}. \tag{4.31}$$

(Allowing the integral to extend to ∞ is justified because the phase-matching function $\phi(\Omega)$ is negligible for $\Omega > \omega_0$.) Analogous to a classical coherent pulse, the biphoton correlation function can be shaped through programmable spectral filtering per Eq. (4.31). But as a consequence of spectral entanglement, the signal and idler filters are multiplied together and evaluated at complementary frequencies in the integrand. In this way the filtering of one photon can be "undone" by filtering the other—a fascinating characteristic which we exploit later in dispersion cancellation and orthogonal coding experiments.

In summary, we have derived the fourth-order biphoton correlation function for the case of monochromatic SPDC in a nonlinear waveguide, starting from basic quantum optical theory. With knowledge of the waveguide dispersion and poling, we can calculate the functional form of the phase-matching function using Eq. (4.15). Then the signal and idler spectral filters, which can be programmed directly on a pulse shaper, permit calculation of the wavepacket $\psi(\tau)$ [Eq. (4.31)]. Finally, the correlation function, which is proportional to the probability density of detecting the signal photon delayed by τ from the idler, follows from $\Gamma^{(2,2)}(\tau) = |\psi(\tau)|^2$. A major goal of our experimental work is to explore new spectral coding techniques made possible by high-resolution telecom pulse shaping technology, effectively extending the range of filters $H_s(\omega)$ and $H_i(\omega)$ available in quantum optical applications. The majority of the experiments described in the following chapters can thus be viewed as special cases of the general biphoton shaping formula, Eq. (4.31).

4.4 Setup for Biphoton Generation

For biphoton generation, we employ a PPLN waveguide [83, 84], chosen for its exceptionally high conversion efficiency [85,86] and fabricated by our collaborators at Stanford University. With the exception of a 67-mm-long waveguide used for SPDC in Section 6.5, every sample considered in this dissertation is 52 mm in length. The poling period is designed to achieve phase matching for degenerate downconversion of a pump at ∼774 nm when the PPLN chip is heated to 140° C; operating at such elevated temperature mitigates the deleterious effects of photorefraction and maximizes the permissible input power level. A schematic of the basic biphoton generation stage is presented in Fig. 4.2(a). We couple a CW laser (New Focus TLB-6712) tuned to the phase-matched wavelength around 774 nm into the PPLN waveguide; approximately 10^{-5} of the incoming photons are converted to entangled photons around 1548 nm (193.8 THz). The waveguide output is passed through three glass filters (Schott RG1000) to remove the residual pump light, and the biphotons are then coupled into optical fiber. Both the signal and idler occupy the same spatio-polarization mode, so the only means to distinguish them is by frequency, in accordance with the theoretical formulation in the previous section. A typical optical spectrum of the SPDC emission is presented in Fig. 4.2(b), acquired at a resolution of 250 GHz. The signal photon corresponds to the high-frequency content (to the right of the dotted line) and the idler to the low-frequency content (left of the line). The spectrum is extremely broad, with a 3-dB bandwidth of 8.25 THz, which is filtered down to the nearly flat portion by the pulse shaper in subsequent experiments.

We have conducted two main classes of experiments with this biphoton source, distinguished by the method of photon detection. One set utilizes a pair of single-photon detectors and *electronically* correlates the arrival times to determine photon coincidences; the other set employs biphoton sum-frequency generation (SFG) to determine photon coincidences *optically*. Although the SFG-based scheme furnishes the finest temporal resolution, the first method is simpler to implement and by far

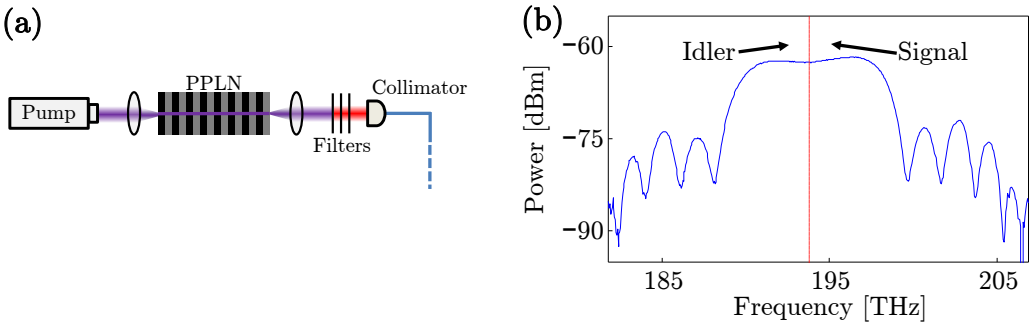

Fig. 4.2. PPLN-based biphoton source. (a) Schematic of generation process. Biphotons are created through spontaneous decay of monochromatic pump photons in a PPLN waveguide. After removing the residual pump light with filters, the biphotons are coupled into optical fiber for subsequent manipulation and characterization. (b) Typical optical spectrum of generated SPDC photons, measured after the collimator in (a) at 250-GHz resolution.

the more common in practice; therefore we consider the slow-detection experiments in the next chapter, proceeding to the more exotic ultrafast experiments in Chapter 6.

5. EXPERIMENTS WITH ELECTRONIC COINCIDENCE DETECTION

5.1 Experimental Arrangement

A schematic of the full experimental setup, including generation, manipulation, and detection, for the first class of biphoton shaping tests is presented in Fig. 5.1(a). After the collimator, the biphotons are sent into a fiber-coupled commercial pulse shaper (Finisar WaveShaper 4000S/X [5]), which offers programmable amplitude and phase control at 20-GHz resolution over the entire C+L bands (1527 to 1600 nm); corresponding to 450 resolvable spectral features, such high resolution vastly exceeds all previous examples of biphoton shaping (e.g., [72, 74]), representing a crucial technological advancement. Additionally, this pulse shaper includes the capabilities of a wavelength-selective switch, allowing each frequency component to be independently programmed to exit the shaper through one of four different output ports. In this way we can separate the high-frequency signal and low-frequency idler photons and send them to distinct single-photon detectors (Aurea SPD_AT_M2), correlating the detections with an event timer featuring 1-ps bins (PicoQuant HydraHarp 400). We note that while other researchers have examined a wavelength-selective switch for routing of entangled photons [88], never before have such capabilities been combined with high-resolution pulse shaping.

Because the temporal resolution of the photon detectors greatly exceeds the maximum duration of the biphoton wavepacket, the measured coincidence rate R_c after electronic correlation represents the integral of the correlation function $\Gamma^{(2,2)}(\tau)$ over the resolution of the detection system. In particular, the time aperture of our pulse shaper—the temporal window over which the shaped correlations can accurately re-

The results of this chapter have been published in [87].

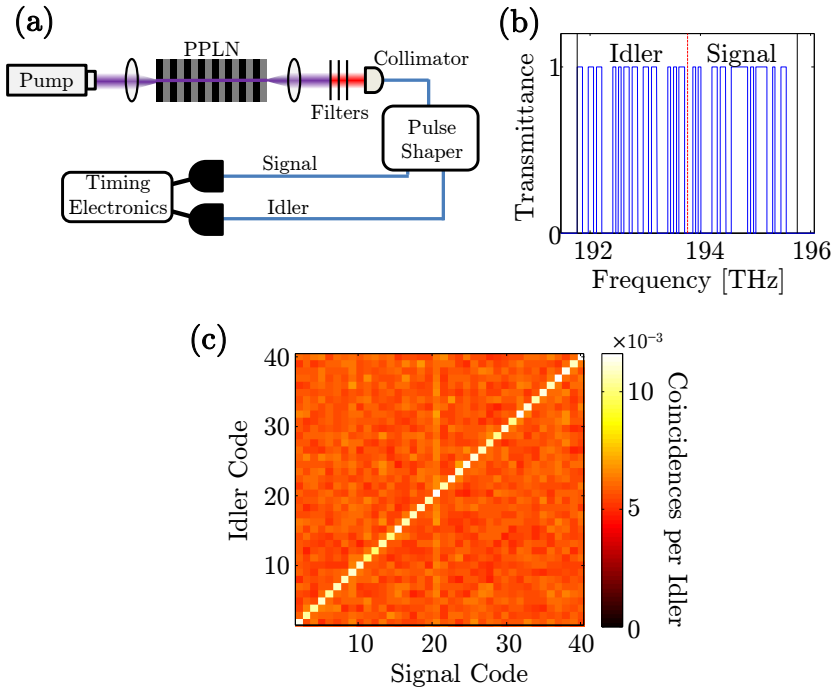

Fig. 5.1. (a) Experimental setup for electronic coincidence experiments. The generated biphotons coupled into optical fiber are filtered by a pulse shaper, with signal and idler photons sent to different output ports and detected on separate single-photon counters. Correlations are determined with time-tagging electronics. (b) Pulse-shaper transmittance for Hadamard codes. Here code 8 is applied to the idler spectrum and code 30 to the signal. (c) Coincidence rate as a function of signal-idler Hadamard codes, normalized to idler detections. Only codes 2 through 40 are shown, as code 1 corresponds to full transmission. When the codes are matched, approximately twice as many coincidences are registered as when the codes differ, confirming spectral entanglement.

produce that of an ideal, infinite-resolution mask [1]—is approximately 50 ps, whereas the detector resolution T_d exceeds 300 ps (experimentally, we take a window of 1 ns to mark simultaneous arrivals on both detectors). Under these conditions, the coincidence rate R_c can be expressed as

$$R_c \propto \int_{-T_d/2}^{T_d/2} d\tau \, \Gamma^{(2,2)}(\tau). \tag{5.1}$$

Since T_d vastly exceeds the maximum possible correlation time of $\Gamma^{(2,2)}(\tau)$, the limits can be extended to $\pm\infty$, which when combined with Eq. (4.31) gives the simple result [88]

$$R_c \propto \int_0^\infty d\Omega |\phi(\Omega) H_s(\omega_0 + \Omega) H_i(\omega_0 - \Omega)|^2, \tag{5.2}$$

which in words states that the coincidence rate is the integral over all possible entangled frequency pairs, weighted by the probability that both photons reach their detectors. Importantly, all dependence on spectral phase has been removed, implying that only amplitude shaping will have an effect on the coincidence rate in these experiments.

5.2 Hadamard Coding for Entanglement Verification

To demonstrate the utility of our biphoton pulse shaper, we first examine a Hadamard amplitude coding approach to markedly increase the count rate in spectral correlation measurements. As highlighted in Fig. 4.1(b), narrowband-pumped SPDC produces a two-dimensional biphoton spectral distribution that shows sharp anticorrelation in joint frequency. And the most straightforward method for measuring these correlations is to simply record the coincidence rate for two narrow spectral filters applied to the signal and idler; doing so for all possible center frequency combinations produces the full joint distribution [89, 90]. Yet this approach suffers from an inverse relationship between resolution and count rate, for to make the resolution finer, the slit passbands must be decreased, which proportionally lowers the overall transmissivity for matched bins. Accordingly, it is difficult and time consuming to measure spectral correlations in this way, particularly for infrared biphotons detected by InGaAs photon counters that suffer from high dark counts compared to their silicon counterparts.

In order to decouple resolution and photon flux, we develop a new spectral filtering approach modeled after classical Hadamard spectroscopy [91]. Instead of measuring the coincidences between spectral *slits*, we look at the coincidences between spectral

codes, chosen from the same Walsh-Hadamard set. In their basic form, these code families contain N length-N sequences of ones and minus-ones that are orthogonal to each other: the inner product of any two different codes is zero [92]. Moreover, with the exception of one code consisting of all ones, each sequence contains an equal number of ones and minus-ones. However, as shown in Eq. (5.2), our detection scheme is insensitive to spectral phase, making such phase-only Hadamard codes indistinguishable; therefore we replace the minus-ones by zeros to instead examine pure amplitude codes of ones and zeros. True orthogonality is then replaced by a contrast of 2:1 between matched and mismatched sequences. Experimentally, we exploit these properties by applying one code to the signal spectrum and another to the idler. If the photons are entangled about the center frequency and the codes match in the symmetric sense, the idler frequency bins corresponding to the passed signal bins are also passed, giving a large number of coincidences. But if the codes do not match, only half of the transmitted signal frequencies are accompanied by the corresponding idler, dropping the coincidence rate by a factor of two. (In this discussion, we neglect the instances when one of the two codes is the all-one case.) In this way, the degree of entanglement can be inferred from the experimentally measured contrast relative to the ideal of 2:1. The key improvement over the traditional two-slit technique lies in the count rate for matched codes. If we divide signal and idler each into N frequency bins, thereby fixing the spectral resolution, a matched bin pair contains only $1/N$th of the total biphoton flux, whereas matched Hadamard codes pass $1/2$ of the flux, independent of the value of N. Thus a count rate improvement of $N/2$ is achieved with our Hadamard approach, and—at least until reaching the limits of the pulse shaper—it is possible to make the spectral resolution finer without suffering an appreciable reduction in peak counts, thereby removing the inverse relationship imposed by the two-slit procedure.

To examine the usefulness of the new method, we program length-40 Hadamard codes with 50-GHz chips, giving total passbands of 2 THz each for the signal and idler photons. As evident in Fig. 4.2(b), over this 4-THz band the biphoton spectrum is

essentially flat, which ensures that all frequency pairs contribute with approximately equal weight, thereby maximizing contrast. An example code combination is presented in Fig. 5.1(b); with 80 resolvable spectral elements, the complexity vastly exceeds all previous experiments in biphoton pulse shaping. Operating the detectors at 20% quantum efficiency and with a 10-ns gate clocked at 1.25 MHz, we attenuate the pump laser to give single-detector count rates of about 3500 s^{-1} when the all-ones code is applied over the passband; this ensures that less than one pair is generated during each coincidence window, minimizing accidentals due to multi-pair emission. Figure 5.1(c) shows the two-dimensional coincidence map obtained by testing all signal-idler code combinations, with a 30-s integration time per point. The contrast between matched and mismatched codes is 1.89:1, slightly less than the theoretical maximum of 2:1 for no accidentals and perfectly flat spectra. The only major drawback is the approximately 6-dB pulse-shaper insertion loss, which proves the main contributor to the relatively low rate of coincidences per idler detection. Nevertheless, our experiment is able to verify spectral entanglement clearly and with a 20-fold increase in total counts over the equivalent pair of monochromators. Admittedly, with the ability to raise the biphoton flux by a factor of $N/2$, it would be possible to achieve the same coincidence rate for matched monochromators as in our Hadamard approach. However, in addition to the requirement of adjusting the pump power, which may be impractical in some circumstances, doing so also increases the relative probability for accidentals due to multiple-pair generation, which scales quadratically with the pair flux [93]. In contrast, our method boosts the coincidence rate at any given pump power, significantly improving sensitivity without altering the statistical properties of the input field. Hadamard coding can thereby be viewed as a source-independent method to verify spectral entanglement much more efficiently than comparing the coincidences between two narrowband filters.

5.3 Interferometer Emulation

Our high-resolution pulse shaper shows additional promise in experiments in Franson interferometry. The archetypal Franson interferometer [94] is shown in Fig. 5.2(a); signal and idler photons are sent through separate Mach-Zehnder interferometers (MZIs), identical except for phase shifts in their long arms, and coincidences between two of the output ports are measured. If the difference between long and short arms exceeds the single-photon coherence time (on the order of picoseconds or less for our biphotons) but is less than the coherence time of the pump (longer than a microsecond for our source), the coincidence rate displays interference while the single-photon rate is constant [94]. Explicitly, the coincidence rate is of the form

$$R_c \propto 1 + \mathcal{V}\cos(\Phi_s + \Phi_i + 2\omega_0 T), \tag{5.3}$$

where Φ_s and Φ_i are the signal and idler phase shifts, $2\omega_0$ the pump frequency, and T the relative long-arm delay; the visibility $\mathcal{V}$ is a number between 0 and 1. Intuitively, such interference results from the intrinsic indistinguishability of coincidences resulting from either both photons taking the long arms (long-long) or both taking the short (short-short); since it is impossible—even in principle—to tell these apart, the two probability amplitudes interfere [95]. If the MZI path-length difference exceeds the detector resolution, then the cases when the photons traverse different arms (long-short and short-long) can be thrown out, permitting a visibility $\mathcal{V} = 1$. On the other hand, if the detectors cannot tell that one photon arrived a time T after the other, a background contribution remains, restricting $\mathcal{V}$ to at most 1/2 [96]. This situation furnishes an excellent example of the importance in quantum optics of indistinguishability *in principle* [95]. Even though slow detectors cannot tell the difference between simultaneous and delayed arrivals, because it is in principle possible to distinguish them with improved equipment, the short-long and long-short paths produce no interference. This and its other interesting properties have made the Franson interferometer a ubiquitous tool in QKD protocols and in entanglement ver-

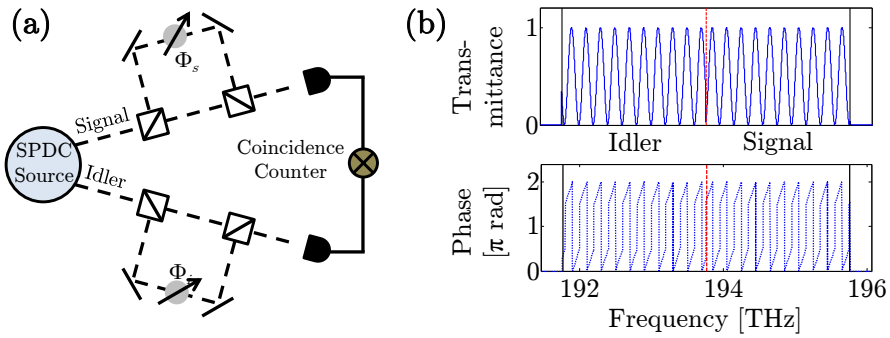

Fig. 5.2. (a) Typical Franson interferometer. The signal and idler photons are sent through MZIs with different phase shifts in the long arms: Φ_s for the signal and Φ_i for idler. (b) Spectral transmittance and phase applied by pulse shaper to emulate a Franson interferometer. Signal and idler photons are distinguished by frequency and sent through spectral filters that are equivalent to traversing MZIs. In addition to 2π jumps from wrapping the spectral phase, π discontinuities also occur as the sinusoidal field transmission function—the square of which gives the power transmittance—changes sign.

ification in general (e.g., [60,61,65,67,86,97,98]), and here we explore novel methods to implement such an interferometer with our pulse shaper.

Since the field at one MZI output is related to the input through a linear and time-invariant transformation, each MZI can be expressed as an equivalent complex spectral filter, which in turn can be programmed directly on the pulse shaper [74]. Neglecting an unimportant overall delay, the signal MZI has the transmittance

$$|H_s(\omega)|^2 = \cos^2\left(\frac{\Phi_s + \omega T}{2}\right) \tag{5.4}$$

and phase

$$\arg H_s(\omega) = \begin{cases} (\Phi_s + \omega T)/2 & \text{if } \cos\left(\frac{\Phi_s+\omega T}{2}\right) > 0 \\ (\Phi_s + \omega T)/2 + \pi & \text{if } \cos\left(\frac{\Phi_s+\omega T}{2}\right) < 0. \end{cases} \tag{5.5}$$

(The idler filter is obtained by replacing Φ_s with Φ_i in the above.) An example filter function for $\Phi_s = \pi/2$, $\Phi_i = 0$, and $T = 5$ ps is given in Fig. 5.2(b). In replacing the mirrors and beam splitters of a traditional MZI with a stand-alone pulse shaper,

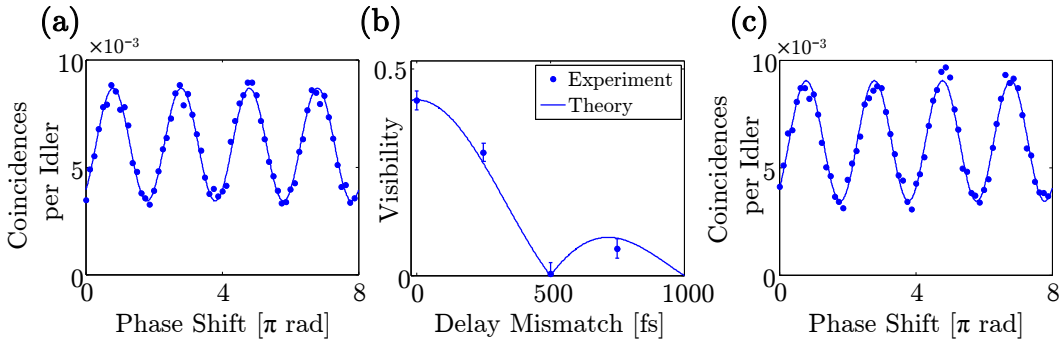

Fig. 5.3. (a) Experimental coincidence rate for pulse-shaper Franson interferometer, at matched MZI delays and with a 30-s integration time per point. The detected coincidences show interference with the applied phase $\Phi_s + \Phi_i$, possessing a visibility of 0.43. (b) Reduction in visibility as the MZI delays are shifted from each other. The theoretical curve is scaled to match the experimental visibility at zero mismatch, and error bars represent 95% confidence intervals for the fit parameters. (c) Coincidence rate for pulse-shaper interferometer with flat spectral phase, again at a measurement time of 30-s per data point. The visibility is 0.45.

our implementation offers enhanced stability over the standard Franson arrangement. Unlike mounted mirrors which destroy interference at the slightest mechanical perturbation, this pulse shaper provides a constant spectral filter independent of table vibrations or temperature fluctuations.

Programming $T = 5$ ps for both spectral filters and measuring the coincidence rate as the phase is shifted, we find the results of Fig. 5.3(a), least-squares fit to a sinusoid and without dark count subtraction. As expected, the measured visibility of 0.43 is below the theoretical maximum of 0.5 for our slow detectors ($T_d \gg T$). This pulse shaper therefore fully emulates the standard Franson interferometer. Moreover, its programmability allows us to easily examine more subtle interference effects, such as signal-idler path-length mismatch. As the long path of the signal MZI is changed compared to that of the idler MZI, an element of distinguishability is introduced between the long-long and short-short coincidence paths, for no longer is the signal-idler arrival difference identical, and so the visibility is expected to decrease. This

argument is confirmed in theory: for a flat signal spectrum of width $\Delta\omega$ and a signal-idler long-arm mismatch of ΔT, we can utilize Eq. (5.2) to obtain

$$R_c \propto 1 + \mathcal{V}\text{sinc}\left(\frac{\Delta\omega\Delta T}{2}\right)\cos(\Phi_s + \Phi_i + \varphi), \tag{5.6}$$

where φ is a constant phase offset. Therefore we expect the visibility to decrease like a sinc function. Figure 5.3(b) shows the measured interference visibility as a function of delay mismatch, which indeed matches that expected for our 2-THz signal spectrum.

The pulse shaper also permits the creation of "interferometers" with no mechanical analogues, an example of which was examined previously in the phase-sensitive ultrafast detection regime [74]; here we extend these concepts to the slow-detector limit. Recalling the findings encapsulated in Eq. (5.2), we expect our measured interference pattern to show no dependence on the phase of $H_s(\omega)$ or $H_i(\omega)$. And with our pulse shaper, it is simple to program the spectral transmittance along with flat phase instead of Eq. (5.5)—a condition which would be impossible to achieve with a mechanical MZI. So taking the spectral amplitude of Eq. (5.4) with flat phase, and sweeping the phase shift $\Phi_s + \Phi_i$, we obtain the interferogram in Fig. 5.3(c); with a visibility of 0.45, it is nearly identical to that found when the shaper was programmed with the full MZI phase. Thus we are able to confirm spectral phase independence in the slow-detection regime, enabled by the independent phase and amplitude control of our pulse shaper.

5.4 Conclusion

Using basic single-photon detection, we have experimentally verified a simple, fiber-pigtailed pulse-shaping system for the control of entangled photons in the telecom band, which offers integrability with existing fiber-based quantum systems. We have demonstrated its effectiveness specifically in a new Hadamard-based approach for gauging spectral entanglement and in creating modified Franson interferometers. More generally, this setup's versatility and programmability make it a useful tool for future characterization of biphoton sources in QKD systems.

6. EXPERIMENTS WITH ULTRAFAST COINCIDENCE DETECTION

6.1 High-Efficiency Biphoton Correlator

The experiments described in Chapter 5 have shown how high-resolution pulse shaping can be exploited to manipulate telecom biphotons. However, with the slow electronic detectors employed, one is fundamentally limited by Eq. (5.2), in that only amplitude filtering has an effect on the measured coincidence rate; any spectral phase modulation vanishes. Therefore we would desire an alternative detection scheme with timing resolution sufficient to measure the correlation function directly, for which the full potential—and fascinating physics—of phase shaping can be realized. Fortunately for us, such a method has indeed been demonstrated, based on biphoton sum-frequency generation (SFG) [100]. Instead of sending signal and idler photons to separate detectors, they are mixed in a second nonlinear medium; if the photons overlap in time, with some small probability they can recombine through SFG and generate a new photon at the original pump frequency. As shown theoretically in [101] and discussed in detail in Appendix B, when phase matching permits all frequency pairs to combine with equal weight, the rate of SFG is directly proportional to the correlation function $\Gamma^{(2,2)}(\tau)$, where the time separation τ can be controlled by stepping the delay of one photon with respect to the other. Such fine resolution is made possible by use of an ultrafast optical—rather than electronic—coincidence gate maintaining femtosecond-level timing resolution, analogous to the nonlinear techniques widely employed for characterizing ultrashort classical pulses [1]. The major shortcoming of this method, though, is the typically low efficiency of biphoton SFG;

The results in Sections 6.1 and 6.2 have been published in [99].

at such low light levels, efficiencies of only 10^{-9} [74] or 10^{-7} [100] have been reported, limiting the applicability of this approach in high-loss environments.

To significantly improve this efficiency, we have proposed and implemented a new biphoton correlator based on SFG in a PPLN waveguide, whose large nonlinear coefficient and long interaction length offer huge performance gains over the bulk crystals employed previously. Figure 6.1(a) shows the setup for our ultrafast coincidence experiments. After the biphotons are coupled into optical fiber, they are either sent through DCF or a pulse shaper and then focused into a second PPLN waveguide, ideally identical to the first and heated to achieve phase matching with it. The unconverted biphotons are removed by three colored glass filters (Schott RG9) and the SFG photons detected by a silicon single-photon avalanche photodiode (PicoQuant τ-SPAD) with a dark count rate less than 20 s^{-1}; an electronic counter (SRS SR400) then logs the detections over specified time windows. No dedicated delay stage is present, since we can control relative signal-idler delay by programming linear phase on the pulse shaper [72]. To minimize loss, we first insert the DCF link with a dispersion of -78 fs/nm, which we have found optimally compensates the combined dispersion of the nonlinear crystals and the $\sim$5 m of Corning SMF-28e fiber connecting the two PPLN waveguides. It is important to verify that we are indeed operating in the single-pair regime (no more than one biphoton within the correlation time). Not only is this required to see the desired quantum correlations, but unacceptably high photon fluxes will also taint any efficiency measurements, due to unwanted mixing of photons from separate entangled pairs. Verification is possible by recording the SFG counts as the pump is attenuated, for in the multi-pair regime the count rate is expected to scale quadratically, whereas a linear dependence obtains for quantum light [100, 101].

Figure 6.1(b) furnishes the results of this test. Each data point represents the average of five 1-s measurements, and the subtracted dark count rate is determined by recording the counts over 5 s when the pump is blocked. A log-log slope of 1.13 is found for the curve, confirming that we reside in the near-linear, quantum regime.

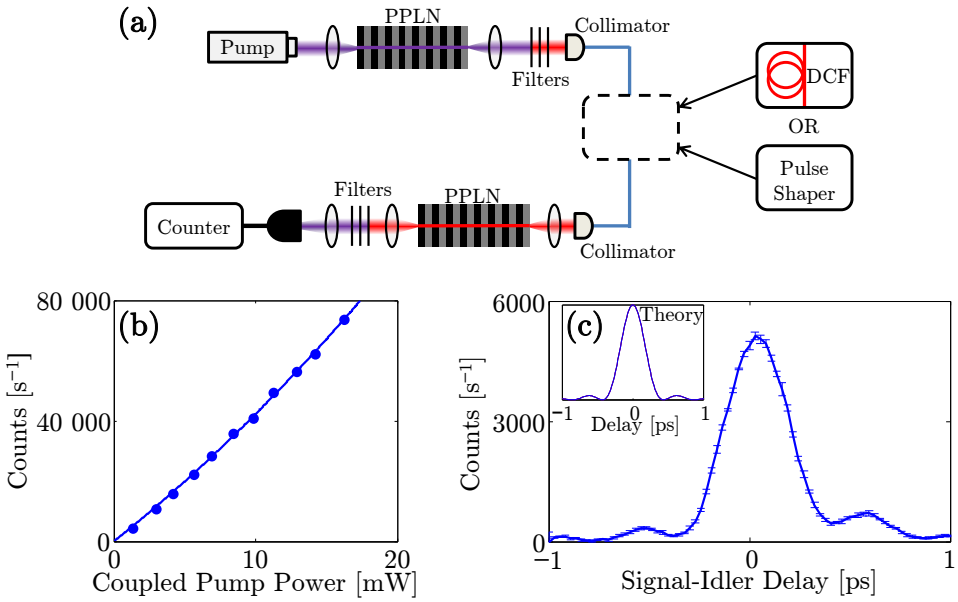

Fig. 6.1. (a) Experimental setup for ultrafast coincidence detection. The biphotons are manipulated with either DCF or a pulse shaper and coupled into a second waveguide for upconversion. A single-photon counter detects the number of SFG photons at ∼774 nm. The second collimator as well as the detector are housed in a box to exclude stray light. (b) Measured detector counts as a function of power coupled into the first waveguide, when DCF is used. The log-log slope is 1.13. (c) Measured signal-idler temporal correlation function with linear interpolants between data points; here the pulse shaper is used to achieve zero net dispersion. The theoretical result is given in the inset.

The raw count rate is exceptionally high as well, reaching 74 100 s^{-1} at a coupled pump power of 16.3 mW. Accounting for losses between the two PPLN waveguides, the probability for a coupled photon pair to recombine in the second waveguide is found to be approximately 10^{-5}, comparable to our SPDC conversion efficiency, as expected from theory (cf. Appendix B), and a full two orders of magnitude higher than the best previously reported [100]. Most importantly, our record-efficiency correlator facilitates use of another high-resolution commercial pulse shaper, whose loss would have otherwise disqualified it with less efficient bulk crystals. In these experiments, we utilize a slightly different Finisar WaveShaper (model 1000S) from that in the previous

chapter; since signal and idler need not be physically separated for detection, we are free to enlist a pulse shaper with only one output port, so we have chosen a model with 10-GHz resolution over the C-band from 191.250 to 196.275 THz. Losing the L-band capabilities of the 4000S/X is of no consequence for us; the SPDC emission's center frequency is located on the high-frequency half of the C-band, so even if we could pass more idler photons by including the L-band, the corresponding signals—and thus the biphotons as a whole—would still be blocked. The pulse-shaper insertion loss is approximately 5 dB, and since we use SFG for detection, which scales quadratically with shared signal-idler optical loss [100, 101], we thereby incur a ∼10-dB reduction in counts, which is nonetheless tolerable because of our exceedingly high count rate.

Operating at the maximum power in Fig. 6.1(b), we replace the DCF with the pulse shaper, programming on it a baseline quadratic phase to achieve a net dispersion of zero and maximize SFG counts. Following the same procedure as in [72], the signal-idler correlation function is then obtained by sweeping through additional oppositely sloped linear phase terms applied to the signal and idler spectra and measuring the SFG counts at each step; the net signal-idler delay is proportional to the difference in these two slopes, thereby permitting tunable control of the relative photon timing. We note that, in general, SFG introduces distortions in the obtained correlation function due to phase-matching nonuniformity [102, 103]. However, our use of a pulse shaper restricts the SPDC bandwidth to within the nearly flat portion of the phase-matching response, ensuring that all frequency pairs combine freely. This produces an SFG flux directly proportional to $\Gamma^{(2,2)}(\tau)$, as detailed in Appendix B.

The result of our measurement is given in Fig. 6.1(c). Error bars depict the uncertainty in five 1-s measurements, after dark count subtraction. In this instance, we obtain the dark count rate by recording the counts when the pulse shaper is programmed to maximum (> 35 dB) attenuation. (This method is employed in all subsequent measurements in this chapter.) Even though the second waveguide and detector are isolated from ambient light by an enclosure, dark counts around 450 s^{-1} are found because of a monitoring light-emitting diode inside the shaper. The

temporal FWHM of the correlation function is 370 fs, in good agreement with the 354 fs expected for a bandlimited flattop signal half-spectrum cut down to 2.5 THz by the pulse shaper. Simulations suggest the slight asymmetry could be due to a small spectral mismatch between the phase-matching curves of the two crystals, although we have not been able to pursue this hypothesis in detail experimentally.

Building on the technical accomplishment of our record-efficiency correlator, we are thus left with an operational "biphoton playground" in which we are free to explore a wide range of complex spectral shaping techniques. Accordingly, our focus in the next four sections is to extend pulse-shaping ideas developed in classical optics to entangled photons, exploring new phenomena of both fundamental and potentially practical interest. Specifically, we exploit high-order dispersion control, common in ultrashort pulse generation, to demonstrate high-order biphoton dispersion cancellation; orthogonal phase codes, used in classical optical code-division multiple-access (O-CDMA) communications, to encode and decode entangled photons; patterned amplitude or phase filtering, used to generate high-repetition-rate classical pulse trains, to create periodic biphotons and show the temporal Talbot effect; and frequency tuning, used for delay control in classical systems, to modulate the relative arrival times of entangled photon pairs.

6.2 High-Order Dispersion Cancellation

Methods to control and compensate optical dispersion—the variation of group velocity with optical frequency [1]—have proven essential in applications ranging from the generation of ultrashort pulses to optical communications. Such concerns naturally extend into the quantum regime as well, e.g., in the spreading of biphoton correlations [104] or heralded single-photon wave packets [105]. Yet the spectral correlation between entangled photons actually permits a fascinating *nonlocal* cancellation of this dispersion; as first shown theoretically by Franson [106], propagating each photon of an entangled pair through different media with equal and opposite

second-order dispersion has no effect on the correlation function, even if the two are arbitrarily far apart; although individually each photon spreads, the dispersion of one photon cancels that of the other so that collectively the biphoton remains unaltered. The mathematical origin of this effect for our biphoton source is readily observed by specializing Eq. (4.31) to pure phase filters $H_s(\omega) = \exp[i\Phi_s(\omega)]$ and $H_i(\omega) = \exp[i\Phi_i(\omega)]$, where $\Phi_s(\omega)$ and $\Phi_i(\omega)$ are arbitrary real functions of frequency. The biphoton wavepacket then becomes

$$\psi(\tau) = \int_0^\infty d\Omega\, \phi(\Omega) \exp\Big\{ -i\Omega\tau + i[\Phi_s(\omega_0+\Omega) + \Phi_i(\omega_0-\Omega)]\Big\}. \tag{6.1}$$

Thus whenever $\Phi_s(\omega_0+\Omega) = -\Phi_i(\omega_0-\Omega)$, the original wavepacket is recovered, with the signal dispersion canceling that of the idler. In ultrafast optics, it is common to describe such spectral phase modulation in terms of the contributing orders of its Taylor expansion; writing signal-idler phases as $\Phi_{s,i}(\omega) = \sum_n \Phi_{s,i}^{(n)}(\omega-\omega_0)^n/n!$, the wavepacket assumes the form

$$\psi(\tau) = \int_0^\infty d\Omega\, \phi(\Omega) \exp\left\{ -i\Omega\tau + i\sum_{n=0}^{\infty} \left[\Phi_s^{(n)} + (-1)^n \Phi_i^{(n)}\right] \Omega^n \right\}. \tag{6.2}$$

Perfect dispersion cancellation, to all orders, is thereby obtained by the condition $\Phi_s^{(n)} + (-1)^n\Phi_i^{(n)} = 0$ for $n = 2, 3, 4, ...$ (The $n = 0, 1$ cases have no impact on the biphoton shape itself.) Dispersion cancellation has been shown on the ultrafast timescale, but only for second-order spectral phase [103]. On the other hand, higher orders become increasingly important for wide bandwidths, and so it is essential to generalize dispersion cancellation to arbitrary dispersions. Although experimental examination of such effects is difficult with standard optical materials and components, due to the lack of independent control of each order, it is attainable with programmable Fourier-transform pulse shaping. We are therefore able to examine high-order dispersion cancellation for the first time using our high-efficiency correlator and fine-resolution pulse shaper.

Before proceeding to the experiments themselves, it is interesting to note that the opposite sign of dispersion yields cancellation for even orders only; for odd orders, the

same sign is required. The spectral anticorrelation of the entangled photons requires that the signal and idler phases be antisymmetric with respect to each other. Thus odd-order coefficients must be matched, not flipped, for full cancellation. This condition is analogous to classical narrowband SFG, which is sensitive only to the symmetric phase [107]. And this reveals a principal difference between Franson cancellation and dispersion insensitivity in Hong-Ou-Mandel (HOM) interference [108–111]. HOM dispersion cancellation places symmetry constraints only on the total biphoton phase, not on the particular functional forms of the signal and idler phases relative to each other. If we define $\Phi_T(\Omega) = \Phi_s(\omega_0 + \Omega) + \Phi_i(\omega_0 - \Omega)$, then the HOM interference pattern is unaffected so long as $\Phi_T(-\Omega) = \Phi_T(\Omega)$; i.e., the total biphoton phase must be a symmetric function of the signal frequency offset. Thus, the HOM interferometer is intrinsically insensitive to any even-order phase experienced by either photon [111], a property that has permitted narrow HOM dips even without true Franson cancellation [110, 112]. On the other hand, the dispersion cancellation examined here, which applies to the biphoton correlation function directly, demands the more stringent condition that the total biphoton phase be identically zero, for all orders above first.

Utilizing the setup of Fig. 6.1(a) with the pulse shaper applying the same baseline quadratic phase used to achieve the bandlimited correlation function in Fig. 6.1(c), we add additional phase terms to examine the cancellation of high spectral orders, from $n = 2$ to $n = 5$. The particular phase coefficients are chosen to yield dispersed waveforms in the range of ± 5 ps, which is well within the ± 30-ps maximum delay possible with the pulse shaper. The basic procedure for each order n is first to apply the specified dispersion $\Phi_s^{(n)}$ to the signal photon, with no dispersion on the idler; then filter the idler with either identical or opposite dispersion $\Phi_i^{(n)}$, but leave the signal untouched; and finally, apply the previous spectral phases to both photons simultaneously. In the first two cases, a broad and lowered correlation function should be observed, while in the third, the original narrow peak should be recovered.

And this is precisely what is obtained in experiment. The second-order case is presented in Fig. 6.2(a) (theory) and (b) (experiment), for dispersion constants

$\Phi_s^{(2)} = -\Phi_i^{(2)} = -0.3$ ps^2. With $\Phi_s^{(2)}$ applied to the signal, but nothing to the idler, a broadened correlation function is obtained; similar behavior is seen with nothing applied to the signal, but $\Phi_i^{(2)}$ on the idler. However, simultaneously applying both spectral phases returns the correlation function to its original, undispersed form, demonstrating complete cancellation. Proceeding to the next even order, with $\Phi_s^{(4)} = -\Phi_i^{(4)} = -0.01$ ps^4, we find the results of Figs. 6.2(c) and (d). Just as in the second-order case, fourth-order cancellation is obtained by applying the opposite sign of $\Phi_s^{(4)}$ to the idler, matching expected results from theory. Odd-order spectral phase follows the reverse procedure, for the signal and idler expansion coefficients must be equal for cancellation to ensue. We verify this behavior for the third-order case in Figs. 6.3(a) and (b). Taking $\Phi_s^{(3)} = \Phi_i^{(3)} = -0.05$ ps^3, cancellation is indeed observed when the same third-order phase is applied to both signal and idler, even though broadening occurs in the individual cases. Finally, testing fifth-order phase with dispersion constants $\Phi_s^{(5)} = \Phi_i^{(5)} = -0.01$ ps^5, cancellation is again achieved, as shown in Fig. 6.3(c) and (d).

The fact that even and odd orders carry opposite requirements highlights a crucial divergence from related dispersion effects with coherent or thermal optical sources. For example, in local dispersion compensation of classical pulses, all spectral orders in the compensating medium must be flipped relative to the dispersing medium. On the other hand, for dispersion cancellation with thermal light sources, the dispersion along both paths must be identical [113–115]. In either case, all spectral orders share a fixed cancellation condition, independent of parity, quite different from the alternating behavior shown here. Experimental observation of these effects represents a key contribution of our work, improving overall understanding of biphoton dispersion management. In particular, we believe our pulse-shaping approach to high-order dispersion cancellation could prove quite useful in the quest for single-cycle biphotons—ultrabroadband entangled photons with correlation times of only a few femtoseconds [116]. Although extremely narrow HOM dips have been observed [112], a single-cycle correlation function has yet to be demonstrated, due in large part to

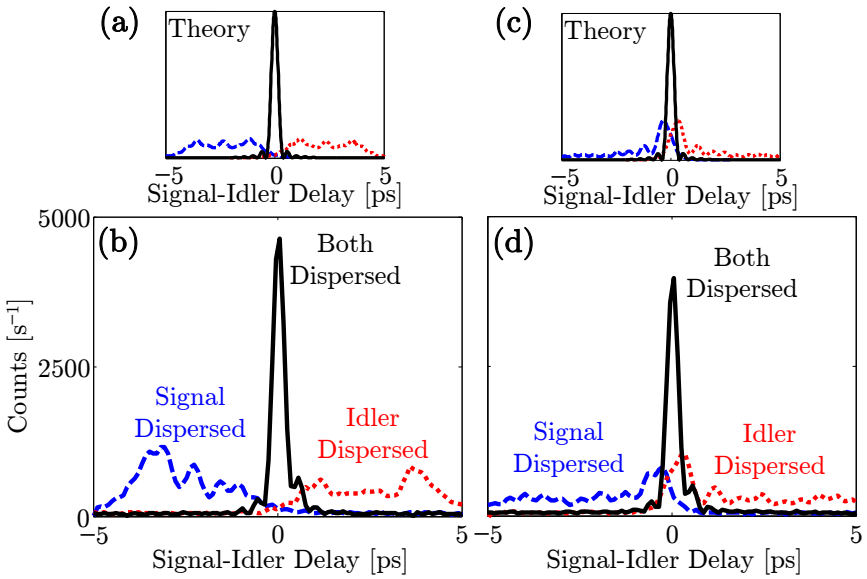

Fig. 6.2. Even-order dispersion cancellation. (a) Theoretical and (b) experimental results for second-order cancellation, using $\Phi_s^{(2)} = -\Phi_i^{(2)} = -0.3$ ps^2. Likewise, (c) theory and (d) experiment for fourth-order cancellation with $\Phi_s^{(4)} = -\Phi_i^{(4)} = -0.01$ ps^4. Error bars are omitted for clarity, but are comparable to those in Fig. 6.1(c), and each curve consists of 100 points, spaced at 100 fs each and joined by linear interpolation. "Signal dispersed" and "idler dispersed" signify application of the specified phase to only one of the two photons, whereas "both dispersed" represents application to both.

a lack of high-order dispersion control [117]. Our experiments generalizing Franson cancellation to arbitrary spectral orders therefore represent an important step in this direction.

6.3 Orthogonal Spectral Coding

In the Hadamard coding described in Section 5.2, we were limited to amplitude-only spectral codes since the slow electronic detectors could not observe any phase effects. However, with our ultrafast biphoton correlator, spectral phase modulation

The results in Section 6.3 have been published in [118].

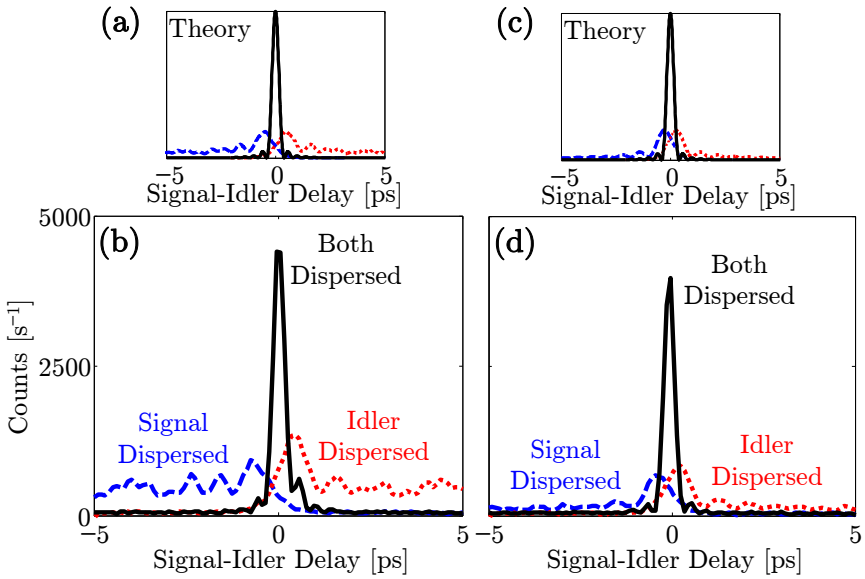

Fig. 6.3. Odd-order dispersion cancellation. Cancellation of third-order dispersion in (a) theory and (b) experiment, for the specific case of $\Phi_s^{(3)} = -\Phi_i^{(3)} = -0.05$ ps^3. (c) Theoretical and (d) experimental cancellation of fifth-order dispersion, for $\Phi_s^{(5)} = -\Phi_i^{(5)} = -0.01$ ps^5. The same considerations mentioned for Fig. 6.2 hold here as well.

is instead of critical importance, as clearly evidenced by the dispersion cancellation experiments in the previous section. Therefore we now examine the possibilities available from truly orthogonal Hadamard codes consisting of ones and minus-ones (phases of 0 and π). Such codes have been utilized in classical O-CDMA [119, 120], and we make use of the concept of time-reversed entanglement generation [121–123] to connect this classical approach to entangled photons. The basic idea is that, instead of using SPDC of a narrowband pump to generate broadband entangled photons, some entanglement-like effects can be seen by considering SFG of broadband classical fields at a fixed upconversion frequency. This process effectively post-selects only the spectral combinations of the classical field that are correlated in the same manner as entangled photons, permitting, for example, a classical analogue of the dispersion cancellation discussed in the last section [123]. Here, though, instead of using this

connection to obtain a classical version of a quantum phenomenon, we exploit it to go in the opposite direction, taking classical code-based O-CDMA to entangled photons.

The classical foundation has been demonstrated in the spectral coding of coherent optical pulses, in which one Hadamard phase code is applied to the upper half of the spectrum ($\omega > \omega_0$), and a second one to the lower half ($\omega < \omega_0$); then a narrowband SFG field is generated and measured [107, 124]. If phase matching permits all constituent frequencies to combine, the resultant SFG field at frequency $2\omega_0$, $\tilde{E}_{\mathrm{SFG}}(2\omega_0)$, is given by the integral [1]

$$\tilde{E}_{\mathrm{SFG}}(2\omega_0) \propto \int_0^\infty d\Omega\, \tilde{E}(\omega_0 + \Omega)\tilde{E}(\omega_0 - \Omega). \tag{6.3}$$

For an input field with a flat spectral amplitude, the integral can be viewed as the inner product between the codes applied to each half of the spectrum. If they are identical (i.e., a mirror image about ω_0), a high yield is found, but if they differ, orthogonality ensures that the integral drops to zero. This discrimination provides a means for many users to communicate over the same spectro-temporal space. The sender encodes the message by applying the intended receiver's code to one spectral half, and only the receiver who applies the correct code to the opposite half will see the message above the background.

Comparing Eq. (6.3) with the general shaped biphoton wavepacket of Eq. (4.31) reveals immediately how one can obtain an entangled photon version of this coding. If $\phi(\Omega)$ is flat over the filter passbands, and we apply Hadamard codes to both the signal and idler, the biphoton wavepacket at $\tau = 0$ is mathematically equivalent to the classical SFG field in O-CDMA: matched codes give a peak, whereas mismatched codes yield essentially zero. How such coding on entangled photons would work is summarized in Fig. 6.4. The signal half of the spectrum corresponding to a temporally narrow biphoton is initially encoded with a Hadamard sequence of 0 and π phases, which spreads and lowers the temporal correlation function, creating a null at zero delay. Then a second phase code is applied to the idler. If the codes match in the symmetric sense, the sharply peaked biphoton is recovered, with a temporal shape identical to the uncoded biphoton in the ideal case. But if the codes

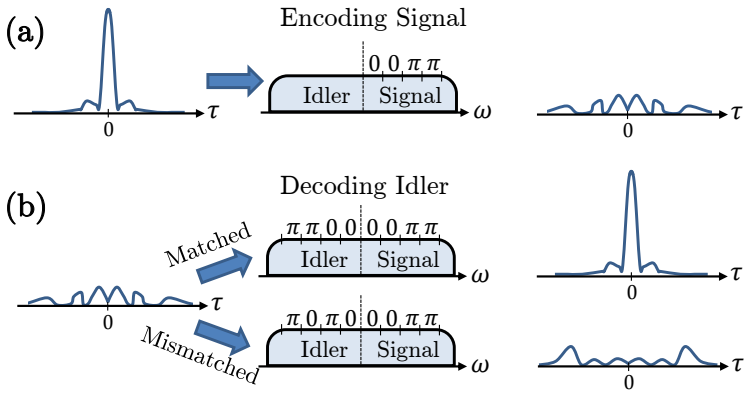

Fig. 6.4. Principle of biphoton spectral coding. (a) Encoding the biphoton. A sequence of 0 and π phase shifts is applied to the signal half-spectrum of a temporally narrow biphoton, which spreads the correlation function in time and produces a null at $\tau = 0$. (b) Decoding the biphoton. A second code is applied to the idler half of the spectrum. If it matches that used for encoding, the narrow correlation peak is recovered, while an unmatched code instead leaves the correlation function in a new, but still spread, state.

differ, the correlation function remains spread with zero magnitude at $\tau = 0$. We remark that this configuration can be viewed as the spectral dual to the temporal coding demonstrated in [125], which is itself an excellent example of carrying classical communication techniques over to biphotons.

For a more intuitive understanding of our approach, we can view this encoding and decoding phenomenon as an example of the quantum mechanical interference of indistinguishable paths. Unlike classical probabilities, the complex amplitudes associated with quantum paths interfere with each other if they cannot be distinguished, even in principle [95], a concept which we utilized to justify the interference in the Franson interferometer of Section 5.3. But whereas two indistinguishable paths contribute in that interferomenter, in our orthogonal coding case we instead have N indistinguishable bin combinations of frequency pairs, for without additional measurements that destroy the experiment, it is impossible to tell through which Hadamard chips the detected photons passed. Accordingly, the probability amplitudes interfere with

each other, and when mismatched codes give identical numbers of pair offsets with combined phase shifts of 0 and π, we obtain perfect cancellation at zero delay. Thus one can view our orthogonal coding approach as an extension of path interference in which the number of paths is programmably controlled by a pulse shaper.

This flexibility in choosing the dimensionality of the coding process—and indeed the effectiveness of the coding itself—derives from the high degree of entanglement possessed by our biphoton source. In general, bipartite entanglement is quantified by the Schmidt number, which roughly corresponds to the total signal-idler spectral modes contributing to the entanglement [126, 127]. The Schmidt decomposition conveys the information potential of an entangled photon pair, indicating in our scheme the maximum useful code dimensionality and also conceivably limiting the spectral shapes of correlated signal-idler frequency modes. Experimentally, this degree of entanglement is well characterized by the Fedorov parameter [128], or the ratio of the marginal signal bandwidth to that conditioned on a frequency measurement of the idler. For our source, with a total signal bandwidth over 2 THz and a conditional width predicted to be less than 200 kHz (the pump laser linewidth) the estimated Fedorov ratio is in excess of 10 million. Such high-dimensional entanglement fully justifies the monochromatic pump assumption built into Eq. (4.14), and it also indicates that our coding process, which we push to a dimension of 40, is only beginning to access the intrinsic information potential of the biphotons themselves; as we note later, experimental limitations such as pulse-shaper resolution prove far more restrictive.

Moreover, while we do employ an SFG detection scheme in these experiments, just as in the classical version [107,124], our use is fundamentally different. In the classical implementation, the process of narrowband SFG is necessary to achieve the desired spectral gating of the product of the input fields—upconversion evaluates only the waveform corresponding to the Hadamard products. But in our case, SFG is required only inasmuch as it furnishes sufficient timing resolution to observe the fine features of the correlation function. The orthogonality condition is imposed on the biphoton state itself and therefore could be seen nonlocally by isolated detectors possessing

adequate resolution. Thus our use of SFG is not a fundamental, but only technical restriction which could be removed in the future by improvements in single-photon detector jitter to the picosecond level [129].

Using the same setup and baseline quadratic phase as in the dispersion cancellation tests [Fig. 6.1(a) with the pulse shaper in place], we first examine our phase coding approach in measurements of the spectral correlations of entangled photons. Previously, in Section 5.2, we implemented an amplitude coding approach which featured an improved count rate over coincidence measurements between two narrow slits, with a theoretical contrast of 2:1 between matched and mismatched codes. Here, however, utilizing pure phase coding accompanied by ultrafast coincidence detection, the contrast between the coincidences at zero delay for matched and mismatched codes is theoretically unbounded, for the phase codes are truly orthogonal. Additionally, phase Hadamard coding compared with narrow slits in the same ultrafast detection scheme is now expected to show an N^2 enhancement in the measured count rate at matched codes and zero delay, instead of the $N/2$ improvement with amplitude codes. One factor of N results from the increased total flux by passing all bins, and another factor of N occurs because of the increased total bandwidth, which supports a temporal correlation function with a sharper peak. Now while this N^2 increase might seem an upgrade over the $N/2$ enhancement of the amplitude coding approach, we point out that the overall efficiency of ultrafast coincidence detection (10^{-5} in our record correlator) makes any phase coding ill-suited for practical spectral measurements; we simply use this test to characterize performance, in no way billing it as a viable spectral measurement technique.

Taking 2.4-THz passbands for the signal and idler, we split both into 4 chips (600 GHz each), finding that both Hadamard [Fig. 6.5(a)] and double-slit [Fig. 6.5(b)] implementations show clear anticorrelation to this resolution, although the Hadamard approach yields an approximately 16-fold increase in total SFG counts. This improved flux becomes even more evident when the chips are made finer. The results for 300-GHz chips are shown in Figs. 6.5(c) and (d), and while the orthogonal codes still give a

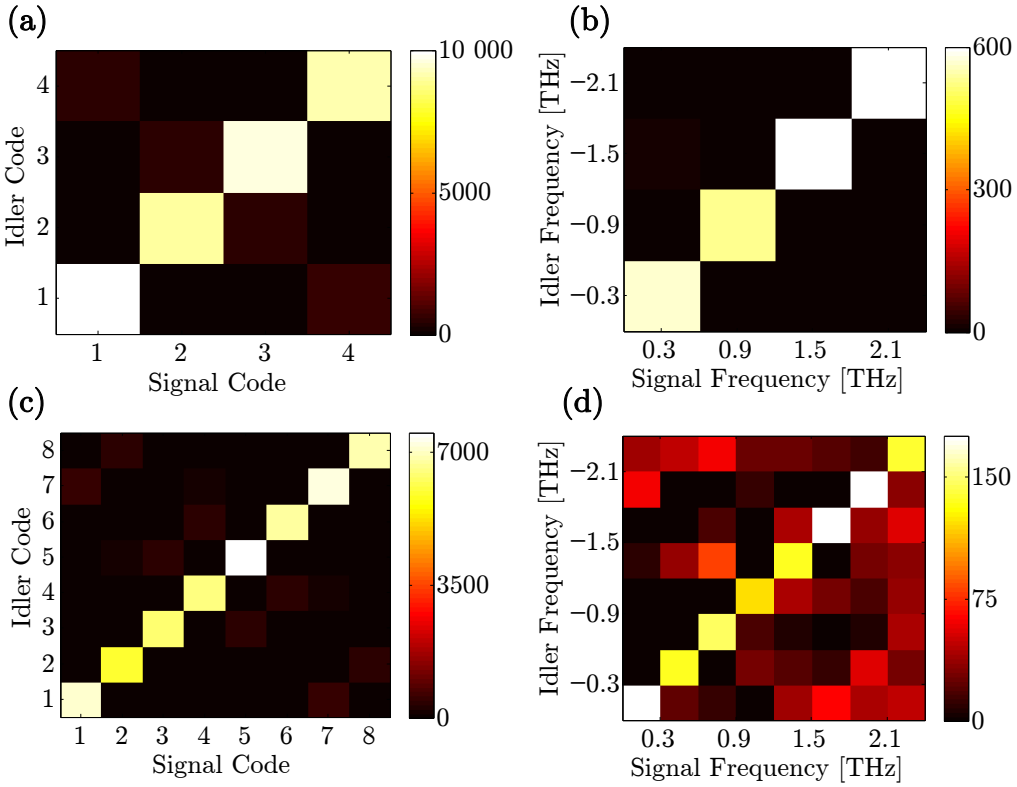

Fig. 6.5. Comparison of Hadamard and equivalent spectrometer measurements. (a) Coincidence rate [s^{-1}] for length-4 Hadamard codes and (b) for the equivalent bandpass filter combinations, with frequencies given by the offset from the degeneracy point, ω_0. (c) Coincidence rate [s^{-1}] for length-8 Hadamard codes and (d) for bandpass filters.

contrast of 59:1 between matched and mismatched cases, the double-slit measurement is beginning to fall into the noise as the maximum count rate drops. Continuing to chop down the frequency bins would push the two-slit case completely into the noise, whereas the Hadamard resolution is far from limited, as we show next.

Pushing the orthogonal codes even further, we split the 2.4-THz bands into 20 chips (120 GHz each), once again recording the coincidences at zero delay for all combinations. As shown in Fig. 6.6(a), a high count rate is still maintained, and matched codes yield on average 115 times more counts than unmatched pairs. Extending this to length-40 codes generates the correlation map in Fig. 6.6(b). In this case the

contrast is about 49:1. The higher count rates for code 1 in both plots, as well as for code 21 in the length-40 case, are fully explained by theory. Due to the finite pulse-shaper resolution, sharp phase transitions from 0 to π introduce diffractive losses, a well-known effect in classical pulse shaping [1]. Since the first code possesses no such transitions (it consists entirely of zero-phase chips), and code 21 of Fig. 6.6(b) has only one transition, the net count rate after the coding and decoding process is appreciably higher for these cases than in the other codes with multiple π phase jumps.

To highlight the biphoton coding picture presented in Fig. 6.4, we also acquire full correlation functions for specific combinations in the length-40 Hadamard map. In Fig. 6.6(c) is shown encoding of the signal photon using code 28 from the two-dimensional map. For flat phase applied to both signal and idler, the correlation function possesses a narrow peak exceeding 9 000 s^{-1} in measured coincidences. (The peak surpasses that in Fig. 6.6(b) due to alignment reoptimization.) When code 28 is applied to the signal, the waveform spreads, and counts of only about 30 s^{-1} are measured at zero delay. The decoding process is verified in Fig. 6.6(d): applying code 3 to the idler keeps the correlation function spread, with a zero-delay SFG count rate of only about 60 s^{-1}, whereas when code 28 is applied, the biphoton regains its sharp peak. The height of the decoded peak is reduced to about two thirds that of the uncoded case, which again is in agreement with the expected drop from pulse-shaper resolution. These results confirm the conceptual depiction of Fig. 6.4, showing that we can indeed hide and recover a biphoton wavepacket in our coding scheme. Moreover, the fact that pulse-shaper resolution limits the maximum code length that can be implemented—introducing loss and waveform degradation as the chip bandwidth decreases—mirrors similar findings in orbital angular momentum, in which experimental imperfections have been shown to fix an optimum dimension beyond which the secure information capacity drops [130]. Proper code-length selection will therefore play an important role in developing our spectral coding approach in the context of QKD.

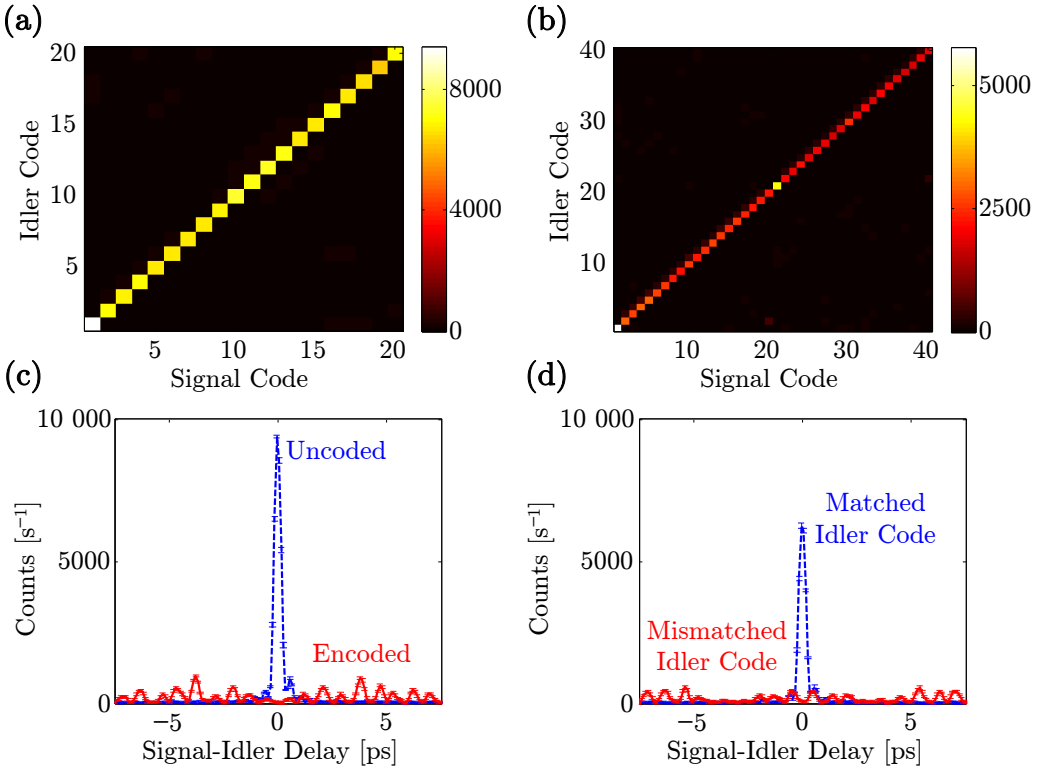

Fig. 6.6. Hadamard orthogonality for long sequences. (a) Measured coincidences [s^{-1}] at zero optical delay for all combinations in the $N = 20$ code family. (b) Coincidence map for length-40 codes. (c), (d) Specific example of length-40 coding. (c) With no codes applied, a sharp correlation function is measured, but when code 28 is applied to the signal, the peak disappears and the biphoton spreads. (d) Applying code 28 to the idler recovers the sharp correlation function, yet programming the wrong code (in this case, code 3) keeps the biphoton spread. Error bars give the standard deviation of five 1-s measurements, after dark count subtraction; linear interpolants connect the measured points.

While most Hadamard code combinations give results that appear essentially featureless, certain specializations can yield interesting wavepackets in their own right. For example, choosing a code of alternating 0's and π's for the signal and flat phase for the idler, we once again obtain orthogonality at zero delay, with the correlation function peak suppressed. However, the pattern's periodic nature yields values of optical delay for which the biphoton packet can produce large maxima. For a chip

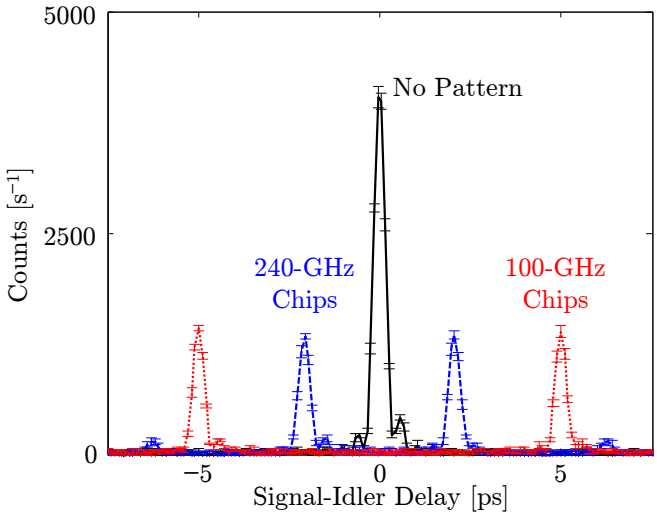

Fig. 6.7. Correlation doublet creation. The length-10 pattern, with 240-GHz chips, creates a separation of 4.2 ps; the length-24 pattern, comprised of 100-GHz chips, increases this separation to 10 ps. Again error bars show the standard deviation of five 1-s measurements, dark counts are subtracted, and linear interpolation is used to connect the measured points.

bandwidth of $\Delta\omega$, every other $\Delta\omega$ bin pair picks up a π phase shift, but as can be seen in Eq. (4.31), for delays $\tau = \pm\pi/\Delta\omega$, each bin acquires an additional spectral phase of 0, π, 2π, 3π, etc., which precisely compensates for the alternating pattern and allows each frequency pair to interfere constructively, producing a temporal peak. Additional local maxima surface at all odd multiples of the above delay, but the finite chip bandwidth suppresses them so that most of the optical energy is concentrated in the first two peaks about zero. This particular code therefore converts a single correlation peak into a doublet, with separation controlled by the chip rate. Figure 6.7 furnishes experimental examples, for 240- and 100-GHz chips. Theory is confirmed, as the generated peaks appear at ± 2.1 ps and ± 5 ps, respectively. Two subsidiary maxima are even discernible at ± 6.3 ps for the 240-GHz case, matching the odd-multiple prediction.

These coding experiments provide just a few examples of the possibilities available for biphoton manipulation based on optical codes. Our novel method for encoding of information in the spectral degree of freedom has potential for application not only in implementing multi-user QKD [131], but also in the development of new code-based time-frequency QKD protocols, as alternatives to previous proposals based on temporal modulation [68] or dispersion [69, 70]. Indeed, development of such a protocol represents one of the goals for future work addressed in the next chapter.

6.4 Biphoton Correlation Train Generation

The third application of ultrafast biphoton pulse shaping we consider focuses on a qualitatively different form of correlation: the two-photon frequency comb—that is, an entangled photon pair occurring in a superposition of discrete spectral mode pairs [133–142], rather than a continuous spectrum as considered heretofore. Such biphotons have the potential to combine the unique characteristics of quantum entanglement with the precision of classical optical frequency comb metrology [6, 7]. Several configurations generating such photonic states have been implemented, including spontaneous four-wave mixing in microresonators [142–144], cavity-enhanced SPDC [134–137, 141, 145], and direct filtering of broadband biphotons [139, 140]. Assuming phase locking of the constituent spectral modes, the temporal correlation function of these biphoton frequency combs consists of a train of peaks, the number of which is approximately equal to the spectral mode spacing divided by the linewidth. Indirect measurements based on HOM interference have revealed the periodic coincidence dips indicative of such correlation trains [134, 139, 140], and with sufficiently low repetition rates, direct correlation measurements have been made possible as well [135, 137, 141]. Moreover, it has been predicted theoretically [146] that propagation of these two-photon frequency combs through dispersive media will produce

The results in Section 6.4 have been published in [132].

revivals of the temporal correlation function at discrete dispersion values, through an extension of the classical temporal Talbot effect described in Section 2.2.

Specifically, we experimentally examine a new method for generating biphoton correlation trains based on optical pulse shaping. Our technique permits the creation of extremely high-repetition-rate (∼THz) trains, with programmable control of peak number and spacing. We explore both amplitude and phase filtering approaches, each with its own advantages. With amplitude filtering, we create coherent biphoton frequency combs with tunable properties and observe the two-photon temporal Talbot effect for the first time. Alternatively, when the temporal phase of the biphoton wavepacket is unimportant, we show that spectral phase-only filtering can yield correlation trains with much greater efficiency, even though the filtered spectrum does not contain a series of discrete frequencies—i.e., it is not comb-like.

The experimental setup matches that in the previous two sections [Fig. 6.1(a) with the pulse shaper in place], and as before the effect of pulse shaping is described by signal and idler filters as in Eq. (4.31). Now, however, we consider spectral filters designed to introduce multiple peaks in the temporal correlation function. Specifically, we first program an amplitude-only filter consisting of a series of separated passbands, converting the continuous biphoton spectrum into a set of discrete spectral lines which corresponds in the time domain to a pseudo-periodic train of peaks. We note that in this method there exists a fundamental tradeoff between overall flux and the number of peaks generated. Defining ω_c as the bandwidth of a given spectral passband and ω_{FSR} as the spacing between passbands, the total number of peaks in the train is proportional to the ratio $\omega_{\mathrm{FSR}}/\omega_c$, whereas the total power transmissivity is *inversely* proportional to this quantity [147]. Combined with the fact that the optical energy is now distributed among many peaks, the maximum count rate actually decreases quadratically with the number of correlation peaks. Therefore to remain comfortably above the background, we program on the signal spectrum three passbands spaced at 650 GHz, each with the fractionally broad bandwidth of 250 GHz, and leave the idler untouched. The measured signal spectrum is given in Fig.

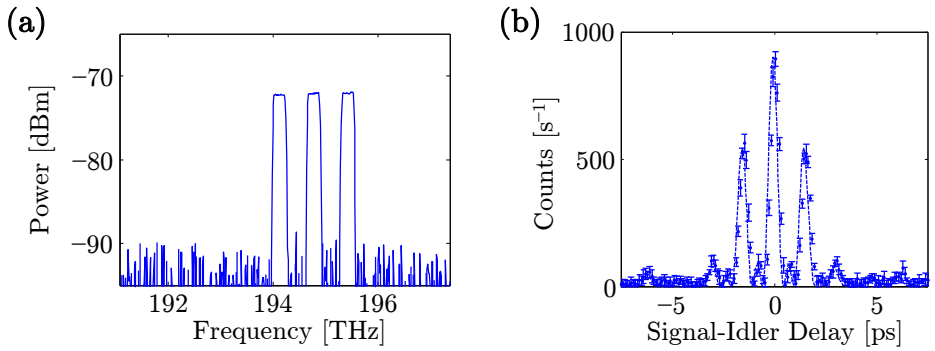

Fig. 6.8. Amplitude filtering. (a) Signal spectrum measured after the pulse shaper (with idler blocked). The nearly flat spectrum of Fig. 4.2(b) is converted to a set of three passbands, spaced by 650 GHz and each of width 250 GHz. (b) Measured temporal correlation function for the spectrum in (a), but with the low-frequency idler passed. A 650-GHz correlation train with three peaks is generated, in accordance with theoretical predictions (given by the dashed curve).

6.8(a), acquired with an optical spectrum analyzer at a resolution of 62.5 GHz. The spacing-to-passband ratio predicts about three temporal peaks, and this is precisely what we find for the filtered biphoton correlation function, as shown in Fig. 6.8(b). (Error bars represent the standard deviation of five 1-s measurements, and the dotted curve gives the theoretical result; this statement holds for all subsequent plots in this section as well.) The result is in excellent agreement with theory, confirming the ability to produce correlation trains through straightforward amplitude filtering by the pulse shaper.

This biphoton comb lends itself well to the examination of the temporal Talbot effect. For although the spatial Talbot effect has been observed with entangled photons [148, 149], its temporal counterpart has been analyzed only theoretically [146]. The origin of this effect for biphoton frequency combs can be understood most simply by considering the ideal case of a series of comb lines with infinitely narrow linewidths

followed by second-order dispersion—the same situation examined for a classical input in Section 2.2. Specifically, in Eq. (4.31) we take

$$H_s(\omega_0 + \Omega) = \sum_{n=0}^{N-1} a_n \delta(\Omega - n\omega_{\mathrm{FSR}}) e^{i\Phi_s^{(2)}\Omega^2/2} \tag{6.4}$$

and

$$H_i(\omega_0 - \Omega) = e^{i\Phi_i^{(2)}\Omega^2/2}, \tag{6.5}$$

which yields the final biphoton amplitude

$$\psi(\tau) = \sum_{n=0}^{N-1} \phi(n\omega_{\mathrm{FSR}}) a_n e^{i\Phi_+ n^2 \omega_{\mathrm{FSR}}^2/2} e^{-in\omega_{\mathrm{FSR}}\tau}, \tag{6.6}$$

where $\Phi_+ = \Phi_s^{(2)} + \Phi_i^{(2)}$, with the familiar Franson dispersion cancellation condition resulting when $\Phi_s^{(2)} = -\Phi_i^{(2)}$ [106]. As an aside, we note that the entanglement shared between signal and idler photons allows the same expression to be obtained when applying all narrowband filters on the idler instead, for it is only the *product* of signal-idler spectral filters which enters in Eq. (4.31). Returning to Eq. (6.6) we readily observe that the periodic wavepacket completely replicates itself for values of Φ_+ that are integer multiples of the Talbot dispersion Φ_T, where

$$\Phi_T = \frac{4\pi}{\omega_{\mathrm{FSR}}^2}, \tag{6.7}$$

as this ensures that the dispersion factor in Eq. (6.6) evaluates to unity for all n [34]. Taking the limit of infinitesimal linewidth for the signal spectrum shown in Fig. 6.8(a) gives the theoretical Talbot carpet shown in Fig. 6.9(a). At integer multiples of Φ_T, perfect reconstruction of the biphoton train is realized; at half-integer multiples, revivals with a half-period delay shift are obtained.

For real biphoton combs, the temporal train is not perfectly periodic, but damped by an envelope with duration inversely proportional to the non-vanishing linewidth, a well-known effect in classical pulse shaping [3]; therefore only approximate coherence revivals are possible. In particular, dispersion eventually spreads out the entire wavepacket, meaning that the self-imaging phenomenon is discernible only up to a

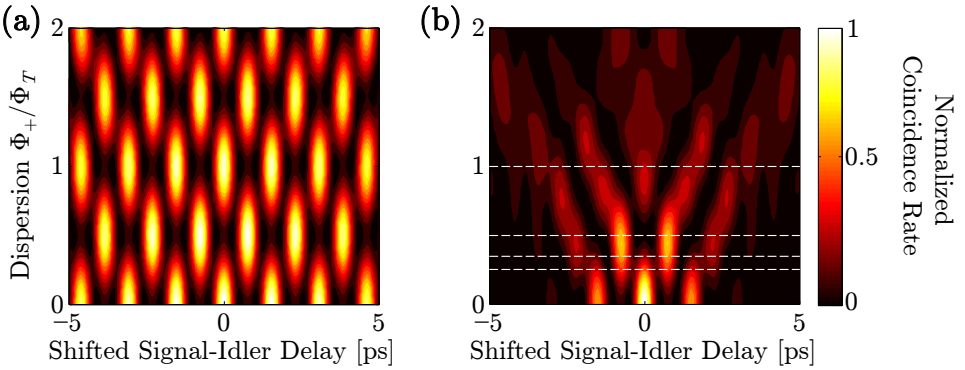

Fig. 6.9. Simulated Talbot carpets. (a) Theoretical temporal correlation as a function of applied dispersion, for our three-peak signal spectrum but with infinitely narrow linewidth. Perfect revivals are observed at integer multiples of the Talbot dispersion. (b) Corresponding correlation function when the linewidth is 250 GHz, as in Fig. 6.8(a). Dashed horizontal lines indicate the values of dispersion considered in Fig. 6.10. Imperfect—but still clear—self-imaging is obtained over the first Talbot length, limited by dispersive spreading. (An overall delay shift has been subtracted off for clarity.)

finite multiple of Φ_T [146]. With the fractionally large linewidth in our experiments ($\omega_{\mathrm{FSR}}/\omega_c = 2.6$), chosen to minimize loss, measurable Talbot interference is limited to approximately the dispersion regime $0 < |\Phi_+| < \Phi_T$. This is nevertheless sufficient to observe the basic effect. Figure 6.9(b) presents the theoretical Talbot carpet for our filtered biphoton source, plotting the temporal two-photon correlation function $\Gamma^{(2,2)}(\tau)$ as a function of net dispersion; horizontal lines mark the specific dispersions which we consider experimentally below. At each value of the dispersion, we have shifted the wavepacket center to zero delay, in much the same way as retarded time is calculated for classical pulses [30]. For in general, the applied dispersion introduces a frequency-dependent delay given by $\tau(\Omega) = \Phi_+\Omega$, and since the mean signal frequency offset $\langle\Omega\rangle \neq 0$, the mean signal-idler delay varies with applied dispersion. Intuitively, the fact that signal and idler are separated by frequency implies that group velocity dispersion forces them to travel at different mean speeds; therefore their av-

erage temporal separation increases as they propagate through greater amounts of dispersion.

As in the theoretical proposal of [146], we have specialized this development to the case of continuous-wave-pumped SPDC, in which the sum of signal and idler frequencies is fixed to a single value. If short-pulse pumping were considered instead, signal and idler would then be correlated about a range of frequencies, and we expect this broadened correlation bandwidth to impose an additional temporal envelope analogous to those resulting from finite filter linewidth or pulse-shaper resolution. Thus when the pump bandwidth exceeds these other characteristic frequencies, the correlation train would be severely damped. Yet for a pump whose spectrum is still narrower than the other relevant frequency scales, we expect self-imaging to nevertheless be observable. Accordingly, it would be interesting to explore the effects of such pulsed pumping in future studies—particularly the transition from the short- to long-pulse regimes—although for this first demonstration we focus on the more direct continuous-wave limit.

Experimentally, we explore the temporal Talbot effect by programming the optical dispersion directly on the pulse shaper and observing the change to the biphoton correlation function of Fig. 6.8(b). As before, measurement of $\Gamma^{(2,2)}(\tau)$ is made possible by applying additional, oppositely sloped linear spectral phase terms to the signal and idler spectra, to programmably control the relative delay. For our 650-GHz correlation trains, the Talbot dispersion parameter Φ_T is 0.753 ps^2, and we apply net dispersions satisfying

$$\Phi_+ = 0.25\Phi_T, 0.35\Phi_T, 0.5\Phi_T, \Phi_T. \tag{6.8}$$

The result for the quarter-Talbot case is presented in Fig. 6.10(a). The correlation train has doubled in repetition rate to 1.3 THz and matches theory well. Similar quarter-Talbot-based repetition-rate multiplication has been used to generate classical pulse trains as well [150–152]. In Fig. 6.10(b), the dispersion is now 35% of the Talbot value, with the odd peaks increasing in relative magnitude and the even ones falling off, a transition which is made complete at the half-Talbot mark, as highlighted in

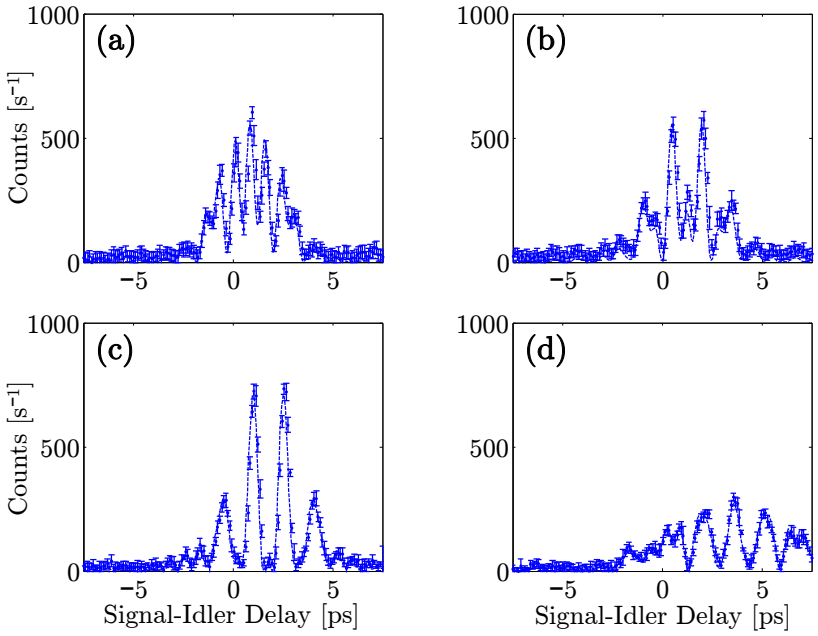

Fig. 6.10. Examples of Talbot interference. Biphoton correlation functions measured for dispersion Φ_+ equal to (a) $0.25\Phi_T$, (b) $0.35\Phi_T$, (c) $0.5\Phi_T$, and (d) Φ_T. Dashed lines represent simulation predictions, scaled separately for each plot.

Fig. 6.10(c). High-extinction peaks at 650 GHz are again clearly evident, shifted under the envelope by half a period with respect to the zero-dispersion case. Finally, the function is returned to its original state at a full Talbot dispersion [Fig. 6.10(d)], although the effects of finite linewidth are taking their toll as the train spreads out, resulting in a lower maximum count rate and the formation of extra satellite peaks.

For direct comparison of the coherence revivals, we numerically correct for the temporal offset due to signal-idler group velocity difference and overlay the zero-, half-, and full-Talbot correlation functions in Fig. 6.11(a), which clearly shows resurgence of the 650-GHz train due to temporal Talbot interference. In likewise fashion, we superpose the quarter- and zero-Talbot results in Fig. 6.11(b), highlighting the repetition-rate doubling. Such rate multiplication through the temporal Talbot effect is particularly advantageous in that it is achieved without removing spectral lines,

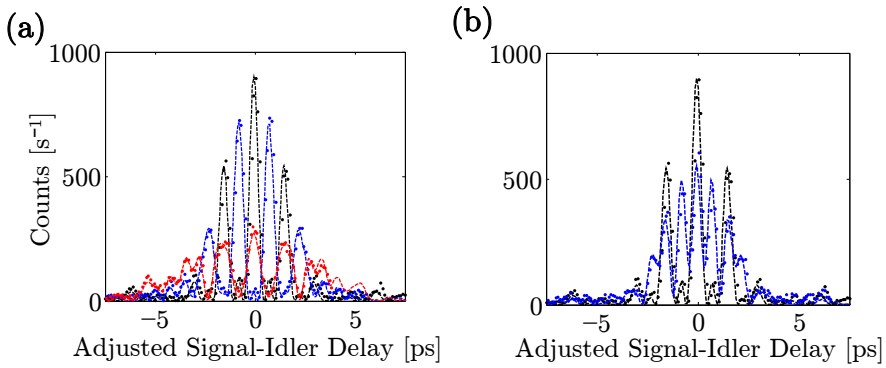

Fig. 6.11. Coherence revival comparison. (a) Overlay of the zero-, half-, and full-Talbot cases, after delay correction to center all at zero delay. 650-GHz trains are seen in all cases, with the finite linewidth responsible for overall spreading. (b) Overlay of the zero- and quarter-Talbot cases, again shifted so both are centered at zero delay. The original 650-GHz train is doubled to 1.3 THz at the quarter-Talbot dispersion, as expected from theory.

which would instead reduce overall flux by an amount equal to the frequency multiplication factor [153–155]. Notwithstanding the ultrahigh efficiency of the ultrafast biphoton correlator we use [87], an obvious goal for the future would be to realize even higher detection efficiencies, which would permit demonstrations with narrower spectral filters and hence longer trains. Nonetheless, the current experiments fully confirm the theory of [146] in extending the temporal Talbot effect to biphotons.

For circumstances in which the temporal biphoton phase is unimportant, and one is concerned only with the correlation function itself, an alternative method based on spectral phase-only filtering can be used to produce correlation trains much more efficiently than amplitude filtering, utilizing a technique developed early in the history of classical femtosecond pulse shaping [147] and applied to, e.g., control of molecular motion [156]. To understand this approach, consider the modulus squared of Eq. (4.31), where we define $K(\Omega) = \phi(\Omega)H_s(\omega_0 + \Omega)H_i(\omega_0 - \Omega)$ for simplicity. This allows us to write the fourth-order correlation function as

$$\Gamma^{(2,2)}(\tau) = \int d\Omega \int d\Omega' \, K^*(\Omega)K(\Omega')e^{i(\Omega-\Omega')\tau}. \tag{6.9}$$

Redefining a new integration variable Δ according to $\Delta = \Omega' - \Omega$ and replacing Ω' gives

$$\Gamma^{(2,2)}(\tau) = \int d\Delta\, e^{-i\Delta\tau} \int d\Omega\, K^*(\Omega) K(\Omega + \Delta). \tag{6.10}$$

Thus the measured correlation function is given by the inverse Fourier transform of the autocorrelation of the filtered biphoton spectrum, and so the condition for a periodic train requires only that this *autocorrelation* consist of discrete peaks—$K(\Omega)$ itself need not be comb-like. In our case, we achieve the desired spectral peaks by taking $H_i(\omega) = 1$ and choosing $H_s(\omega)$ to be a periodic repetition of a maximal-length binary phase sequence (M-sequence) [157], which indeed possesses discrete spikes in its autocorrelation. Since the input biphoton spectrum is essentially flat over the pulse-shaper passband, no additional amplitude equalization is required, and so the spectral filtering is ideally lossless. In stark contrast to amplitude filtering, the maximum count rate drops only linearly with the number of peaks generated by phase filtering—instead of quadratically—thereby offering the potential for significantly longer biphoton trains at a given flux. However, we emphasize that temporal interference effects, such as the Talbot phenomenon, do not carry over to these non-comb-like states, since the inter-peak temporal phase varies widely.

We first consider the length-7 M-sequence [0 1 1 1 0 1 0], where we map the zeros to phase 0 and the ones to phase π. Each element is programmed to cover a bandwidth of 115 GHz, giving a total of three repetitions of the M-sequence over the 2.415-THz signal passband set on the pulse shaper here. The measured correlation train is presented in Fig. 6.12(a), again showing good agreement with theory. The missing peak at zero delay results from destructive interference between the 0 and π phase elements. We can restore the central peak by changing the binary phase shift; taking 0.78π for the shift instead of the original π, we obtain the blue curve in Fig. 6.12(b). A high-contrast train at 805 GHz is generated under a smooth envelope, without any amplitude filtering of the biphoton spectrum.

To directly compare the flux improvement over the equivalent amplitude filter, we also program three repetitions of the amplitude sequence [1 0 0 0 0 0 0] over the

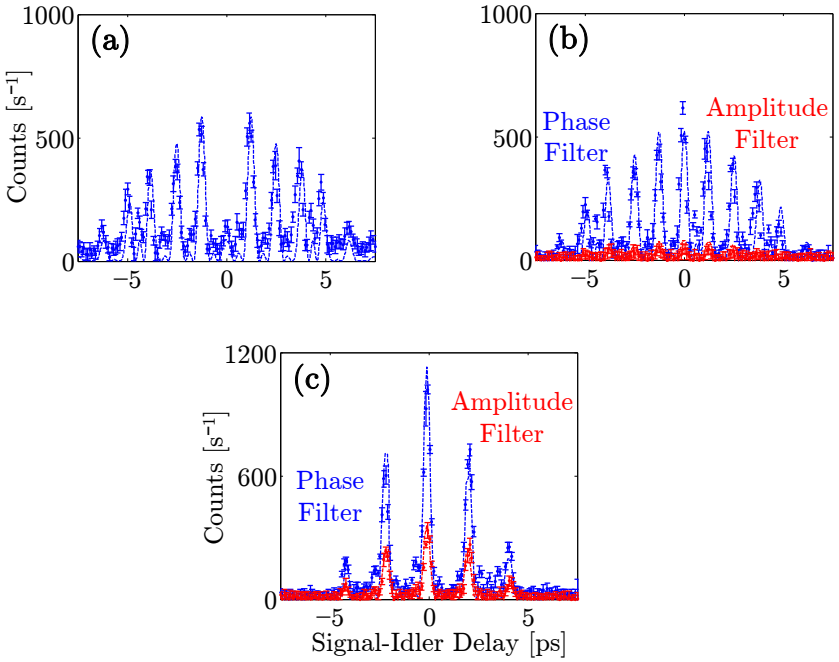

Fig. 6.12. M-sequence filtering. (a) Measured correlation function for length-7 M-sequence with a π phase shift. (b) Correlation function for the same M-sequence but with a 0.78π phase shift (blue), compared to an amplitude filter at the same repetition rate (red). (c) Correlation function for a length-3 M-sequence with a 0.65π phase shift (blue) and the corresponding amplitude filter. Dashed lines give theoretical predictions for all results. In both (b) and (c), phase filtering yields a flux improvement roughly equal to the number of peaks.

same bandwidth, which gives the desired 805-GHz train but at the cost of removing much of the original biphoton spectrum. This result (red curve) is compared to the phase-only approach in Fig. 6.12(b); the amplitude case is reduced approximately 7-fold in integrated flux and is barely visible above the noise. We run a similar comparison for length-3 sequences as well, giving each symbol a bandwidth of 160 GHz and replicating the sequence five times over a 2.4-THz total signal bandwidth. For the phase filter, we use the M-sequence [1 0 1], where ones now map to a phase shift of 0.65π; for the amplitude filter, we take the transmission sequence of [1 0 0]. Both results are compared in Fig. 6.12(c), and a count rate improvement of about

3:1 is observed for the phase-only sequence. These results stress the substantial flux increases facilitated by pure phase filtering, which—coupled with the programmable control of peak number and spacing—make such states valuable tools for future work with high-repetition-rate biphotons.

Yet despite the considerable improvement in biphoton flux effected by phase-only filtering, both amplitude and phase approaches face a separate restriction which limits the maximum length of obtainable biphoton trains: pulse-shaper time aperture. The time aperture, or the maximum temporal duration over which the shaped waveform will accurately reproduce that of the ideal infinite-resolution mask, is fixed by the resolvable frequency spacing [1–3]. If we model this temporal window as a Gaussian function with an intensity FWHM $T_{\mathrm{FWHM}} = (2\ln 2)^{1/2}T$, the effect of finite resolution is to yield the impulse response $h(t)$ [the inverse Fourier transform of the transfer function $H(\omega)$]

$$h(t) = h^{(0)}(t)e^{-t^2/T^2}, \tag{6.11}$$

where $h^{(0)}(t)$ is the impulse response corresponding to an infinite-resolution pulse shaper. Therefore the generated trains are restricted to a time window roughly equal to the inverse of the spectral resolution. Now when the characteristic frequency scale $\delta\omega$ over which the ideal mask $H^{(0)}(\omega)$ varies satisfies $1/\delta\omega \ll T$, $h(t) \approx h^{(0)}(t)$, and the effects of finite resolution are negligible (which was the case in the previous experiments). However, to explicitly examine the limits of our biphoton correlation train generator, now we choose filter functions that are significantly modified by the time aperture. Moreover, because we use the pulse shaper not only for generation but also for imposing the relative signal-idler delay, we suffer on two counts: first in the creation of the correlation train, and second in its measurement. Letting $\tilde{\psi}(\tau)$ denote the measured wavepacket under the effects of finite pulse-shaper resolution, to best reflect the experimental conditions of our measurement, the expression in Eq. (4.31) must be modified to

$$\tilde{\psi}(\tau) = \int d\Omega\, \phi(\Omega)\tilde{H}_s(\omega_0 + \Omega, \tau/2)\tilde{H}_i(\omega_0 - \Omega, -\tau/2), \tag{6.12}$$

where the delay τ is explicitly imposed by the filters, with the signal temporally shifted by $\tau/2$ and the idler by $-\tau/2$ [72]. The corresponding infinite-resolution filters are thus

$$\tilde{H}_s^{(0)}(\omega_0 + \Omega, \tau/2) = C(\Omega)e^{-i\Omega\tau/2} \tag{6.13}$$

and

$$\tilde{H}_i^{(0)}(\omega_0 - \Omega, -\tau/2) = e^{-i\Omega\tau/2}, \tag{6.14}$$

where $C(\Omega)$ is the ideal spectral code applied to the signal photon. The finite-resolution filters $\tilde{H}_s(\omega, \tau)$ and $\tilde{H}_i(\omega, \tau)$ are obtained by convolving $\tilde{H}_s^{(0)}(\omega, \tau)$ and $\tilde{H}_i^{(0)}(\omega, \tau)$ with the Fourier transform of the time aperture function e^{-t^2/T^2}. In this way we can incorporate the effect of finite resolution on both the spectral code and imposition of signal-idler delay.

Experimentally, we take the same periodically repeated length-3 phase sequence as before ([0.65π 0 0.65π]), but this time consider very narrow spectral chips. In order to correct for count-rate reduction due to alignment drift, we normalize each correlation function to a peak value of unity; since the time aperture term is equal to one at zero signal-idler delay, such renormalization has no effect on examination of aperture effects. In the first case, we program a chip bandwidth of 16 GHz, for a total of 50 repetitions of the fundamental sequence over the 2.4-THz signal bandwidth; the measured correlation function is given in Fig. 6.13(a). Compared to the 160-GHz chip case in Fig. 6.12(c), the peak separation has been pushed from 2.1 to 21 ps, and the two side peaks are lowered slightly in relative intensity by the pulse-shaper time aperture. Further reductions are evident for even smaller chips; Fig. 6.13(b) shows the results for 9-GHz chips (total signal bandwidth 2.403 THz), and Fig. 6.13(c) those for 5-GHz chips (2.4-THz total signal bandwidth). We find that a value for T of 50 ps ($T_{\mathrm{FWHM}} = 58.9$ ps) gives good agreement with the observed peak reduction, as evident by the dotted theoretical curves in Fig. 6.13. This experimentally measured time aperture corresponds to a 3-dB spectral resolution of about 7.5 GHz, slightly better than the 10 GHz specified for the WaveShaper 1000S. From these results, it is clear that pulse-shaper resolution limits the overall duration of the generated

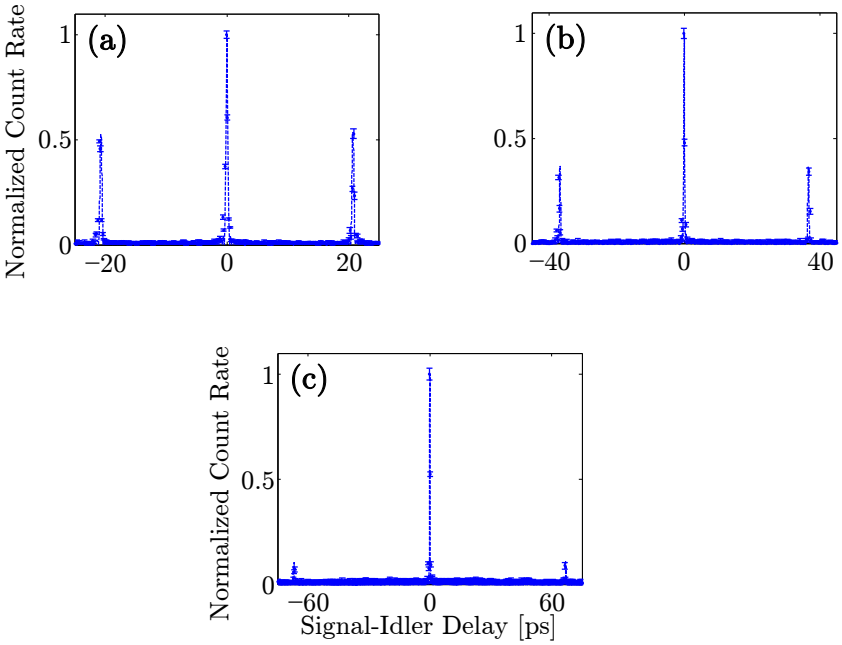

Fig. 6.13. Examination of pulse-shaper time aperture. Normalized coincidence rate for periodic repetitions of length-3 M-sequences with (a) 16-GHz chips, (b) 9-GHz chips, and (c) 5-GHz chips. The theoretical curves (dashed lines) are obtained with $T = 50$ ps in Eq. (6.11).

biphoton correlation function to a window of around 60 ps. Any detection schemes with slower response times are therefore unable to resolve these correlation trains, so while this phase-only filtering method is well suited for programmable generation of high-repetition-rate biphoton trains, the narrow linewidth available from resonant photon-pair generation [134–137, 141–145] or filtering with an etalon [139, 140] would prove more appropriate when temporally long trains are required.

6.5 Tunable Delay Control

The fourth and final set of experiments on ultrafast biphoton manipulation focuses on programmable control of signal-idler delay. In classical photonics, tunable delay systems are used in a variety of applications, including metrology and commu-

The results in Section 6.5 have been described in [158].

nications [34, 159]. In its most basic form, delay control can be realized by simply varying the optical path length traversed by the field through the system. Unfortunately, the switching speed of this approach is limited to the ∼kHz range by the mechanical motion of a delay stage or mirror. Alternatively, drastically faster modulation is possible through a setup using wavelength conversion followed by dispersion [160]. Since different frequencies propagate at distinct group velocities through a dispersive medium, the amount of wavelength shift applied to the input field (either through electro-optic modulation or nonlinear mixing) maps directly to the delay of the output; thus, by tuning the frequency shift, it is possible to modulate the applied delay, in some cases with GHz switching speeds [159]. However, this delay comes at a price: dispersion not only shifts the arrival time, but also causes the pulse to spread. Therefore compensation is typically achieved by propagating through equal and opposite group velocity dispersion, either before shifting the original wavelength or after shifting the output wavelength back to its original value [160, 161].

Building on these classical systems, we propose and demonstrate tunable delay control of nonclassical time-frequency entangled photons for the first time, through shifting the pump frequency and propagating the generated biphotons through optical dispersion. By exploiting the effect of nonlocal dispersion cancellation described in detail in Sec. 6.2, we can also compensate for the spreading which would otherwise degrade the sharpness of the temporal correlations. A schematic of this concept is shown in Fig. 6.14. Unlike the classical case, delay shifting and dispersion compensation occur simultaneously, circumventing the need for a second wavelength shifter or dispersive medium, and highlighting a unique advantage of quantum entanglement. We note that this new method for entangled photon control represents a quantum optical analogue of classical pulse-position modulation.

The origin of such tunable delay is readily observed on taking two second-order dispersive filters in Eq. (4.31). Specifically, if we consider equal and opposite signal

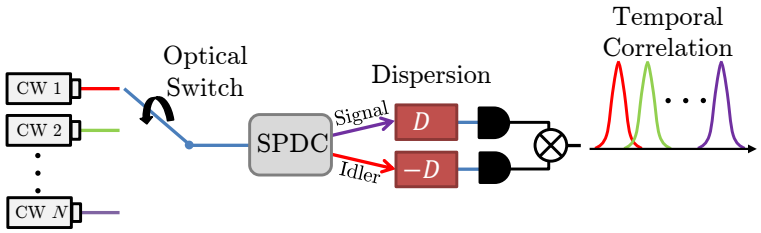

Fig. 6.14. General scheme for delay control of time-frequency entangled photons through pump frequency tuning and propagation in dispersive media.

and idler dispersion coefficients such that $H_s(\omega) = \exp[iA(\omega-\omega_0)^2/2]$ and $H_i = \exp[-iA(\omega-\omega_0)^2/2]$, Eq. (4.31) reduces to the simple result

$$\psi(\tau) = \int_0^\infty d\Omega\, \phi(\Omega) e^{-i\Omega\tau} \equiv \psi_0(\tau), \tag{6.15}$$

and we recover the original biphoton, unaffected by dispersion—i.e., dispersion cancellation. Yet as examined in Sec. 6.2, opposite signs of dispersion give cancellation only for even spectral phase orders; for odd orders, opposite signs add cumulatively. This implies an important distinction between delay (first-order spectral phase) and second-order dispersion, for if we detune the center frequency of the biphotons relative to the quadratic dispersion by an amount $\delta\omega$ such that $\omega_0' = \omega_0 + \delta\omega$ is the new center, the fixed filters H_s and H_i now introduce additional phase terms linear in frequency, which *add* rather than cancel. Specifically, $H_s(\omega_0'+\Omega)H_i(\omega_0'-\Omega) = \exp(2iA\delta\omega\Omega)$ and the biphoton wavepacket is of the form

$$\psi(\tau) = \int_0^\infty d\Omega\, \phi(\Omega) e^{-i\Omega(\tau-2A\delta\omega)} = \psi_0(\tau - 2A\delta\omega). \tag{6.16}$$

The additional phase term $\exp(i2A\Omega\delta\omega)$ directly corresponds to a temporal delay of $2A\delta\omega$, proportional to both the strength of the dispersion and magnitude of the frequency tuning. In this way the delays imparted by the signal and idler dispersive media are retained, while the associated wavepacket spreading is removed, a fortuitous situation made possible by the spectral anticorrelation of the entangled state. Moreover, in principle the size of this delay per unit frequency is unbounded, provided

sufficiently strong and low-loss dispersive media are available, although in the experiment described below, we do suffer from additional limitations. Nevertheless, this finding indicates that by simply shifting the pump laser frequency, one can modulate the relative arrival times of entangled photons with minimal impact on the shape of their correlation. In contrast to tunable optical delay lines requiring mechanical adjustment, the filters here are fixed, so that our scheme could be implemented rapidly by simply switching between pump lasers along a fixed frequency grid—although we have not yet examined this possibility in our preliminary experiments.

To realize the necessary antisymmetric quadratic phase, we again exploit the flexibility of our high-resolution pulse shaper, making use of the experimental setup of Fig. 6.1(a) for biphoton control and ultrafast coincidence detection. And because of the pulse shaper's programmability, we are also free to consider an alternative delay scenario. In the proposed arrangement above, we assume fixed dispersion and a tunable pump laser; this is most compatible with previous classical approaches and rapid switching capabilities. But the basic physics is based only on modulation of the *relative* frequency spacing between the dispersion and SPDC center, so equivalently we can fix the pump-laser wavelength and shift the center of the antisymmetic quadratic phase imparted by the pulse shaper, a practically simpler endeavor which we tackle first. However, before delving into these experiments, it is profitable first to address in more detail the limitations imposed by our pulse shaper. In the simple development above, we have assumed signal and idler are perfectly distinct and experience quadratic spectral phase over a bandwidth wider than what they occupy. Yet because of the nature of the downconversion process here, portions of the signal and idler spectra can pass through the wrong filter; and due to the 5-THz pulse-shaper bandwidth, additional loss is incurred for frequency shifts approaching the band edge.

To place these general comments on a concrete footing, we more precisely model the signal and idler spectral filters as

$$H_{s,i}(\omega) = \begin{cases} 0 & ; \quad \omega < \omega_L \\ e^{-iA(\omega-\omega_0)^2/2} & ; \quad \omega_L < \omega < \omega_0 \\ e^{iA(\omega-\omega_0)^2/2} & ; \quad \omega_0 < \omega < \omega_H \\ 0 & ; \quad \omega_H < \omega. \end{cases} \tag{6.17}$$

Here ω_L and ω_H are the lower and upper cutoff frequencies of the pulse shaper, and from now on we take ω_0 as the center frequency of the antisymmetric phase and ω_0' as that of the biphoton. Since both photons propagate through the same physical pulse shaper, the signal and idler filters can formally be taken as identical—the difference is the frequencies at which they are evaluated. For example, when $\omega_0' = \omega_0$, none of the signal spectrum will "see" a dispersion coefficient of $-A$ (vice versa for the idler), and we can unambiguously assign unique phase filters to each photon; such was the case in our previous dispersion cancellation experiments. Now, though, when one of the frequencies ω_0 or ω_0' is shifted ($\delta\omega \neq 0$), some signal-idler frequency pairs will experience the *same* sign of dispersion and temporally spread.

Taking the above form for $H_s(\omega)$ and $H_i(\omega)$ and inserting them into Eq. (4.31) (with ω_0' as the biphoton center frequency), we obtain the more complicated wavepacket

$$\psi(\tau) = \int_{|\delta\omega|}^{\Delta} d\Omega\, \phi(\Omega) e^{-i\Omega(\tau - 2A\delta\omega)} + e^{\pm iA\delta\omega^2} \int_0^{|\delta\omega|} d\Omega\, \phi(\Omega) e^{-i\Omega(\tau \mp A\Omega)} \quad ; \quad \delta\omega \gtrless 0, \tag{6.18}$$

where the upper (lower) conditionals are taken when the detuning $\delta\omega$ is greater (less) than zero, and $\Delta = \min\{|\omega_H - \omega_0'|, |\omega_L - \omega_0'|\}$. The first integral has the desired time-shift form, but now only the signal spectrum with offset frequency in the interval $(|\delta\omega|, \Delta)$ contributes. The second integral shows that the offsets less than $|\delta\omega|$ experience a net quadratic dispersion and thereby spread. Therefore, both increasing the relative frequency shift $\delta\omega$ and moving the pump frequency toward either edge of the pulse shaper passband lower the bandwidth and energy of the time-shifted portion of the biphoton, introducing observable distortion. These effects explain well

the experimental results below, but we emphasize that this nonideality stems only from the nature of the experiment here and is not inherent to the method itself. For example, in situations where it is possible to spatially separate signal and idler for all pump frequencies (e.g., in noncollinear or type-II downconversion), one could ensure that the entire spectrum of each photon sees the desired dispersion, giving perfect cancellation at all delay shifts.

With these considerations in mind, we first demonstrate tunable delay control by keeping the pump wavelength fixed and shifting the dispersion curve applied by the pulse shaper. Figure 6.15(a) shows the phase applied in each of the five cases considered. We take as dispersion coefficient $A = 3/\pi$ ps^2 and examine frequency shifts of $\delta\omega = 2\pi p \times 250$ GHz, where p is an integer from the list $[-2\ -1\ 0\ 1\ 2]$. Because the pump remains fixed, we employ a PPLN waveguide with a uniform poling pattern for maximum efficiency. Figure 6.15(b) displays the second-harmonic-generation efficiency as a function of pump frequency for the waveguide used for SFG; the waveguides for both SPDC and SFG have similar forms. Stepping through each of the frequency shifts, we find the results in Fig. 6.15(c) (theory) and Fig. 6.15(d) (experiment). As expected, the signal-idler delay is shifted by integer multiples of 3 ps, with the reduction in peak probability away from zero delay—and even the small $\sim$5-ps-wide pedestals for $p = \pm 2$—in good agreement with theory, thus corroborating the development culminating in Eq. (6.18).

We now move on to our main demonstration of biphoton tunable delay: tuning the pump frequency relative to a fixed antisymmetric dispersion profile. The pump-dispersion relationship is now given by Fig. 6.16(a). As before, the dispersion coefficient A is $3/\pi$ ps^2, but now the biphoton center frequency is shifted; the numerical labels in Fig. 6.16 again correspond to the value of p in the expression $\delta\omega = 2\pi p \times 250$ GHz. Since the PPLN waveguides used in all experiments up to this point accept only a small range of pump wavelength ($\sim$0.1 nm), and so are not suited for the $\sim$nm pump shifts required in this experiment, we now employ PPLN waveguides with phase-modulated poling patterns designed to give roughly equal down-conversion ef-

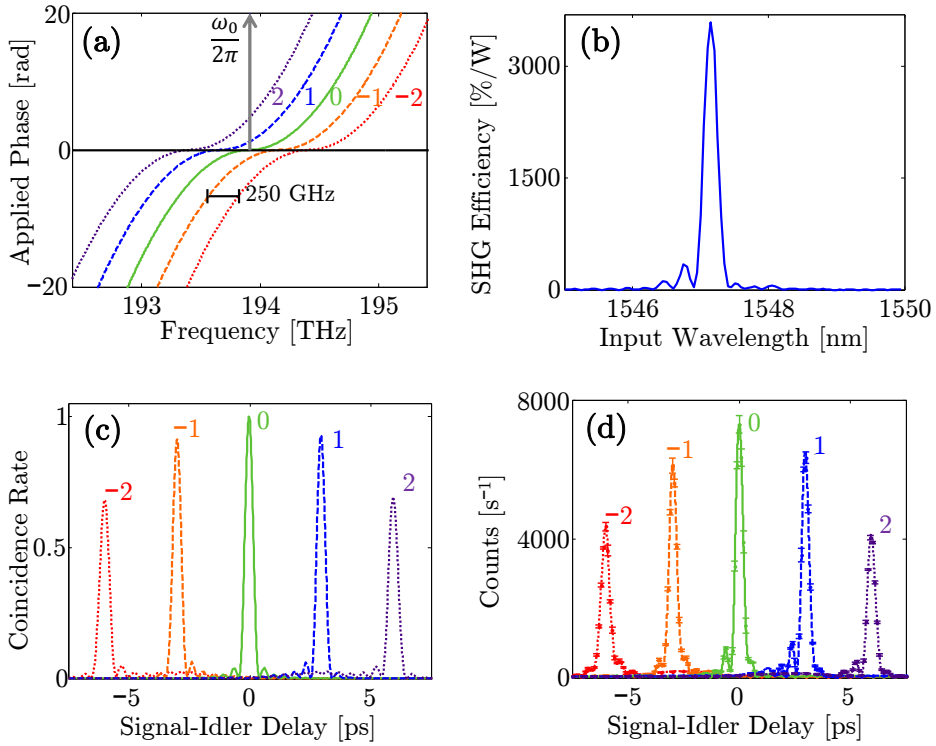

Fig. 6.15. Experiments with fixed pump. (a) Schematic of a fixed pump with shifts in the antisymmetric dispersion curve, displayed over 3 THz of the 5-THz pulse shaper window. (b) Phase-matching curve for PPLN waveguide with a uniform poling pattern. (c) Theoretical and (d) experimental results showing delay control of the biphoton correlation function. The numbers [−2 −1 0 1 2] correspond to the amount the dispersion curve is shifted in each case, in units of 250 GHz. The curves connecting the measured results in (d) were obtained via cubic spline interpolation.

ficiency at five distinct pump wavelengths [162]. Figure 6.16(b) shows an example phase-matching curve of this grating, suggesting comparable down-converted power at each frequency. Ideally, for a fixed waveguide length, the integrated efficiency remains constant over different poling patterns, and therefore the maximum efficiency drops for the five-wavelength guide by roughly a factor of 5, as evident in comparing Figs. 6.15(b) and 6.16(b). This reduced efficiency, impacting both SPDC and SFG, is the main reason for the added difficulty of these experiments. Theoretical results [Fig.

6.16(c)] and measurements [Fig. 6.16(d)] again display good agreement, although the total count rate is diminished by the lower nonlinear efficiencies. Moreover, the relative height of the shifted peaks (compared to the $p = 0$ case) are appreciably shorter for the pump-shifted implementation than the dispersion-shifted approach; cf. Figs. 6.15(c) and 6.16(c) or Figs. 6.15(d) and 6.16(d). The origin of this additional suppression is exposed by Eq. (6.18): the energy and height of the desired shifted correlation peak is limited by $\delta\omega$ and Δ; the former is identical for the shifts in both experiments, but the latter is not. When the pump ω_0' is fixed, $\Delta = \min\{|\omega_H - \omega_0'|, |\omega_L - \omega_0'|\}$ remains unchanged for all values of p. Yet when the pump is frequency-shifted, Δ decreases for larger values of $|p|$ as more of the biphoton is eliminated by the band edge of the pulse shaper. It is precisely this additional nonideality which causes the more pronounced reduction in relative count rates in Fig. 6.16.

One useful metric to characterize system performance is the fractional delay: the ratio of the delay of the correlation peak to the FWHM of the zero-delay correlation function. We adopt this from a common figure of merit in classical delay lines, where one takes the ratio of the output pulse delay to the input pulse width [163]. Another metric we include is the normalized peak number of counts, which provides a measure of the fraction of each biphoton successfully shifted in delay—and accordingly some information about the distortion. In the case of a fixed pump with shifts in the dispersion profile, the measured correlation peaks for $\pm$250- and $\pm$500-GHz shifts correspond to fractional delays of $\pm$7.5 (normalized peak count rate at 87%) and $\pm$15 (normalized peak count rate at 58%), respectively, while in the case of a fixed dispersion profile with shifts in the pump frequency, we obtain the same fractional delays but now with normalized peak count rates at 73% and 38%. These results are confirmed by simulation (Fig. 6.17)—we emphasize that our simulation results account for the segments of the biphoton spectrum that experience the same sign of dispersion and the finite bandwidth of our pulse shaper, both of which contribute to reduced count rates for delayed correlations. As a side note, if we are not limited by the pulse shaper bandwidth, we predict fractional delays up to $\pm$60 should be possible

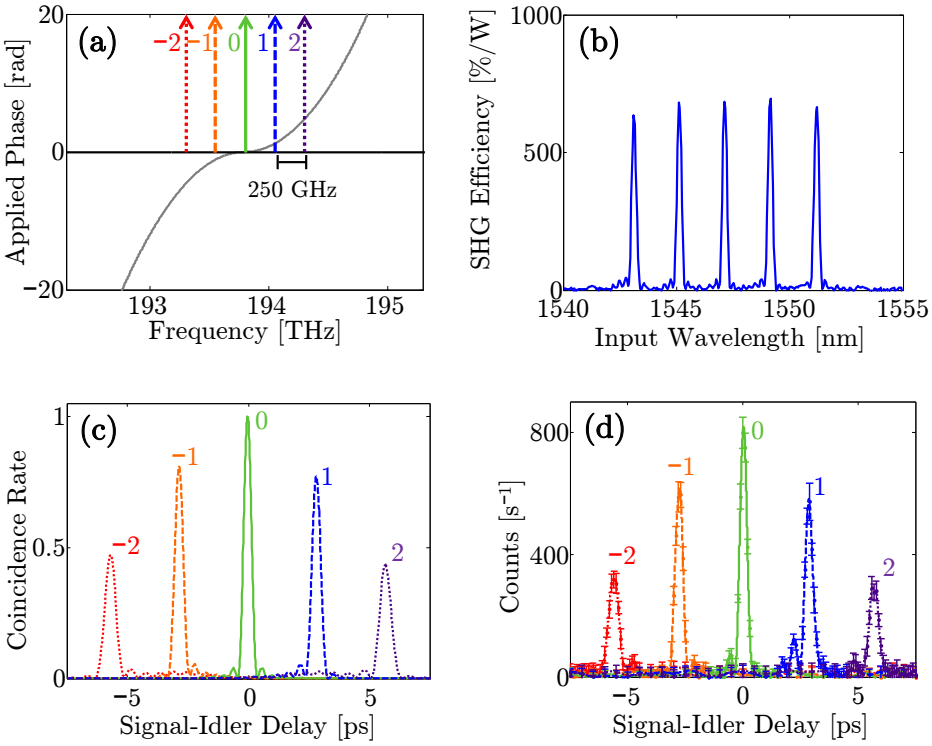

Fig. 6.16. Experiments with fixed dispersion. (a) Schematic of the fixed antisymmetric dispersion curve with shifts in pump frequency, displayed over 3 THz of the 5-THz pulse shaper window. (b) Phase-matching curve for PPLN waveguide with a non-uniform poling pattern. (c) Theoretical and (d) experimental results showing delay control of the biphoton correlation function. The numbers [−2 −1 0 1 2] correspond to the amount the center frequency of the biphoton is shifted in each case, in units of 250 GHz; the experimental results in (d) are connected with cubic spline interpolants.

while maintaining a normalized peak count rate exceeding 50%. In fact, much longer fractional delays can be achieved by increasing the value of our dispersion constant A; however, we cannot increase A without bound due to the finite resolution of our pulse shaper. Based on previous tests with this pulse shaper (Section 6.4), we anticipate maximum absolute delay shifts up to around ±30 ps.

In summary, we have described and demonstrated a new way to tune the temporal position of the fourth-order correlation function for entangled photons. By shifting

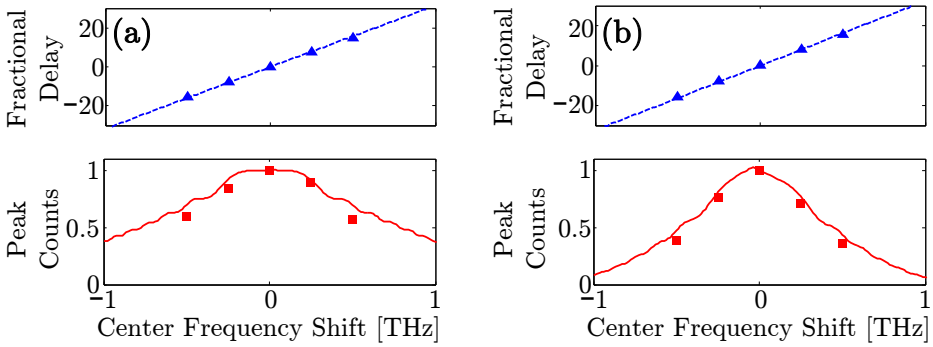

Fig. 6.17. Fractional delay and normalized peak count rate versus shift in center frequency for (a) the case of a fixed pump with shifts in the antisymmetric dispersion curve and (b) the case of a fixed antisymmetric dispersion curve and shifts in pump frequency. The markers denote experimental results; the curves, simulation.

the frequency of the pump and applying dispersion cancellation, we can control the relative delay of signal and idler photons without introducing significant distortion. We believe that our scheme will be useful for delay correction in time-energy quantum key distribution systems. In future experiments, optical fibers and chirped fiber Bragg gratings could be used to provide the necessary dispersion, replacing the pulse shaper and in principle permitting much longer delays that are resolvable with electronic coincidence detection. Finally, it will be interesting to explore some other capabilities with this technique, such as rapidly modulating the pump frequency and encoding it with binary information.

6.6 Conclusion

The four sets of biphoton experiments described in this chapter—high-order dispersion cancellation, spectral coding, generation of correlation trains, and tunable delay control—herald not only new technical capabilities in the manipulation and measurement of entangled photon states, but also the demonstration of new physics: e.g., the first detailed tests of high-order dispersion cancellation and the first ob-

servation of the biphoton temporal Talbot effect. Furthermore, experiments such as orthogonal spectral coding and tunable delay control reveal how classical optical communication techniques offer unique potential in quantum systems. For this reason, our work represents so much more than simply a reprise of experiments realized at high power now at low light levels, for the quantum systems furnish new opportunities for nonlocal and paradoxical effects. Therefore we are only just beginning to uncover the full potential at the interface between classical signal processing and quantum information; the results demonstrated here should provide a valuable springboard for practical developments in the future.

7. OUTLOOK

7.1 General Comments

The experiments chronicled in this dissertation represent significant contributions to the fields of temporal cloaking and biphoton pulse shaping. In realizing high-speed temporal cloaks compatible with optical communications, we look to bring time cloaking to the verge of practical application; in manipulating the correlations of entangled photon pairs with unprecedented sophistication, we hope to enable new tools for novel quantum information systems. Due to the relative youth of both of these fields, predicting exactly what role our work will ultimately assume is a nebulous endeavor. Nonetheless, in this concluding chapter we provide our educated guesses on what research avenues to pursue—and how we envision these fields to mature in the future.

7.2 Temporal Cloaking

Of the two, temporal cloaking is perhaps the most uncertain. Proposed a mere four years ago [25] and first demonstrated in 2012 [28], relatively few researchers have entered the field; indeed, apart from our work [11, 46], only one other experiment has surfaced since 2012 [164], and this example would more accurately be classified as a "polarization cloak," for it utilizes polarization scrambling to hide events rather than creating true temporal gaps. And in none of these examples has the practical question of combining time and spatial cloaking been evaluated in any detail. Nevertheless, the implications of realizing a space-time cloak are truly exciting. P. Kinsler and M. W. McCall [26,27] have recently noted some of the more exotic possibilities, including causality editors which alter the order of a sequence of events (causality is not in fact

violated, just made to appear as such to an observer), and "tardis" cloaks which give viewers the temporary impression a region of space is larger that it actually is; these draw their moniker from Doctor Who, a fitting science fiction connection for such a curious concept as cloaking! While such capabilities remain theoretical only—and experimental realization seems distant at best, impossible at worse—we impress the importance of still supporting research directed in such pathways, for it would be reckless to obstruct the potential scientific advances which await.

Yet temporal cloaking's true niche may indeed lie in optical communication systems, not only in the more clandestine avenues implied by the name "cloak," but also in expanding the toolkit for routing and multiplexing signals effectively. For example, the proposal of [47] describes methods for applying time cloaking in a data center switch to route information streams without increasing packet duration. And the proof-of-principle experiments detailed in Chapter 3 provide further examples of how cloaking can enable successful communication as well as thwart it. So although we cannot guarantee that time cloaking will transform optical communication, we are excited with its potential.

7.3 Biphoton Pulse Shaping

The examples of biphoton pulse shaping considered in this dissertation indicate the rapid development of biphoton manipulation in general, and accordingly there exist several important avenues of research to bring such fundamental experiments to more applied specializations, such as secure QKD. In some ways SFG, which proves so valuable in the central demonstrations of biphoton pulse shaping in Chapter 6, now sits as a hindrance to further development. For by requiring signal-idler recombination, any experiments utilizing biphoton SFG are intrinsically ill-suited for QKD implementations, in which the two communicating parties must obviously be spatially separated for any useful application. Moreover, the use of SFG in the previous

Much of the discussion of Section 7.3 can be found in [165].

demonstrations of *ultrafast* biphoton dispersion cancellation (ours and that of [103]) means that a fully nonlocal implementation—in which both photons are measured on separated detectors—has not been realized with such high timing resolution. It is therefore desirable to find alternative high-time-resolution detection methods which could observe these effects nonlocally. Pending further improvements in single-photon detector jitter to the picosecond level [129], methods based on single-photon mixing with ultrashort [166] or chirped [167] classical pulses seem particularly promising, and so nonlocal generalizations of ultrafast dispersion cancellation and orthogonal coding may be possible with such techniques, although they have yet to be demonstrated. Furthermore, high-dimensional time-frequency QKD protocols based on dispersion [69] or temporal modulation [68] have recently been proposed, and it would be interesting to investigate how sophisticated biphoton control could be exploited to realize these schemes in practice.

In fact, it is their potential as information carriers that has motivated much of the previous work on biphoton pulse shaping, and so here we briefly discuss some of the basic ideas behind time-frequency entanglement for QKD. Such correlations prove particularly promising for key distribution in fiber networks, as they are well-preserved through long propagation distances and can generate multiple bits of information per biphoton. A rough schematic of how this process could work is provided in Fig. 7.1. Signal and idler photons produced through SPDC are sent to Alice and Bob, respectively, who measure randomly either the arrival time or frequency of their received photon. Due to the strong spectro-temporal entanglement, measurements in the same basis produce highly correlated results, so by dividing frequency and time into discrete bins, it is possible to construct a secret key through measurements on successive biphotons. And since results in two different bases are uncorrelated—as time and frequency are Fourier conjugates—the presence of an eavesdropper is revealed by publicly comparing some subset of the measured bits and looking for an increased error rate.

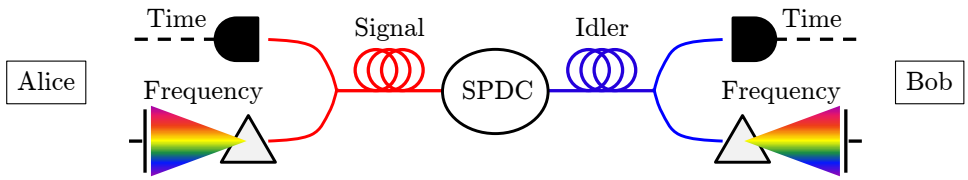

Fig. 7.1. Schematic of time-frequency QKD with entangled photons. Alice and Bob measure either the arrival time or frequency of their respective photons, using results with the same bases to construct a secure key.

The expanded information potential resulting from high-dimensional entanglement can be quantified through the Schmidt decomposition [126, 127], in which the biphoton spectrum is expressed as a sum of factorable two-photon states. Roughly speaking, the number of modes with non-negligible coefficients can be estimated by the Schmidt number K [127]. The larger K is, the greater the amount of information obtainable from the biphoton. As a reference, we note that the idealized biphoton state of Eq. (4.14) with a perfectly monochromatic pump has $K = \infty$; in reality, the finite linewidth of our pump drops our realistic estimate of K to several million or so. Yet actually extracting this information potential can prove extremely difficult. For example, in our experiments [118], the maximum number of frequency chips is limited by the 10-GHz spectral resolution of the pulse shaper—not the ∼200-kHz pump linewidth. Similar behavior has been shown for time binning [67] and orbital angular momentum [130], in which there were observed maximum dimensions beyond which the secure information capacity dropped. The ability to optimize both the intrinsic and practical information potential of biphoton states will prove essential in the experimental development of high-dimensional QKD.

Interestingly, electro-optic modulators have already been proposed for implementing a time-frequency QKD system [68]. Conceptually, the protocol matches Fig. 7.1; however, instead of directly measuring the time variable with a single-photon detector, the authors propose to use a second spectrometer preceded by a time-to-frequency

converter. In this fashion, the arrival time of each photon is converted to a particular frequency, so that a wavelength measurement is equivalent to a temporal measurement. The time-to-frequency converter itself consists of a dispersive element and an electro-optic phase modulator. An advantage of this approach is the improved timing resolution over simple avalanche photodiodes; a disadvantage is the increased dark count rate due to utilization of a detector array in the spectrometer. As might be expected, the Fourier dual to this approach has the reverse advantage/disadvantage relationship; as proposed in [69] and demonstrated with modest success in [70], the spectrometers in the setup of Fig. 7.1 can be replaced by two frequency-to-time converters (highly dispersive elements) with opposite signs of dispersion, followed by single-photon detectors. Thus if both photons are measured in the dispersed-time basis, the dispersion cancellation effect described in Section 6.4 ensures that their arrival times are still synchronized. Intuitively, the connection with a frequency measurement can be understood by the fact that dispersion cancellation is itself a consequence of narrowband spectral entanglement. Although Fourier-transform pulse shaping was not explicitly considered in this proposal—and admittedly, pulse shapers cannot apply dispersions as large as other optical devices such as fiber Bragg gratings—the basic idea does lend itself to such pulse shaping. In fact, it would be interesting to consider how the spectral coding in Section 6.5 could be used for similar time spreading and despreading in a form of code-based time-frequency QKD.

And so while experiments up to this point have already revealed new insights into the behavior of entangled photons, numerous opportunities remain unrealized, particularly in the context of quantum cryptography. Thus we expect the next decade to witness even more advances in biphoton pulse shaping; we have only begun to scratch the surface of the potential within such entangled quanta, and technologies developed in classical optics will no doubt continue to find unanticipated uses in the quantum regime.

LIST OF REFERENCES

LIST OF REFERENCES

[1] A. M. Weiner, *Ultrafast Optics* (Wiley, 2009).

[2] A. M. Weiner, "Femtosecond pulse shaping using spatial light modulators," *Rev. Sci. Instr.* **71**, 1929–1960 (2000).

[3] A. M. Weiner, "Ultrafast optical pulse shaping: A tutorial review," *Opt. Commun.* **284**, 3669–3692 (2011).

[4] A. M. Weiner, J. P. Heritage, and E. M. Kirschner, "High-resolution femtosecond pulse shaping," *J. Opt. Soc. Am. B* **5**, 1563–1572 (1988).

[5] M. F. Roelens, S. Frisken, J. A. Bolger, D. Abakoumov, G. Baxter, S. Poole, and B. J. Eggleton, "Dispersion trimming in a reconfigurable wavelength selective switch," *J. Lightwave Technol.* **26**, 73–78 (2008).

[6] T. Udem, R. Holzwarth, and T. W. Hänsch, "Optical frequency metrology," *Nature* **416**, 233–237 (2002).

[7] N. R. Newbury, "Searching for applications with a fine-tooth comb," *Nature Photon.* **5**, 186–188 (2011).

[8] S. T. Cundiff and A. M. Weiner, "Optical arbitrary waveform generation," *Nature Photon.* **4**, 760–766 (2010).

[9] Z. Jiang, C.-B. Huang, D. E. Leaird, and A. M. Weiner, "Optical arbitrary waveform processing of more than 100 spectral comb lines," *Nature Photon.* **1**, 463–467 (2007).

[10] V. R. Supradeepa, C. M. Long, R. Wu, F. Ferdous, E. Hamidi, D. E. Leaird, and A. M. Weiner, "Comb-based radiofrequency photonic filters with rapid tunability and high selectivity," *Nature Photon.* **6**, 186–194 (2012).

[11] J. M. Lukens, D. E. Leaird, and A. M. Weiner, "A temporal cloak at telecommunication data rate," *Nature* **498**, 205–208 (2013).

[12] V. G. Veselago, "The electrodynamics of substances with simultaneously negative values of ϵ and μ," *Sov. Phys. Usp.* **10**, 509–514 (1968).

[13] J. B. Pendry, A. J. Holden, D. J. Robbins, and W. J. Stewart, "Magnetism from conductors and enhanced nonlinear phenomena," *IEEE Trans. Microw. Theory Tech.* **47**, 2075–2084 (1999).

[14] D. R. Smith, W. J. Padilla, D. C. Vier, S. C. Nemat-Nasser, and S. Schultz, "Composite medium with simultaneously negative permeability and permittivity," *Phys. Rev. Lett.* **84**, 4184–4187 (2000).

[15] A. Alù and N. Engheta, "Achieving transparency with plasmonic and metamaterial coatings," *Phys. Rev. E* **72**, 016623 (2005).

[16] U. Leonhardt, "Optical conformal mapping," *Science* **312**, 1777–1780 (2006).

[17] J. B. Pendry, D. Schurig, and D. R. Smith, "Controlling electromagnetic fields," *Science* **312**, 1780–1782 (2006).

[18] D. Schurig, J. J. Mock, B. J. Justice, S. A. Cummer, J. B. Pendry, A. F. Starr, and D. R. Smith, "Metamaterial electromagnetic cloak at microwave frequencies," *Science* **314**, 977–980 (2006).

[19] J. Li and J. B. Pendry, "Hiding under the carpet: A new strategy for cloaking," *Phys. Rev. Lett.* **101**, 203901 (2008).

[20] V. M. Shalaev, "Transforming light," *Science* **322**, 384–386 (2008).

[21] R. Liu, C. Ji, J. J. Mock, J. Y. Chin, T. J. Cui, and D. R. Smith, "Broadband ground-plane cloak," *Science* **323**, 366–369 (2009).

[22] J. Valentine, J. Li, T. Zentgraf, G. Bartal, and X. Zhang, "An optical cloak made of dielectrics," *Nature Mater.* **8**, 568–571 (2009).

[23] I. I. Smolyaninov, V. N. Smolyaninova, A. V. Kildishev, and V. M. Shalaev, "Anisotropic metamaterials emulated by tapered waveguides: Application to optical cloaking," *Phys. Rev. Lett.* **102**, 213901 (2009).

[24] H. Chen, C. T. Chan, and P. Sheng, "Transformation optics and metamaterials," *Nature Mater.* **9**, 387–396 (2010).

[25] M. W. McCall, A. Favaro, P. Kinsler, and A. Boardman, "A spacetime cloak, or a history editor," *J. Opt.* **13**, 024003 (2011).

[26] P. Kinsler and M. W. McCall, "Cloaks, editors, and bubbles: Applications of spacetime transformation theory," *Ann. Phys.* **526**, 51–62 (2014).

[27] P. Kinsler and M. W. McCall, "Transformation devices: Event carpets in space and space-time," *Phys. Rev. A* **89**, 063818 (2014).

[28] M. Fridman, A. Farsi, Y. Okawachi, and A. L. Gaeta, "Demonstration of temporal cloaking," *Nature* **481**, 62–65 (2012).

[29] B. H. Kolner and M. Nazarathy, "Temporal imaging with a time lens," *Opt. Lett.* **14**, 630–632 (1989).

[30] B. H. Kolner, "Space-time duality and the theory of temporal imaging," *IEEE J. Quantum Electron.* **30**, 1951–1963 (1994).

[31] H. A. Haus, *Waves and Fields in Optoelectronics* (Prentice-Hall, 1984).

[32] C. V. Bennett and B. H. Kolner, "Principles of parametric temporal imaging. I. System configurations," *IEEE J. Quantum Electron.* **36**, 430–437 (2000).

[33] C. V. Bennett and B. H. Kolner, "Principles of parametric temporal imaging. II. System performance," *IEEE J. Quantum Electron.* **36**, 649–655 (2000).

[34] V. Torres-Company, J. Lancis, and P. Andrés, "Space-time analogies in optics," in *Progress in Optics* **56** (E. Wolf, ed.), Ch. 1 (Elsevier, 2011).

[35] C. V. Bennett and B. H. Kolner, "Aberrations in temporal imaging," *IEEE J. Quantum Electron.* **37**, 20–32 (2001).

[36] H. Talbot, "Facts relating to optical science," *Philos. Mag. Ser. 3* **9**, 401–407 (1836).

[37] K. Patorski, "The self-imaging phenomenon and its applications," in *Progress in Optics* **27** (E. Wolf, ed.), Ch. 1 (Elsevier, 1989).

[38] J. Wen, Y. Zhang, and M. Xiao, "The Talbot effect: Recent advances in classical optics, nonlinear optics, and quantum optics," *Adv. Opt. Photon.* **5**, 83–130 (2013).

[39] T. Jannson and J. Jannson, "Temporal self-imaging effect in single-mode fibers," *J. Opt. Soc. Am.* **71**, 1373–1376 (1981).

[40] T. Komukai, T. Yamamoto, and S. Kawanishi, "Optical pulse generator using phase modulator and linearly chirped fiber Bragg gratings," *IEEE Photon. Technol. Lett.* **17**, 1746–1748 (2005).

[41] V. Torres-Company, J. Lancis, and P. Andrés, "Unified approach to describe optical pulse generation by propagation of periodically phase-modulated CW laser light," *Opt. Express* **14**, 3171–3180 (2006).

[42] V. Torres-Company, J. Lancis, and P. Andrés, "Lossless equalization of frequency combs," *Opt. Lett.* **33**, 1822–1824 (2008).

[43] M. Farhat, P.-Y. Chen, S. Guenneau, S. Enoch, R. McPhedran, C. Rockstuhl, and F. Lederer, "Understanding the functionality of an array of invisibility cloaks," *Phys. Rev. B* **84**, 235105 (2011).

[44] V. N. Smolyaninova, I. I. Smolyaninov, and H. K. Ermer, "Experimental demonstration of a broadband array of invisibility cloaks in the visible frequency range," *New J. Phys.* **14**, 053029 (2012).

[45] J. C. Howell, J. B. Howell, and J. S. Choi, "Amplitude-only, passive, broadband, optical spatial cloaking of very large objects," *Appl. Opt.* **53**, 1958–1963 (2014).

[46] J. M. Lukens, A. J. Metcalf, D. E. Leaird, and A. M. Weiner, "Temporal cloaking for data suppression and retrieval," *Optica* **1**, 372–375 (2014).

[47] S. Arnon and M. Fridman, "Data center switch based on temporal cloaking," *J. Lightwave Technol.* **30**, 3427–3433 (2012).

[48] E. Lau, "Beugungserscheinungen an Doppelrastern," *Ann. Phys.* **6**, 417–423 (1948).

[49] J. Jahns and A. Lohmann, "The Lau effect (a diffraction experiment with incoherent illumination)," *Opt. Commun.* **28**, 263–267 (1979).

[50] D. Zalvidea, R. Duchowicz, and E. E. Sicre, "Temporal transformation of periodic incoherent ultrashort light pulses by chirped fiber gratings," *Appl. Opt.* **43**, 3005–3009 (2004).

[51] J. Lancis, C. M. Gómez-Sarabia, J. Ojeda-Castañeda, C. R. Fernández-Pousa, and P. Andrés, "Temporal Lau effect: Noncoherent regeneration of periodic pulse trains," *J. Eur. Opt. Soc. Rapid Publ.* **1**, 06018 (2006).

[52] V. Torres-Company, C. R. Fernández-Pousa, and L. R. Chen, "Temporal Lau effect: A multiwavelength self-imaging phenomenon," *Opt. Lett.* **34**, 1885–1887 (2009).

[53] Agilent Technologies, *Agilent N4901 Serial BERT User's Guide* (2006).

[54] A. J. Metcalf, V. Torres-Company, D. E. Leaird, and A. M. Weiner, "High-power broadly tunable electrooptic frequency comb generator," *IEEE J. Sel. Top. Quantum Electron.* **19**, 3500306 (2013).

[55] L. Mandel and E. Wolf, *Optical Coherence and Quantum Optics* (Cambridge University Press, 1995).

[56] A. Einstein, B. Podolsky, and N. Rosen, "Can quantum-mechanical description of physical reality be considered complete?" *Phys. Rev.* **47**, 777–780 (1935).

[57] J. S. Bell, "On the Einstein Poldolsky Rosen Paradox," *Physics (Long Island City, NY)* **1**, 195–200 (1964).

[58] A. Aspect, "Bell's inequality test: More ideal than ever," *Nature* **398**, 189–190 (1999).

[59] C. H. Bennett and G. Brassard, "Quantum cryptography: Public key distribution and coin tossing," *Proc. IEEE Int. Conf. on Computers, Systems and Signal Processing*, 175–179 (1984).

[60] N. Gisin, G. Ribordy, W. Tittel, and H. Zbinden, "Quantum cryptography," *Rev. Mod. Phys.* **74**, 145–195 (2002).

[61] N. Gisin and R. Thew, "Quantum communication," *Nature Photon.* **1**, 165–171 (2007).

[62] A. K. Ekert, "Quantum cryptography based on Bell's theorem," *Phys. Rev. Lett.* **67**, 661–663 (1991).

[63] T. Jennewein, C. Simon, G. Weihs, H. Weinfurter, and A. Zeilinger, "Quantum cryptography with entangled photons," *Phys. Rev. Lett.* **84**, 4729–4732 (2000).

[64] J. Brendel, N. Gisin, W. Tittel, and H. Zbinden, "Pulsed energy-time entangled twin-photon source for quantum communication," *Phys. Rev. Lett.* **82**, 2594–2597 (1999).

[65] I. Marcikic, H. de Riedmatten, W. Tittel, V. Scarani, H. Zbinden, and N. Gisin, "Time-bin entangled qubits for quantum communication created by femtosecond pulses," *Phys. Rev. A* **66**, 062308 (2002).

[66] H. de Riedmatten, I. Marcikic, V. Scarani, W. Tittel, H. Zbinden, and N. Gisin, "Tailoring photonic entanglement in high-dimensional Hilbert spaces," *Phys. Rev. A* **69**, 050304 (2004).

[67] I. Ali-Khan, C. J. Broadbent, and J. C. Howell, "Large-alphabet quantum key distribution using energy-time entangled bipartite states," *Phys. Rev. Lett.* **98**, 060503 (2007).

[68] J. Nunn, L. J. Wright, C. Söller, L. Zhang, I. A. Walmsley, and B. J. Smith, "Large-alphabet time-frequency entangled quantum key distribution by means of time-to-frequency conversion," *Opt. Express* **21**, 15959–15973 (2013).

[69] J. Mower, Z. Zhang, P. Desjardins, C. Lee, J. H. Shapiro, and D. Englund, "High-dimensional quantum key distribution using dispersive optics," *Phys. Rev. A* **87**, 062322 (2013).

[70] C. Lee, Z. Zhang, G. R. Steinbrecher, H. Zhou, J. Mower, T. Zhong, L. Wang, X. Hu, R. D. Horansky, V. B. Verma, A. E. Lita, R. P. Mirin, F. Marsili, M. D. Shaw, S. W. Nam, G. W. Wornell, F. N. C. Wong, J. H. Shapiro, and D. Englund, "Entanglement-based quantum communication secured by nonlocal dispersion cancellation," *Phys. Rev. A* **90**, 062331 (2014).

[71] V. Binjrajka, C.-C. Chang, A. W. R. Emanuel, D. E. Leaird, and A. M. Weiner, "Pulse shaping of incoherent light by use of a liquid-crystal modulator array," *Opt. Lett.* **21**, 1756–1758 (1996).

[72] A. Pe'er, B. Dayan, A. A. Friesem, and Y. Silberberg, "Temporal shaping of entangled photons," *Phys. Rev. Lett.* **94**, 073601 (2005).

[73] B. Dayan, Y. Bromberg, I. Afek, and Y. Silberberg, "Spectral polarization and spectral phase control of time-energy entangled photons," *Phys. Rev. A* **75**, 043804 (2007).

[74] F. Zäh, M. Halder, and T. Feurer, "Amplitude and phase modulation of time-energy entangled two-photon states," *Opt. Express* **16**, 16452–16458 (2008).

[75] E. Poem, Y. Gilead, Y. Lahini, and Y. Silberberg, "Fourier processing of quantum light," *Phys. Rev. A* **86**, 023836 (2012).

[76] K. J. Blow, R. Loudon, S. J. D. Phoenix, and T. J. Shepherd, "Continuum fields in quantum optics," *Phys. Rev. A* **42**, 4102–4114 (1990).

[77] C. K. Hong and L. Mandel, "Theory of parametric frequency down conversion of light," *Phys. Rev. A* **31**, 2409–2418 (1985).

[78] D. S. Hum and M. M. Fejer, "Quasi-phasematching," *C. R. Phys.* **8**, 180–198, (2007).

[79] D. A. Kleinman, "Theory of optical parametric noise," *Phys. Rev.*, **174**, 1027–1041 (1968).

[80] M. Fiorentino, S. M. Spillane, R. G. Beausoleil, T. D. Roberts, P. Battle, and M. W. Munro, "Spontaneous parametric down-conversion in periodically poled KTP waveguides and bulk crystals," *Opt. Express* **15**, 7479–7488 (2007).

[81] R. J. Glauber, "The quantum theory of optical coherence," *Phys. Rev.* **130**, 2529–2539 (1963).

[82] Y. Shih, "Entangled biphoton source - property and preparation," *Rep. Prog. Phys.* **66**, 1009–1044 (2003).

[83] K. R. Parameswaran, R. K. Route, J. R. Kurz, R. V. Roussev, M. M. Fejer, and M. Fujimura, "Highly efficient second-harmonic generation in buried waveguides formed by annealed and reverse proton exchange in periodically poled lithium niobate," *Opt. Lett.* **27**, 179–181 (2002).

[84] C. Langrock, S. Kumar, J. E. McGeehan, A. E. Willner, and M. M. Fejer, "All-optical signal processing using $\chi^{(2)}$ nonlinearities in guided-wave devices," *J. Lightwave Technol.* **24**, 2579–2592 (2006).

[85] S. Tanzilli, H. De Riedmatten, W. Tittel, H. Zbinden, P. Baldi, M. De Micheli, D. B. Ostrowsky, and N. Gisin, "Highly efficient photon-pair source using periodically poled lithium niobate waveguide," *Electron. Lett.* **37**, 26–28 (2001).

[86] S. Tanzilli, W. Tittel, H. De Riedmatten, H. Zbinden, P. Baldi, M. DeMicheli, D. Ostrowsky, and N. Gisin, "PPLN waveguide for quantum communication," *Eur. Phys. J. D* **18**, 155–160 (2002).

[87] J. M. Lukens, A. Dezfooliyan, C. Langrock, M. M. Fejer, D. E. Leaird, and A. M. Weiner, "Biphoton manipulation with a fiber-based pulse shaper," *Opt. Lett.* **38**, 4652–4655 (2013).

[88] J. Oh, C. Antonelli, and M. Brodsky, "Coincidence rates for photon pairs in WDM environment," *J. Lightwave Technol.* **29**, 324–329 (2011).

[89] Y.-H. Kim and W. P. Grice, "Measurement of the spectral properties of the two-photon state generated via type II spontaneous parametric downconversion," *Opt. Lett.* **30**, 908–910 (2005).

[90] G. Brida, V. Caricato, M. V. Fedorov, M. Genovese, M. Gramegna, and S. P. Kulik, "Characterization of spectral entanglement of spontaneous parametric-down conversion biphotons in femtosecond pulsed regime," *EPL* **87**, 64003 (2009).

[91] E. D. Nelson and M. L. Fredman, "Hadamard spectroscopy," *J. Opt. Soc. Am.* **60**, 1664–1669 (1970).

[92] K. G. Beauchamp, *Applications of Walsh and Related Functions* (Academic Press, 1984).

[93] C. Liang, K. F. Lee, M. Medic, P. Kumar, R. H. Hadfield, and S. W. Nam, "Characterization of fiber-generated entangled photon pairs with superconducting single-photon detectors," *Opt. Express* **15**, 1322–1327 (2007).

[94] J. D. Franson, "Bell inequality for position and time," *Phys. Rev. Lett.* **62**, 2205–2208 (1989).

[95] L. Mandel, "Quantum effects in one-photon and two-photon interference," *Rev. Mod. Phys.* **71**, S274–S282 (1999).

[96] Z. Y. Ou, X. Y. Zou, L. J. Wang, and L. Mandel, "Observation of nonlocal interference in separated photon channels," *Phys. Rev. Lett.* **65**, 321–324 (1990).

[97] Q. Zhang, C. Langrock, H. Takesue, X. Xie, M. Fejer, and Y. Yamamoto, "Generation of 10-GHz clock sequential time-bin entanglement," *Opt. Express* **16**, 3293–3298 (2008).

[98] Q. Zhang, H. Takesue, S. W. Nam, C. Langrock, X. Xie, B. Baek, M. M. Fejer, and Y. Yamamoto, "Distribution of time-energy entanglement over 100 km fiber using superconducting single-photon detectors," *Opt. Express* **16**, 5776–5781 (2008).

[99] J. M. Lukens, A. Dezfooliyan, C. Langrock, M. M. Fejer, D. E. Leaird, and A. M. Weiner, "Demonstration of high-order dispersion cancellation with an ultrahigh-efficiency sum-frequency correlator," *Phys. Rev. Lett.* **111**, 193603 (2013).

[100] B. Dayan, A. Pe'er, A. A. Friesem, and Y. Silberberg, "Nonlinear interactions with an ultrahigh flux of broadband entangled photons," *Phys. Rev. Lett.* **94**, 043602 (2005).

[101] B. Dayan, "Theory of two-photon interactions with broadband down-converted light and entangled photons," *Phys. Rev. A* **76**, 043813 (2007).

[102] K. A. O'Donnell and A. B. U'Ren, "Time-resolved up-conversion of entangled photon pairs," *Phys. Rev. Lett.* **103**, 123602 (2009).

[103] K. A. O'Donnell, "Observations of dispersion cancellation of entangled photon pairs," *Phys. Rev. Lett.* **106**, 063601 (2011).

[104] A. Valencia, M. V. Chekhova, A. Trifonov, and Y. Shih, "Entangled two-photon wave packet in a dispersive medium," *Phys. Rev. Lett.* **88**, 183601 (2002).

[105] S.-Y. Baek, O. Kwon, and Y.-H. Kim, "Temporal shaping of a heralded single-photon wave packet," *Phys. Rev. A* **77**, 013829 (2008).

[106] J. D. Franson, "Nonlocal cancellation of dispersion," *Phys. Rev. A* **45**, 3126–3132 (1992).

[107] Z. Zheng and A. M. Weiner, "Spectral phase correlation of coded femtosecond pulses by second-harmonic generation in thick nonlinear crystals," *Opt. Lett.* **25**, 984–986 (2000).

[108] C. K. Hong, Z. Y. Ou, and L. Mandel, "Measurement of subpicosecond time intervals between two photons by interference," *Phys. Rev. Lett.* **59**, 2044–2046 (1987).

[109] A. M. Steinberg, P. G. Kwiat, and R. Y. Chiao, "Dispersion cancellation and high-resolution time measurements in a fourth-order optical interferometer," *Phys. Rev. A* **45**, 6659–6665 (1992).

[110] A. M. Steinberg, P. G. Kwiat, and R. Y. Chiao, "Dispersion cancellation in a measurement of the single-photon propagation velocity in glass," *Phys. Rev. Lett.* **68**, 2421–2424 (1992).

[111] A. F. Abouraddy, M. B. Nasr, B. E. A. Saleh, A. V. Sergienko, and M. C. Teich, "Quantum-optical coherence tomography with dispersion cancellation," *Phys. Rev. A* **65**, 053817 (2002).

[112] M. B. Nasr, S. Carrasco, B. E. A. Saleh, A. V. Sergienko, M. C. Teich, J. P. Torres, L. Torner, D. S. Hum, and M. M. Fejer, "Ultrabroadband biphotons generated via chirped quasi-phase-matched optical parametric down-conversion," *Phys. Rev. Lett.* **100**, 183601 (2008).

[113] V. Torres-Company, H. Lajunen, and A. T. Friberg, "'Nonlocal' dispersion cancelation with classical light," *New J. Phys.* **11**, 063041 (2009).

[114] V. Torres-Company, A. Valencia, M. Hendrych, and J. P. Torres, "Cancellation of dispersion and temporal modulation with nonentangled frequency-correlated photons," *Phys. Rev. A* **83**, 023824 (2011).

[115] V. Torres-Company, J. P. Torres, and A. T. Friberg, "Shaping the ultrafast temporal correlations of thermal-like photons," *Phys. Rev. Lett.* **109**, 243905 (2012).

[116] S. E. Harris, "Chirp and compress: Toward single-cycle biphotons," *Phys. Rev. Lett.* **98**, 063602 (2007).

[117] S. Sensarn, G. Y. Yin, and S. E. Harris, "Generation and compression of chirped biphotons," *Phys. Rev. Lett.* **104**, 253602 (2010).

[118] J. M. Lukens, A. Dezfooliyan, C. Langrock, M. M. Fejer, D. E. Leaird, and A. M. Weiner, "Orthogonal spectral coding of entangled photons," *Phys. Rev. Lett.* **112**, 133602 (2014).

[119] A. M. Weiner, Z. Jiang, and D. E. Leaird, "Spectrally phase-coded O-CDMA [invited]," *J. Opt. Netw.* **6**, 728–755 (2007).

[120] J. P. Heritage and A. M. Weiner, "Advances in spectral optical code-division multiple-access communications," *IEEE J. Sel. Top. Quantum Electron.* **13**, 1351–1369 (2007).

[121] R. Kaltenbaek, J. Lavoie, D. N. Biggerstaff, and K. J. Resch, "Quantum-inspired interferometry with chirped laser pulses," *Nature Phys.* **4**, 864–868 (2008).

[122] R. Kaltenbaek, J. Lavoie, and K. J. Resch, "Classical analogues of two-photon quantum interference," *Phys. Rev. Lett.* **102**, 243601 (2009).

[123] R. Prevedel, K. M. Schreiter, J. Lavoie, and K. J. Resch, "Classical analog for dispersion cancellation of entangled photons with local detection," *Phys. Rev. A* **84**, 051803 (2011).

[124] Z. Zheng, A. M. Weiner, K. R. Parameswaran, M.-H. Chou, and M. M. Fejer, "Low-power spectral phase correlator using periodically poled $LiNbO_3$ waveguides," *IEEE Photon. Technol. Lett.* **13**, 376–378 (2001).

[125] C. Belthangady, C.-S. Chuu, I. A. Yu, G. Y. Yin, J. M. Kahn, and S. E. Harris, "Hiding single photons with spread spectrum technology," *Phys. Rev. Lett.* **104**, 223601 (2010).

[126] C. K. Law, I. A. Walmsley, and J. H. Eberly, "Continuous frequency entanglement: Effective finite Hilbert space and entropy control," *Phys. Rev. Lett.* **84**, 5304–5307 (2000).

[127] C. K. Law and J. H. Eberly, "Analysis and interpretation of high transverse entanglement in optical parametric down conversion," *Phys. Rev. Lett.* **92**, 127903 (2004).

[128] M. V. Fedorov, M. A. Efremov, A. E. Kazakov, K. W. Chan, C. K. Law, and J. H. Eberly, "Packet narrowing and quantum entanglement in photoionization and photodissociation," *Phys. Rev. A* **69**, 052117 (2004).

[129] R. H. Hadfield, "Single-photon detectors for optical quantum information applications," *Nature Photon.* **3**, 696–705 (2009).

[130] J. Leach, E. Bolduc, D. J. Gauthier, and R. W. Boyd, "Secure information capacity of photons entangled in many dimensions," *Phys. Rev. A* **85**, 060304 (2012).

[131] M. Razavi, "Multiple-access quantum key distribution networks," *IEEE Trans. Commun.* **60**, 3071–3079 (2012).

[132] J. M. Lukens, O. Odele, C. Langrock, M. M. Fejer, D. E. Leaird, and A. M. Weiner, "Generation of biphoton correlation trains through spectral filtering," *Opt. Express* **22**, 9585–9596 (2014).

[133] J. Perina, Jr., "Characterization of a resonator using entangled two-photon states," *Opt. Commun.* **221**, 153–161 (2003).

[134] Y. J. Lu, R. L. Campbell, and Z. Y. Ou, "Mode-locked two-photon states," *Phys. Rev. Lett.* **91**, 163602 (2003).

[135] H. Goto, Y. Yanagihara, H. Wang, T. Horikiri, and T. Kobayashi, "Observation of an oscillatory correlation function of multimode two-photon pairs," *Phys. Rev. A* **68**, 015803 (2003).

[136] H. Goto, H. Wang, T. Horikiri, Y. Yanagihara, and T. Kobayashi, "Two-photon interference of multimode two-photon pairs with an unbalanced interferometer," *Phys. Rev. A* **69**, 035801 (2004).

[137] H. Wang, T. Horikiri, and T. Kobayashi, "Polarization-entangled mode-locked photons from cavity-enhanced spontaneous parametric down-conversion," *Phys. Rev. A* **70**, 043804 (2004).

[138] H.-b. Wang and T. Kobayashi, "Quantum interference of a mode-locked two-photon state," *Phys. Rev. A* **70**, 053816 (2004).

[139] M. A. Sagioro, C. Olindo, C. H. Monken, and S. Pádua, "Time control of two-photon interference," *Phys. Rev. A* **69**, 053817 (2004).

[140] A. Zavatta, S. Viciani, and M. Bellini, "Recurrent fourth-order interference dips and peaks with a comblike two-photon entangled state," *Phys. Rev. A* **70**, 023806 (2004).

[141] F.-Y. Wang, B.-S. Shi, and G.-C. Guo, "Observation of time correlation function of multimode two-photon pairs on a rubidium D_2 line," *Opt. Lett.* **33**, 2191–2193 (2008).

[142] W. C. Jiang, X. Lu, J. Zhang, O. Painter, and Q. Lin, "A silicon-chip source of bright photon-pair comb," arXiv:1210.4455 (2012).

[143] S. Clemmen, K. P. Huy, W. Bogaerts, R. G. Baets, P. Emplit, and S. Massar, "Continuous wave photon pair generation in silicon-on-insulator waveguides and ring resonators," *Opt. Express* **17**, 16558–16570 (2009).

[144] S. Azzini, D. Grassani, M. J. Strain, M. Sorel, L. G. Helt, J. E. Sipe, M. Liscidini, M. Galli, and D. Bajoni, "Ultra-low power generation of twin photons in a compact silicon ring resonator," *Opt. Express* **20**, 23100–23107 (2012).

[145] Y. J. Lu and Z. Y. Ou, "Optical parametric oscillator far below threshold: Experiment versus theory," *Phys. Rev. A* **62**, 033804 (2000).

[146] V. Torres-Company, J. Lancis, H. Lajunen, and A. T. Friberg, "Coherence revivals in two-photon frequency combs," *Phys. Rev. A* **84**, 033830 (2011).

[147] A. M. Weiner and D. E. Leaird, "Generation of terahertz-rate trains of femtosecond pulses by phase-only filtering," *Opt. Lett.* **15**, 51–53 (1990).

[148] K.-H. Luo, J. Wen, X.-H. Chen, Q. Liu, M. Xiao, and L.-A. Wu, "Second-order Talbot effect with entangled photon pairs," *Phys. Rev. A* **80**, 043820 (2009).

[149] X.-B. Song, H.-B. Wang, J. Xiong, K. Wang, X. Zhang, K.-H. Luo, and L.-A. Wu, "Experimental observation of quantum Talbot effects," *Phys. Rev. Lett.* **107**, 033902 (2011).

[150] J. Azaña and M. A. Muriel, "Technique for multiplying the repetition rates of periodic trains of pulses by means of a temporal self-imaging effect in chirped fiber gratings," *Opt. Lett.* **24**, 1672–1674 (1999).

[151] J. Azaña and M. Muriel, "Temporal self-imaging effects: theory and application for multiplying pulse repetition rates," *IEEE J. Sel. Top. Quantum Electron.* **7**, 728–744 (2001).

[152] J. Caraquitena, Z. Jiang, D. E. Leaird, and A. M. Weiner, "Tunable pulse repetition-rate multiplication using phase-only line-by-line pulse shaping," *Opt. Lett.* **32**, 716–718 (2007).

[153] T. Sizer, II, "Increase in laser repetition rate by spectral selection," *IEEE J. Quantum Electron.* **25**, 97–103 (1989).

[154] P. Petropoulos, M. Ibsen, M. N. Zervas, and D. J. Richardson, "Generation of a 40-GHz pulse stream by pulse multiplication with a sampled fiber Bragg grating," *Opt. Lett.* **25**, 521–523 (2000).

[155] K. Yiannopoulos, K. Vyrsokinos, E. Kehayas, N. Pleros, K. Vlachos, H. Avramopoulos, and G. Guekos, "Rate multiplication by double-passing Fabry-Perot filtering," *IEEE Photon. Technol. Lett.* **15**, 1294–1296 (2003).

[156] A. M. Weiner, D. E. Leaird, G. P. Wiederrecht, and K. A. Nelson, "Femtosecond pulse sequences used for optical manipulation of molecular motion," *Science* **247**, 1317–1319 (1990).

[157] M. R. Schroeder, *Number Theory in Science and Communication* (Springer-Verlag, 1986).

[158] O. D. Odele, J. M. Lukens, J. A. Jaramillo-Villegas, C. Langrock, M. M. Fejer, D. E. Leaird, and A. M. Weiner, "Tunable delay control of biphoton correlations based on dispersion cancellation," *(submitted)* (2015).

[159] J. van Howe and C. Xu, "Ultrafast optical signal processing based upon space-time dualities," *J. Lightwave Technol.* **24**, 2649 (2006).

[160] J. van Howe and C. Xu, "Ultrafast optical delay line by use of a time-prism pair," *Opt. Lett.* **30**, 99–101 (2005).

[161] J. E. Sharping, Y. Okawachi, J. van Howe, C. Xu, Y. Wang, A. E. Willner, and A. L. Gaeta, "All-optical, wavelength and bandwidth preserving, pulse delay based on parametric wavelength conversion and dispersion," *Opt. Express* **13**, 7872–7877 (2005).

[162] M. Asobe, O. Tadanaga, H. Miyazawa, Y. Nishida, and H. Suzuki, "Multiple quasi-phase-matched $LiNbO_3$ wavelength converter with a continuously phase-modulated domain structure," *Opt. Lett.* **28**, 558–560 (2003).

[163] J. van Howe and C. Xu, "Ultrafast optical delay line using soliton propagation between a time-prism pair," *Opt. Express* **13**, 1138–1143 (2005).

[164] P. Y. Bony, M. Guasoni, P. Morin, D. Sugny, A. Picozzi, H. R. Jauslin, S. Pitois, and J. Fatome, "Temporal spying and concealing process in fibre-optic data transmission systems through polarization bypass," *Nature Commun.* **5**, 4678 (2014).

[165] J. M. Lukens and A. M. Weiner, "Biphoton pulse shaping," in *All-Optical Signal Processing* (S. Wabnitz and B. J. Eggleton, eds.), Ch. 13 (Springer, 2015).

[166] O. Kuzucu, F. N. C. Wong, S. Kurimura, and S. Tovstonog, "Joint temporal density measurements for two-photon state characterization," *Phys. Rev. Lett.* **101**, 153602 (2008).

[167] J. M. Donohue, M. Agnew, J. Lavoie, and K. J. Resch, "Coherent ultrafast measurement of time-bin encoded photons," *Phys. Rev. Lett.* **111**, 153602 (2013).

[168] J. Guigay, "On Fresnel diffraction by one-dimensional periodic objects, with application to structure determination of phase objects," *Opt. Acta* **18**, 677–682 (1971).

APPENDICES

A. DERIVATION OF EQUATION (2.17)

In this section, we fill in the steps between Eqs. (2.16) and (2.17) for the propagation of a phase-modulated field through quarter-Talbot dispersion. The mathematical procedure is modeled after [168], which we have adapted to temporal pulse propagation. Taking $a_{\rm out}(t)$ as the field after propagation through a distance L, Eq. (2.10) can be expressed in the integral form [1]

$$a_{\rm out}(t) = \frac{e^{i\pi/4}}{\sqrt{2\pi\beta_2 L}} \int_{-\infty}^{\infty} dt'\, a_{\rm in}(t') e^{-i(t-t')^2/2\beta_2 L}, \tag{A.1}$$

where $a_{\rm in}(t)$ is the input time-domain field; although in our case it is given by Eq. (2.16), for now we deem it a generic periodic waveform. We do specialize to L an integer fraction N of the Talbot distance L_T. That is,

$$L = \frac{L_T}{N} = \frac{4\pi}{\beta_2 \omega_m^2 N}, \tag{A.2}$$

assuming for definiteness that $\beta_2 > 0$. It proves convenient to express the continuous variable of integration t' in the somewhat strange form

$$t' = t + \eta + \frac{4\pi p}{\omega_m}, \tag{A.3}$$

where p is an integer ranging from $-\infty$ to ∞. To encompass the full time axis, for each value of p the variable η must be integrated from η_0 to $\eta_0 + 4\pi/\omega_m$, where the particular value for η_0 is chosen for convenience later. For this decomposition of t' and choice for L, the integral kernel of Eq. (A.1) can be expanded as follows:

$$\begin{aligned} \exp\left[-\frac{i(t-t')^2}{2\beta_2 L}\right] &= \exp\left[-i\frac{(\eta + 4\pi p/\omega_m)^2}{2\beta_2}\frac{\beta_2\omega_m^2 N}{4\pi}\right] \\ &= \exp\left[-i\left(\frac{\omega_m^2 N\eta^2}{8\pi} + \omega_m N p\eta + 2\pi N p^2\right)\right] \\ &= e^{-i\omega_m^2 N\eta^2/8\pi} e^{-i\omega_m N p\eta}. \end{aligned} \tag{A.4}$$

Since $a_{\text{in}}(t)$ repeats itself with period $2\pi/\omega_m$, we know that $a_{\text{in}}(t+\eta+4\pi p/\omega_m) = a_{\text{in}}(t+\eta)$, and the full integral becomes

$$a_{\text{out}}(t) = e^{i\pi/4}\sqrt{\frac{\omega_m^2 N}{8\pi^2}}\int_{\eta_0}^{\eta_0+4\pi/\omega_m} d\eta\, a_{\text{in}}(t+\eta)e^{-i\omega_m^2 N\eta^2/8\pi}\sum_{p=-\infty}^{\infty} e^{-i\omega_m N p\eta}. \tag{A.5}$$

The usefulness of the peculiar integral substitution finally becomes clear when we observe that the infinite sum corresponds to a Dirac comb. Specifically,

$$\sum_{p=-\infty}^{\infty} e^{-i\omega_m N p\eta} = \frac{2\pi}{\omega_m N}\sum_{p=-\infty}^{\infty}\delta\left(\eta - \frac{2\pi p}{\omega_m N}\right), \tag{A.6}$$

which permits integration of Eq. (A.5) irrespective of the particular form of the periodic input. To complete the integration, we now choose a value for η_0 such that $0 < \eta_0 < \frac{2\pi}{\omega_m N}$, which limits the only nonzero contributions to values of p ranging from 1 to $2N$. We therefore obtain

$$a_{\text{out}}(t) = \frac{e^{i\pi/4}}{\sqrt{2N}}\sum_{p=1}^{2N} a_{\text{in}}\left(t + \frac{2\pi p}{\omega_m N}\right)e^{-i\pi p^2/2N}. \tag{A.7}$$

An additional simplification results by breaking up the sum into its first and last N terms, i.e.,

$$a_{\text{out}}(t) = \frac{e^{i\pi/4}}{\sqrt{2N}}\sum_{p=1}^{N}\left\{a_{\text{in}}\left(t + \frac{2\pi p}{\omega_m N}\right)e^{-i\pi p^2/2N} + a_{\text{in}}\left(t + \frac{2\pi(N+p)}{\omega_m N}\right)e^{-i\pi(p+N)^2/2N}\right\}. \tag{A.8}$$

Expanding the second exponential gives $(-1)^p(-i)^N e^{-i\pi p^2/2N}$, and invoking the periodicity of $a_{\text{in}}(t)$, we finally arrive at

$$a_{\text{out}}(t) = \frac{e^{i\pi/4}}{\sqrt{2N}}\sum_{p=1}^{N} a_{\text{in}}\left(t + \frac{2\pi p}{\omega_m N}\right)e^{-i\pi p^2/2N}\Big[1 + (-1)^p(-i)^N\Big]. \tag{A.9}$$

At this point, we specialize to the quarter-Talbot case ($N = 4$). Since the $p = 1, 3$ terms vanish for $N = 4$, only two terms remain, giving

$$a_{\text{out}}(t) = \frac{1}{\sqrt{2}}\left\{e^{-i\pi/4}a_{\text{in}}\left(t + \frac{\pi}{\omega_m}\right) + e^{i\pi/4}a_{\text{in}}(t)\right\}. \tag{A.10}$$

Plugging in the phase-modulated input field of Eq. (2.16) produces

$$a_{\text{out}}(t) = \frac{1}{\sqrt{2}}\left\{e^{i\frac{\pi}{4}(\cos\omega_m t - 1)} + e^{-i\frac{\pi}{4}(\cos\omega_m t - 1)}\right\}, \tag{A.11}$$

and by invoking the trigonometric identities $\cos x - 1 = -2\sin^2(x/2)$ and $e^{iz} + e^{-iz} = 2\cos z$, the output field is simplified to

$$a_{\text{out}}(t) = \sqrt{2}\cos\left(\frac{\pi}{2}\sin^2\frac{\omega_m t}{2}\right), \tag{A.12}$$

which represents Eq. (2.17) of the main text.

B. THEORY OF BIPHOTON SFG IN PPLN WAVEGUIDES

In this appendix, we derive the output quantum state produced in the process of biphoton SFG. Our formulation, based on the interaction picture and similar in form to that in [102], represents an alternative to the Heisenberg-picture approaches in [101, 116] and is in our opinion more transparent to the important physics. The primary purpose of this development, then, is twofold: first, to show that under the actual conditions in our experiments, biphoton SFG does indeed represent a valid measurement of the fourth-order correlation function $\Gamma^{(2,2)}(\tau)$; and second, to obtain an explicit expression for the upconversion efficiency and arrive at the conditions under which it is equal to that of SPDC.

The appropriate interaction Hamiltonian is of the form

$$\hat{H}_I(t) = \epsilon_0 \int_{\mathcal{V}} d^3\vec{r}\,\gamma(z)\hat{E}^{(+)}_{\mathrm{SFG}}(z,t)\hat{E}^{(-)}_s(z,t)\hat{E}^{(-)}_i(z,t) + \mathrm{h.c.}, \tag{B.1}$$

which corresponds to Eq. (4.6), but with the pump replaced by a quantized SFG field. For simplicity, we assume that the upconversion waveguide is identical to that used for SPDC, and we take its longitudinal extent from $z = 0$ to $z = L$; all effects of propagation between crystals can be incorporated with spectral filters $\tilde{H}_{s,i}(\omega)$ applied to the signal and idler photons, respectively. The signal, idler, and SFG field operators, after factoring out terms slowly varying with frequency, are thus

$$\hat{E}^{(+)}_s(z,t) = i\left[\frac{\hbar\omega_0}{4\pi\epsilon_0 c n_0 S}\right]^{1/2} \int_0^\infty d\Omega\, \tilde{H}_s(\omega_0+\Omega)\hat{a}_s(\omega_0+\Omega)e^{i(k_s z-\omega_0 t-\Omega t)}, \tag{B.2}$$

$$\hat{E}^{(+)}_i(z,t) = i\left[\frac{\hbar\omega_0}{4\pi\epsilon_0 c n_0 S}\right]^{1/2} \int_0^{\omega_0} d\Omega'\, \tilde{H}_i(\omega_0-\Omega')\hat{a}_i(\omega_0-\Omega')e^{i(k_i z-\omega_0 t+\Omega' t)}, \tag{B.3}$$

and

$$\hat{E}^{(-)}_{\mathrm{SFG}}(z,t) = -i\left[\frac{\hbar\omega_0}{2\pi\epsilon_0 c n_p S}\right]^{1/2} \int_{-2\omega_0}^\infty d\Omega_p\, \hat{a}^\dagger_{\mathrm{SFG}}(2\omega_0+\Omega_p)e^{-i(k_p z-2\omega_0 t-\Omega_p t)}. \tag{B.4}$$

We assume that the input state at some initial time t_i is the biphoton of Eq. (4.14), and invoking the same perturbative approximation as in Eq. (4.11), the generated quantum state at time $t > t_i$ is

$$|\varphi\rangle = M|\Psi\rangle + \frac{1}{i\hbar}\int_{t_i}^{t} dt'\, \hat{H}_I(t')|\Psi\rangle, \tag{B.5}$$

with $M \sim 1$.

Ultimately, we are interested in the flux of upconverted photons at the waveguide output ($z = L$), which can be represented by the operator [generalizing Eq. (4.17)]

$$\hat{\mathcal{F}}_{\rm SFG} = \frac{n_p \epsilon_0 c S}{\hbar\omega_0} \hat{E}^{(-)}_{\rm SFG}(L,t)\hat{E}^{(+)}_{\rm SFG}(L,t), \tag{B.6}$$

so that the expected value of the flux is

$$\begin{aligned} \mathcal{F}_{\rm SFG} &= \langle\varphi|\hat{\mathcal{F}}_{\rm SFG}|\varphi\rangle \\ &= \frac{n_p \epsilon_0 c S}{\hbar\omega_0}\langle\varphi|\hat{E}^{(-)}_{\rm SFG}(L,t)\hat{E}^{(+)}_{\rm SFG}(L,t)|\varphi\rangle. \end{aligned} \tag{B.7}$$

Making use of Eqs. (4.14), (B.1), (B.5), and (B.7), the only nonzero contribution is

$$\hat{E}^{(+)}_{\rm SFG}(L,t)|\varphi\rangle = \frac{1}{i\hbar}\hat{E}^{(+)}_{\rm SFG}(L,t)\int_{t_i}^{t} dt'\, \hat{H}_I(t')\int_0^{\omega_0} d\Omega\, \phi(\Omega)|\omega_0+\Omega\rangle_s|\omega_0-\Omega\rangle_i. \tag{B.8}$$

Plugging in the expressions in Eqs. (B.1)-(B.4), and utilizing operator relations Eqs. (4.2)-(4.5), this simplifies to

$$\begin{aligned} \hat{E}^{(+)}_{\rm SFG}(L,t)|\varphi\rangle &= \frac{i\hbar\omega_0^2\gamma_m}{8\pi^2\epsilon_0 c^2 n_0 n_p S} e^{-2i\omega_0 t}\int_0^{\omega_0} d\Omega\, \phi(\Omega)\tilde{H}_s(\omega_0+\Omega)\tilde{H}_i(\omega_0-\Omega) \\ &\quad\times\int_{-2\omega_0}^{\infty} d\Omega_p\, e^{ik_p L}\int_{-2\omega_0}^{\infty} d\Omega_p'\int_0^L dz\, e^{i\Delta k z}\int_{t_i}^{t} dt'\, e^{i\Omega_p' t'} \\ &\quad\times\hat{a}_{\rm SFG}(2\omega_0+\Omega_p)\hat{a}^{\dagger}_{\rm SFG}(2\omega_0+\Omega_p')|{\rm vac}\rangle, \end{aligned} \tag{B.9}$$

where as before $\gamma_m e^{iK_m z}$ corresponds to the dominant poling coefficient in the expansion of $\gamma(z)$ and Δk is the phase mismatch defined in Eq. (4.13). The combination of SFG annihilation and creation operators acting on the vacuum reduces to $\delta(\Omega_p - \Omega_p')|{\rm vac}\rangle$, and taking the limit of long t converts the integral over t' to $2\pi\delta(\Omega_p')$, finally reducing the above expression to

$$\begin{aligned} \hat{E}^{(+)}_{\rm SFG}(L,t)|\varphi\rangle &= |{\rm vac}\rangle\frac{i\hbar\omega_0^2\gamma_m L}{4\pi\epsilon_0 c^2 n_0 n_p S} e^{i(k_p L - 2\omega_0 t)} \\ &\quad\times\int_0^{\omega_0} d\Omega\, \phi(\Omega)\tilde{H}_s(\omega_0+\Omega)\tilde{H}_i(\omega_0-\Omega)e^{i\Delta k L/2}{\rm sinc}\frac{\Delta k L}{2}. \end{aligned} \tag{B.10}$$

The motivation for the tilde notation now becomes clear as we decompose these filters into "manipulation" and "measurement" components; that is, we extract a factor from the product $\tilde{H}_s(\omega_0+\Omega)\tilde{H}_i(\omega_0-\Omega)$ which we deem a part of the measurement process, rather than of the biphoton itself. Specifically, we consider the contributions corresponding to signal-idler delay control and compensation of crystal dispersion as separate from the spectral filtering—i.e., pulse shaping—we wish to measure. Thus we write

$$\tilde{H}_s(\omega_0+\Omega)\tilde{H}_i(\omega_0-\Omega) = H_s(\omega_0+\Omega)H_i(\omega_0-\Omega)e^{-i\Delta kL/2}e^{-i\Omega\tau}, \tag{B.11}$$

where the $H_{s,i}$ represent filtering applied to the biphoton *apart* from the measurement procedure.

Squaring Eq. (B.10) then leads to the interesting result

$$\mathcal{F}_{\mathrm{SFG}} \propto \left| \int_0^{\omega_0} d\Omega\, \phi(\Omega) H_s(\omega_0+\Omega)H_i(\omega_0-\Omega)\mathrm{sinc}\frac{\Delta kL}{2}e^{-i\Omega\tau} \right|^2. \tag{B.12}$$

If we make the assumption $\Delta kL \ll 1$ so that $\mathrm{sinc}\Delta kL/2 \sim 1$, we are left with

$$\begin{aligned} \mathcal{F}_{\mathrm{SFG}} &\propto \left| \int_0^{\omega_0} d\Omega\, \phi(\Omega) H_s(\omega_0+\Omega)H_i(\omega_0-\Omega)e^{-i\Omega\tau} \right|^2 \\ &\propto \Gamma^{(2,2)}(\tau), \end{aligned} \tag{B.13}$$

where we have recalled the expression for the spectrally filtered biphoton wavepacket [Eq. (4.31)]. Therefore we reach the paramount conclusion that, assuming all biphoton frequency components can mix with equal probability, *the rate of sum-frequency generation is directly proportional to the fourth-order biphoton correlation function.* And because of the spectral filtering applied by the pulse shaper in our experiments, which significantly limits the bandwidth of the manipulated photons, we meet the above condition to a great degree of accuracy. Figure B.1 compares the theoretically calculated $\Gamma^{(2,2)}(\tau)$ both considering and neglecting the sinc factor of the SFG guide, where we assume 52-mm-long nonlinear waveguides and filtering by a 5-THz-bandwidth pulse shaper. With each curve normalized to a value of unity, no noticeable differences are evident in the temporal shape of the correlations, which confirms

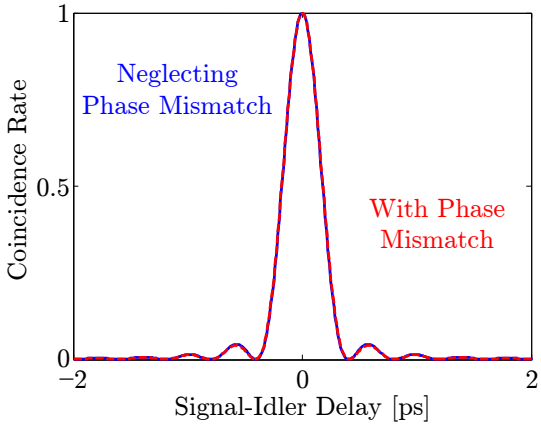

Fig. B.1. Theoretical comparison of SFG flux between neglecting and imposing the $\mathrm{sinc}(\Delta kL/2)$ phase-mismatch factor associated with biphoton SFG. Because of the spectral windowing effected by our pulse shaper, the two curves are nearly identical, indicating that the SFG process introduces no distortion of the biphoton correlations and provides an accurate measure of $\Gamma^{(2,2)}(\tau)$.

that our experiments do indeed operate in a regime in which SFG can be assumed a near-perfect biphoton cross-correlator. (The *absolute* rate of upconversion is reduced by about 5% due to the phase-mismatch factor, but as observed, this has negligible impact on the shape.)

Returning to Eq. (B.10), we can also estimate the absolute efficiency of biphoton SFG in the same manner as for SPDC in Section 4.2. We specialize to the case of maximum efficiency by taking the spectral filters $\tilde{H}_{s,i}$ as lossless and perfectly compensating all spectral phase. Plugging the expression for $\phi(\Omega)$ from Eq. (4.15) into Eq. (B.10) and removing any spectral phase, we are left with

$$\hat{E}^{(+)}_{\mathrm{SFG}}(L,t)|\varphi\rangle = -|\mathrm{vac}\rangle \frac{\hbar\omega_0^3\gamma_m^2 L^2 E_0}{8\pi\epsilon_0 c^3 n_0^2 n_p S} e^{i(k_p L - 2\omega_0 t)} \int_0^{\omega_0} d\Omega\, \mathrm{sinc}^2 \frac{\Delta kL}{2}. \tag{B.14}$$

Noting that the factor preceding the inner product in Eq. (B.7) is nothing more than the input pump photon flux $\mathcal{F}_p$ divided by $|E_0|^2$ [Eq. (4.17)], we find immediately that

$$\frac{\mathcal{F}_{\mathrm{SFG}}}{\mathcal{F}_p} = \frac{\hbar^2\omega_0^6\gamma_m^4 L^4}{64\pi^2\epsilon_0^2 c^6 n_0^4 n_p^2 S^2} \left(\int_0^{\omega_0} d\Omega\, \mathrm{sinc}^2 \frac{\Delta kL}{2} \right)^2. \tag{B.15}$$

Since the SFG efficiency is the ratio of SFG flux at $z = L$ to the signal flux at $L = 0$, we obtain

$$\eta_{\mathrm{SFG}} = \frac{\mathcal{F}_{\mathrm{SFG}}}{\mathcal{F}_s} = \frac{\mathcal{F}_{\mathrm{SFG}}}{\mathcal{F}_p}\eta_{\mathrm{SPDC}}^{-1}, \tag{B.16}$$

where the last equality follows from the relation $\eta_{\mathrm{SPDC}} = \mathcal{F}_{\mathrm{s}}/\mathcal{F}_{\mathrm{p}}$. Recalling Eq. (4.19), and replacing γ_m by $-4d_{\mathrm{eff}}$, we finally obtain

$$\eta_{\mathrm{SFG}} = \frac{2\hbar\omega_0^3 d_{\mathrm{eff}}^2 L^2}{\pi\epsilon_0 c^3 n_0^2 n_p S}\int_0^{\omega_0} d\Omega\,\mathrm{sinc}^2\frac{\Delta kL}{2}, \tag{B.17}$$

which is identical to the expression for η_{SPDC} [Eq. (4.21)]! Therefore, at least ideally (perfect phase compensation), we expect the same quantum efficiency for biphoton upconversion as in generation, a fact which is indeed qualitatively confirmed in our experiments.

VITA

VITA

Joseph M. Lukens graduated with a B.S. in electrical engineering and physics from The University of Alabama in 2011. He is currently pursuing a Ph.D. in electrical engineering at Purdue University, where he conducts research in ultrafast photonics. His interests include high-speed optical communications, temporal cloaking, signal processing of nonclassical light, and biphoton pulse shaping. His work has resulted in six journal publications, one book chapter, and numerous conference presentations, including first-place poster at the inaugural 2014 Siegman International School on Lasers, a feature abstract at the CLEO 2013 press luncheon, and top selection at the 2011 IEEE Region 3 Southeastcon Student Paper Competition. For his contributions to research and mentoring, Lukens was selected as a recipient of the College of Engineering Outstanding Graduate Student Research Award in 2015. Supported by a Meissner Fellowship in his first year at Purdue, since September 2012 he has been funded through a National Defense Science and Engineering Graduate (NDSEG) Fellowship from the DoD. Lukens is a member of the Optical Society (OSA) and an active reviewer for OSA, the American Physical Society (APS), and Nature Publishing Group.